Extended-Frequency Dynamic Phasor Modelling of LCC-HVDC Systems for Electromagnetic Transient Simulations

By

Afshin Bagheri Vandaei

A Thesis Submitted to the Faculty of Graduate Studies
in partial fulfilment of the requirements for the degree of
Doctor of Philosophy

Department of Electrical and Computer Engineering
Faculty of Engineering
The University of Manitoba
Winnipeg, Manitoba, Canada

Abstract

A new model for line-commutated converter (LCC) HVDC systems based upon the concept of extended-frequency dynamic phasors is developed in an electromagnetic transient (EMT)-based simulation platform. The proposed model is capable of representing LCC-HVDC converters during normal as well as abnormal operating modes, such as system imbalances and commutation failure, by automatically adjusting its parameters based upon converter terminal quantity measurements. The model offers a high level of accuracy with reduced computational burden as a suitable replacement for conventional switch-based models of LCC in EMT simulation platforms. The proposed model is then extended to real-time EMT simulations.

The performance of the proposed model is first evaluated against detailed EMT simulations of a simple LCC system. The evaluation is then extended to simulation of large electric networks such as CIGRE HVDC benchmark and IEEE 12-bus systems with an embedded LCC-HVDC link. Simulation results confirm that the proposed dynamic phasor-based model retains EMT-grade accuracy even at large simulations time steps. Significant acceleration ratios reaching up to an order of magnitude are observed in the simulations using the proposed model compared with conventional EMT models.

A real-time EMT variant of the model is then implemented in RTDS real-time simulator. The performance of the dynamic phasor-based model is investigated against existing real-time LCC models with large and small time steps in a hardware-in-loop simulation scenario. The results confirm that the proposed dynamic phasor model retains the same level of accuracy as existing small time-step real-time models while using significantly larger time-steps, thus relieving the burden of real-time computations.

Acknowledgments

I would like to extend my sincere gratitude to Dr. Shaahin Filizadeh for his continuous encouragement, guidance, and valuable suggestions. I consider myself privileged to have had the opportunity to work under his supervision. I would also like to thank my advisory committee members for their comments and feedback throughout the course of this work.

I would like to express my sincere thanks to Dr. Dharshana Muthumuni and also my colleagues at the Manitoba HVDC Research Centre for their support and valuable discussions on various research topics.

I must also thank the academic and technical staff of the Department of Electrical and Computer Engineering at University of Manitoba and RTDS Technologies Inc. I am also grateful to the MITACS Ph.D. Accelerate program, and the Faculty of Graduate Studies at the University of Manitoba for various forms of support they provided.

This acknowledgement will not be complete without thanking my family. I extend my gratitude to my parents, and to my brothers.

Contents

List of Tables

List of Figures

List of Symbols

Z	Impedance
Y	Admittance
ω	Angular Frequency (rad/s)
f	Frequency (Hz)
Z_c	Characteristic impedance
Y_c	Characteristic admittance
Δt	Simulation time step
t	Time
j	Imaginary unit
$i(t)$	Instantaneous current
$v(t)$	Instantaneous voltage
$I(t)$	Current dynamic phasor
$V(t)$	Voltage dynamic phasor
$I_{his}(t)$	History current dynamic phasor
$\Re$	Real part of a complex number

List of Abbreviations and Acronyms

EMT	Electromagnetic Transient
DP	Dynamic Phasor
TS	Transient Stability
DP-EMT	Dynamic Phasor - Electromagnetic Transient
HIL	Hardware-in-loop

List of Copyrighted Material

I. Parts of Sections 4.3 and 4.4 are "Reproduced by permission of the Institute of Engineering & Technology" from IET journal paper (A.B. Vandaei and S. Filizadeh) [80].

II. Parts of Section 5.2 is reproduced from IEEE conference paper (A.B. Vandaei et al) [81].

Chapter 1

Introduction

1.1 Background

In the analysis and design of power systems, electrical engineers employ different types of simulation platforms with various approaches for modeling electrical components. This results in different levels of accuracy and computational intensity while solving the same power system. Maintaining high accuracy and simultaneously minimizing computational intensity of computer simulations has been a major challenge for power system engineers.

Transient Stability (TS)-type programs are among such simulation platforms, and facilitate power system stability and dynamic behavior studies [1]. Traditionally, phasor representation has been used as the basic modeling approach in most TS-type programs to cover low-frequency (normally below 5 Hz) electromechanical dynamics of rotating devices [2]-[3] as well as fundamental-frequency phenomena of devices such as HVDC converters [4]. Therefore, fast electromagnetic transients are neglected and as such large

simulation time steps (in the order of milliseconds) may be used to simulate large electrical networks consisting of thousands of nodes.

To cover those neglected phenomena in detail within a small electric network, Electromagnetic Transient (EMT) simulators have been introduced. These simulators facilitate inclusion of fast transients, which are mostly related to switching in power-electronic devices or events such as lighting strikes, using smaller simulation time steps (in the order of microseconds). Therefore, EMT-type simulations are applicable in much smaller power systems than TS-type ones to keep them computationally viable and at the same time to retain a high level of details within the electric network.

Widespread utilization of power electronic-based systems in recent decades such as modern HVDC systems and flexible AC transmission systems (FACTS) devices, distributed energy resources, etc., has made these sophisticated systems an inevitable part of today's power system studies. Modeling and simulation of power electronic-based systems requires a new modeling approach that can facilitate inclusion of detailed models in a large electric network.

To overcome the above challenges, the concept of time-varying dynamic phasors (DPs) was introduced [5] to provide user-defined complexity level of simulation by neglecting or averaging details of an electric component's behavior. A time-varying dynamic phasor is simply a phasor representation of a time-domain signal using magnitude and phase angle information that may vary with time. Such a modelling approach equips electrical engineers with the necessary means for inclusion of more

detailed models in large electric networks and as a result an unprecedented insight into the operation of a power system.

HVDC transmission systems are one of the areas where DP modeling approach becomes applicable and can help electrical engineers with improved system design and analysis tools. HVDC as a power electronic-based system has become an inevitable part of many modern power systems with applications such as long distance electrical power transmission, connecting grids with different frequencies, providing grid access to onshore and offshore power generation from renewable energy resources, etc. Voltage-source converters (VSCs) and line-commutated converters (LCCs) are the two main topologies used in HVDC systems. The former topology has been the subject of wide-spread interest in recent years due to its insignificant level of harmonic generation, better reactive power control, and site area compactness while the latter has been a conventional approach with lower station losses, lower cost, higher reliability, established maturity, and higher power capability [6]. Therefore, the majority of existing HVDC systems employ LCC-HVDC schemes. New LCC-HVDC systems continue to be built and together with the existing ones they will continue to be a major player in modern power systems. The focus of this research is on this class of HVDC converters.

This research aims to develop a computationally affordable DP model of an LCC-HVDC system in an EMT-type environment and to use such a model in large network studies. Using a DP-based model one can include a user-defined number of harmonics addressing the transients of switching events in an LCC-HVDC system with better

accuracy than conventional phasor models while still being able to simulate systems at large time-steps.

1.2 Research Motivation

DPs have been widely used to model DC-DC converters [7]-[8], resonant converters [9], DC-AC bridge topologies [10], FACTS [11]-[12], HVDC topologies [4], [13]-[14], electrical machines [15]-[18], sub-synchronous resonance (SSR) [19], hybrid simulation as in TS-EMT and DP-EMT interfaces [20], etc.

Recent achievements using DP for modeling line-commutated converters as the building blocks of HVDC systems can be summarized into switching function modifications [4], [21]-[38]. The term switching function simply refers to the mathematical relationship between voltage and current waveforms on the DC and AC sides of an LCC as introduced in [34]. The same mathematical concept is used to study the frequency and harmonic transfer phenomena in an LCC in [25]. Such an approach would result in a complicated model, which might not necessarily be able to work under different operating conditions (e.g., unbalanced operation and commutation failure). The work in [35] addresses unbalanced operating conditions and how they can affect harmonic distortions. [32, 36] use the switching function concept to build a model for an LCC under balanced operating conditions considering only the fundamental frequency component of the system response. [31] is an attempt for covering asymmetrical operating conditions but shows large inaccuracies during system transients. Improved

accuracy is achieved in [29] by inclusion of a limited number of harmonics. [4] is an attempt to derive a general DP-based LCC model; however, it is designed only for a specific type of asymmetry. Yang et al. derived switching functions only for fundamental-frequency operation using a dq reference frame, which makes their DP equivalents complicated as reported in [37]. A DP model is developed solely to represent the LCC performance during commutation failure in [30]. Parametric average-value and generalized averaging methods are used in the most recent literature for modeling switching functions in [38].

Most of existing complicated models have never been implemented in an EMT-type simulator such as PSCAD/EMTDC to be compared with a conventional time-domain model and as a result their computational advantage is under a shadow of doubt. Consequently, computational affordability, as the main advantage of DP-based modeling, would also be overshadowed with such complicated models due to the time it takes to run them even in a small electric network. This aspect is also largely unaddressed in existing literature. Therefore, one might end up with a complicated DP model for LCC-HVDC systems without any real world benefits.

A close examination of existing DP-based LCC-HVDC models reveals a clear need for developing a model that:

(i) covers all the operating conditions of LCC-HVDC systems (balanced, unbalanced, and commutation failure);

(ii) allows inclusion of an arbitrary number of harmonics without having to redevelop the model;

(iii) is embedded into an EMT-type simulation platform; and

(iv) offers quantified computational benefits over conventional EMT models.

The lack of a simple switching function-based model that can work under any operating conditions and its feasibility assessment studies when implemented in an EMT-type simulator are the main motivations for this research.

1.3 Desired Outcomes and Objectives

The majority of previous research on LCC-HVDC DP model development has been focused on modifying voltage and current switching functions in a way such that they can work under any operating conditions without considering the fact that the resulting complexity may imply excessive computational requirements. Therefore, even the base model without inclusion of higher-frequency harmonics, when implemented in an EMT-type software, may take a longer time than existing time-domain models to execute. Extending to higher harmonics for better accuracy would be practically out of question as a result. In this regard, the main endeavor of this research is development of a simplified, general DP model for LCC-HVDC transmission systems followed by a feasibility assessment of the required computational effort. The following items constitute the main objectives and motivations of this research.

a) A comprehensive review of literature on DP-based models of LCC-HVDC systems;

b) Implementing a DP-based model of a 6-pulse Graetz bridge as the main building block of an LCC-HVDC system in PSCAD/EMTDC and RSCAD real-time simulation environments;

c) Extension of the model to arbitrary pulse-number bridges;

d) Validating the model comparing its results with detailed time-domain switching models;

e) Investigating the performance of the DP model in large electrical networks such as CIGRE HVDC benchmark model [39]-[41], IEEE 12 bus system [42], or larger.

The dynamic phasor models are developed in both PSCAD/EMTDC and RSCAD real-time EMT simulation environments and the results are validated against existing time-domain switching models in these EMT-type simulation platforms. Then, they are applied in large systems to show how inclusion of a large number of harmonics can affect the system response accuracy at different time steps.

1.4 Thesis Organization

This thesis consists of six chapters. Chapter 2 discusses the findings of the literature survey on the dynamic phasor concept, mathematical formulations, and modeling approaches in LCC-HVDC simulation. Chapter 3 briefly introduces LCC-HVDC subsystem, its control schemes, and voltage and current waveforms at both AC and DC sides. In Chapter 4, basic operation of an LCC-HVDC transmission system will be discussed and its dynamic phasor model will be developed based upon the concept of

switching functions. The accuracy of the developed model will be investigated against a time-domain switching model in PSCAD/EMTDC. Chapter 5 demonstrates the application of the proposed DP-based model in real-time simulation of moderately large electrical networks with embedded LCC-HVDC systems and a HIL setup for its control. Chapter 6 presents thesis contributions, conclusions, and recommendations for future work.

Chapter 2

Dynamic Phasor Modeling Principles

2.1 Introduction

This chapter begins with the necessity of transient studies in power systems. It will be followed with the role of dynamic phasors (DPs) in power systems transient studies and how electrical engineers can benefit from such a modeling approach. Then, various terms referring to the same concept as a dynamic phasor will be introduced and different applications of this modeling approach will be mentioned conducting a literature review. Among a wide range of applications, LCC-HVDC systems are introduced as an area where the features offered by dynamic phasors can be applied for improved transient studies. To do so, the fundamentals of DP-based modeling are established by the end of this chapter.

2.2 Overview of DP-Based Transient Studies

Power systems are complex and interconnected large electric networks with a wide variety of continuous or discrete, and linear or nonlinear components. For optimal design

and implementation of electrical power systems and subsequently their control, operation, and maintenance, electrical engineers need to be provided with system responses under different operating conditions. Analytical methods would be extremely challenging, if at all possible, to achieve such information and actual field tests are expensive or impossible to conduct. Therefore, various types of computer-based simulation software are used to overcome such challenges and facilitate power system studies in general.

There are many different studies conducted on power systems such as power flow, short circuit, protective device coordination, arc flash hazard analysis, motor starting, harmonic mitigation and compliance, ground grid system, transient disturbances analysis, etc. In this regard, transient analysis addresses transients associated with exchange of energy within electric and magnetic fields or mechanical systems as in electromagnetic or electromechanical transients, respectively.

Electromagnetic transients are related to high-frequency phenomena in the range of 50 Hz to 50 MHz, which are further classified into slow, fast, and very fast front surges by CIGRE standards. It is while the electromechanical transients cover very low frequency contents in the range of 1 Hz to 3 Hz. Therefore, EMT-type simulation platforms are best suited for small but detailed systems with simulation time-steps in the order of microseconds. On the other hand, simulation of electromechanical transients of large electric networks are characterized by large time steps in the order of milliseconds.

With widespread utilization of power electronic based systems (e.g., HVDC networks, FACTS devices, and renewable energy resource interfaces) there is an undeniable need for simulation platforms with the capability of modeling EMTs within large electric networks. Therefore, there is a gap between electromagnetic and

electromechanical-based simulation platforms; this can be addressed using a new modeling approach named dynamic phasors.

Dynamic phasor-type modeling is known under various names such as time-varying complex signal modeling, time-varying phasor modeling, analytical signal modeling, shifted-frequency analysis, multi-frequency averaging, generalized (state-space) averaging, etc., with different applications in fields from communication and vibro-acoustics to power systems. There have been many studies on the application of the so-called dynamic average-value models (DAVMs) in DC power systems of electric vehicles [43], naval electrical systems [44], aircrafts [45], and space crafts [46]. Dynamic phasors have also found applications in power systems wherever an electric device is connected to the grid using power electronic converters such as variable-speed wind energy systems [47], FACTS devices [48], renewable energy resources [49], microgrid automation [50], etc. In terms of power system transients, dynamic phasors are applicable in studies related to subsynchronous resonance (SSR) [19], transient stability [2], and power electronic controls [51]-[54]. [55] can be considered as one of the first research works carried out to establish the mathematical background of time-varying phasors and their application in electromagnetic transients computation.

LCC-HVDC systems are power electronic based systems with short-term, high-frequency transients due to switching of their converters and fast-acting controllers. With the increasing complexity of modern electrical networks, these LCC-HVDC systems are widely embedded within large AC systems consisting of thousands of electrical nodes resulting in very large admittance matrices. Therefore, application of DPs for computationally affordable simulation of such systems is inevitable. To model such systems, one should first establish the mathematical background of dynamic phasors.

Then, one can use the established concepts to model any electric component based on DPs whenever it is necessary.

2.3 Fundamentals of the Dynamic Phasor Concept

Phasor representation of an AC (sinusoidal) signal in power systems is a well-known concept where one can use the constant amplitude and phase of a vector to represent a time varying AC (i.e., sinusoidal) signal. In this regards, the time-varying AC signal $x(t)$ can be written in a general form as in (2-1) for a given base frequency ω.

$$x(t) = A\cos(\omega t + \alpha) \tag{2-1}$$

where A and α are the magnitude and phase of the AC signal, respectively. Using Euler's formula, one can go from the trigonometric function $x(t)$ to a complex exponential function as in (2-2), which is the fundamental of conventional phasor analysis in power systems. Since the imaginary part in the complex exponential function is a redundant term, one can use only the real part of the complex signal with amplitude A and phase α to go back to the time domain signal as follows:

$$x(t) = \Re[Ae^{j\alpha}e^{j\omega t}] \tag{2-2}$$

The term $e^{j\omega t}$ is called the carrier and it does not contain additional information for building the time domain signal using a complex exponential one if the base frequency is known. Therefore, (2-3) can be considered as the phasor representation of (2-1) with respect to the base frequency ω.

$$X(t) = Ae^{j\alpha} \tag{2-3}$$

It must be noted that (2-3) is a constant and not a dynamic phasor yet. Phasor representation is a useful modeling approach since it replaces a time varying signal with a

constant one. The need for dynamic phasors appears during power system transients when the base frequency ω, amplitude A, or phase angle α are not constant values anymore and as such the signal $x(t)$ is not necessarily periodic or sinusoidal any longer as shown in Figure 2-1. Despite lack of periodicity the arbitrary waveform $x(t)$ may be approximated by a number of purely sinusoidal waveforms with different frequencies, amplitudes, and phases over a sampling window $[t\text{-}T_0,t)$. In this way, a non-periodic waveform can be approximated with a number of periodic ones in each sampling interval.

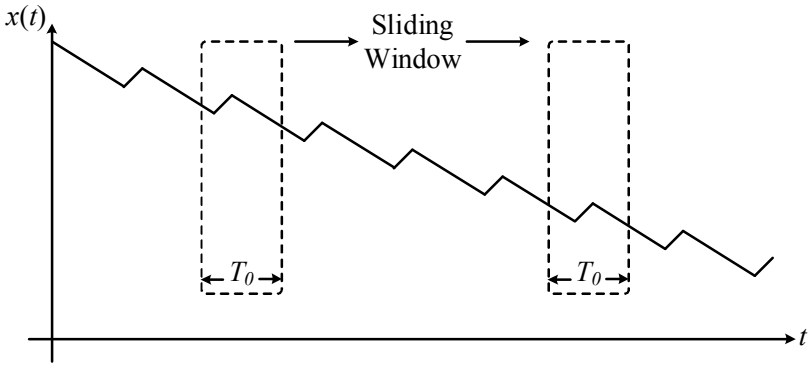

Figure 2-1 DP visualization of a time varying aperiodic signal

Therefore, over a sampling window, the arbitrary waveform $x(t)$ can be built from the following function.

$$x(t-T_0+s)=\sum_{n=-\infty}^{\infty}\langle A\rangle_n(t)e^{jn\omega\,(t-T_0+s)} \tag{2-4}$$

where the base frequency is defined as $\omega=2\pi/T_0$. In the case of modeling switching functions of an LCC-HVDC system, T_0 is normally set to the fundamental frequency of AC system. According to (2-4), an infinite number of sinusoidal waveforms can be added together to form $x(t)$ over each sampling window. This would result in perfect accuracy in arbitrary signal approximation (provided that the original signal does not contain any discontinuities) but would require an infinite number of constituent sinusoids

(harmonics). As a result, there should be a compromise between desired accuracy and the level of complexity as both increase together; normally the infinite series in (2-4) is truncated, which results in some loss of accuracy for the sake of practical implementation. $2\langle A\rangle_n(t)$ is now a dynamic phasor with a time varying phase and amplitude, which can be calculated as follows.

$$2\langle A\rangle_n(t)=\frac{1}{T_0}\int_0^{T_0} x(t-T_0+s)e^{-jn\omega(t-T_0+s)}ds \tag{2-5}$$

These dynamic phasors are the Fourier series coefficients of the portion of the arbitrary signal within the moving window. Finally, one can have the dynamic phasors as follows.

$$2\langle A\rangle_n(t)=\left|\langle A\rangle_n(t)\right|e^{j\alpha_n(t)} \tag{2-6}$$

where $\left|\langle A\rangle_n(t)\right|$ is the amplitude of each dynamic phasor and $\alpha_n(t)$ is its phase. The original time-domain signal may be obtained as follows.

$$x(t)=\Re[\langle A\rangle_0+2\sum_{n=1}^{\infty}\left|\langle A\rangle_n(t)\right|e^{j(n\omega t+\alpha_n(t))}] \tag{2-7}$$

The factor 2 appears due to the fact that negative-indexed phasors have the same amplitude but the opposite phase as the positive-indexed ones. From this point forward, (2-5) is used to extract the dynamic phasor representation of a given time varying arbitrary signal $x(t)$ as in (2-8).

$$\langle x\rangle_n(t)=\frac{1}{T_0}\int_0^{T_0} x(t-T_0+s)e^{-jn\omega(t-T_0+s)}ds \tag{2-8}$$

The following properties become useful in modeling power system components. First one is the dynamic phasor representation of the derivative of a function, which comes in the following form.

$$\left\langle \frac{dx(t)}{dt} \right\rangle_n = \frac{d\left\langle x(t) \right\rangle_n}{dt} + jn\omega \left\langle x(t) \right\rangle_n \tag{2-9}$$

Next is dynamic phasor of the product of two signals $x(t)$ and $y(t)$ as follows.

$$\left\langle x(t).y(t) \right\rangle_n = \sum_{i=-\infty}^{\infty} \left\langle x \right\rangle_{n-i}(t).\left\langle y \right\rangle_i(t) \tag{2-10}$$

which is the convolution between two phasor domain equivalents of the two functions. This property becomes useful when using DPs along with multiplicative switching functions in modeling power electronic converters.

2.4 Chapter Summary

This chapter provided a short review of the definition and necessity of dynamic phasors in power system transient studies. As previously mentioned with the inclusion of fast transients in a large power system, dynamic phasors can be employed to keep modeling accuracy at an acceptable level for large simulation time steps. Then mathematical background of dynamic phasors was also presented.

Chapter 3

LCC-HVDC Systems

3.1 Introduction

Traditionally, HVDC systems were introduced as a supplement to AC transmission systems. With the dawn of a new energy era and smart grid deployment, HVDC systems are expected to go far beyond their traditional applications. Nowadays, HVDC is a method of choice in applications such as subsea electrical transmission, interconnection of asynchronous AC systems, long-distance bulk power transmission, interconnection of remote renewable recourses and AC systems, etc. LCC as a common approach for building HVDC systems is the focus of this research. Since LCC-HVDC case studies often involve large systems, DP would be an appropriate modeling approach for covering the transients due to LCC switching without having to use EMT-level time-steps. Building a general and computationally feasible DP-based model of an LCC requires investigating its performance and its voltage and current waveform on both AC and DC sides.

3.2 Subsystem Definition

A general representation for a line-commutated converter-based high-voltage direct current (LCC-HVDC) system is a DC link connecting two AC systems through a combination of six-pulse bridge converters and transformers as shown in Figure 3-1. There are many different configurations for an HVDC system such as monopolar, bipolar with one 12-pulse valve-group per pole, bipolar with two 12-pulse valve-groups per pole, back to back bipolar, multi-terminal, etc., for different applications [5]. Depending on the scheme being used for an HVDC system, one can come up with the DC link configuration, the number of 6-pulse converters to build the LCC, configuration of AC transformers, and the appropriate circuit for the AC filters.

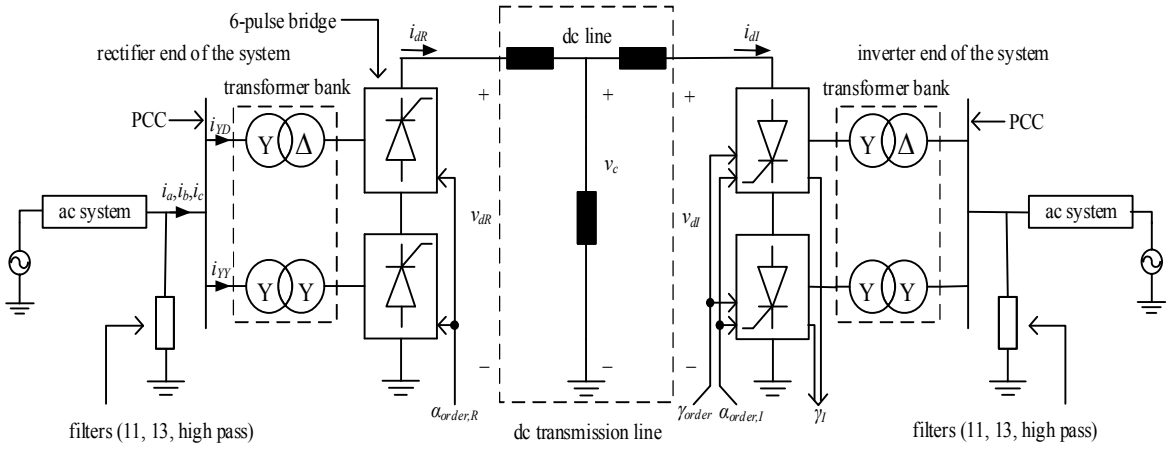

Figure 3-1 LCC-HVDC system configuration

The left hand side bridge is referred to as the rectifier where AC power is transformed (converted) to DC. It is while the right hand side bridge works as an inverter where DC quantities are converted to AC. In this regard, all the left hand side blocks in Figure 3-1

will be referred to as rectifying components and the right hand side ones are called inverting devices.

3.2.1 AC systems

Based on the Thevenin equivalent circuit theorem, the terminating AC systems can be replaced with an AC voltage source in series with a Thevenin equivalent impedance, Z_S, which is usually highly inductive. Short circuit ratio (SCR) and effective short circuit ratio (ESCR) are two important indicators for basic performance analysis of an HVDC circuit based on terminating AC system parameters. Although these two indicators are not much effective in addressing power-voltage instability, overvoltage transients, fault recovery, and harmonic interactions of an HVDC system, they are applicable as simple methods for investigating the expected level of performance of an HVDC system.

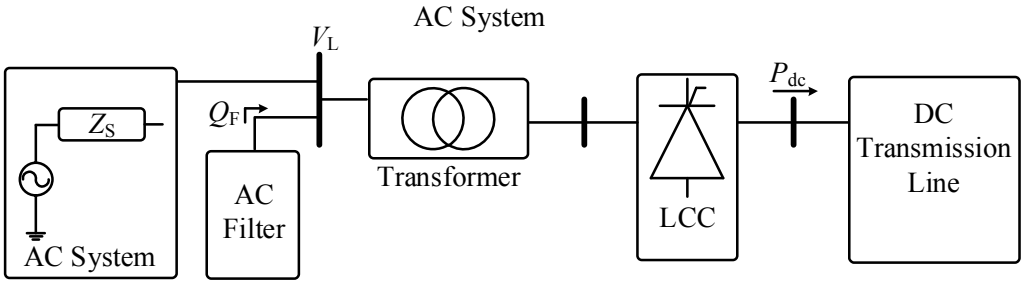

Figure 3-2 Rectifying side AC system

Considering the AC system at the rectifying end of a single-infeed HVDC as in Figure 3-2, one can define the terms SCR and ESCR as follows.

$$SCMVA = \frac{V_L^{\,2}}{Z_S} \tag{3-1}$$

$$SCR = \frac{SCMVA}{P_{dc}} \tag{3-2}$$

$$ESCR = SCR - \frac{Q_F}{P_{dc}} \tag{3-3}$$

where $SCMVA$ is the short circuit complex power of the AC system at converter's AC bus bar, V_L is the line voltage, Q_F is the reactive power of the AC filter at rated voltage, and P_{dc} is the rated dc power. As a rule of thumb, one can categorize an AC system as reasonably strong when its $ESCR$ is larger than 2.5. Such an $ESCR$ would guarantee system robustness during transients and proper support from the AC system for performance of HVDC.

3.2.2 AC filters

Filters are installed at the AC terminals of LCC-HVDC systems to absorb the large spectrum of harmonics that are generated due to the switching operation of LCC valves. Furthermore, they can help the power system by providing reactive power for the LCC converters.

The design procedure for the AC filter is complex and related to multiple factors such as impedance scanning, DC reactive power control, inverter harmonics calculation, filter parameter tuning and setting selection, etc. Since filter design is not the main focus of this research, a simple approach would be considered for its implementation.

A simple design approach for the AC filter block would be using a combination of simple RLC circuits for providing a specific amount of reactive power (Q_F) for a desired ESCR and canceling the lowest dominant harmonics of the converter's injected current.

Considering these two goals and using (3-1)-(3-2) as well as equivalent impedance of a RLC circuit, one can come up with a simple and appropriate circuit for the AC filter block.

While specifically tuned filters provide some of the reactive power of the converter, multiple switchable capacitor banks are also usually installed in parallel with AC filters to adapt delivered reactive power to the demands of the converters. They also provide high-frequency filtering.

3.2.3 Transformers

The converter transformer is an essential part of an HVDC system with various functions at high AC and DC voltages. In a 6-pulse bridge configuration, the AC side of the converter contains current harmonics of order $6n\pm1$. Canceling these harmonics requires expensive filtering equipment. Using two strategically connected converter transformers provides a more economical solution for this problem as in Figure 3-3. This results in a 12-pulse converter configuration, which is a common practice for HVDC systems. Various functions are achieved with such a converter transformer configuration including canceling low order harmonics, galvanic barrier between AC and DC systems, increasing reactive impedance on the AC side for reducing short circuit currents and controlling the rate of rise in valve current during commutation, voltage transformation between AC and DC, supply voltage adjustment using a tap changer, etc.

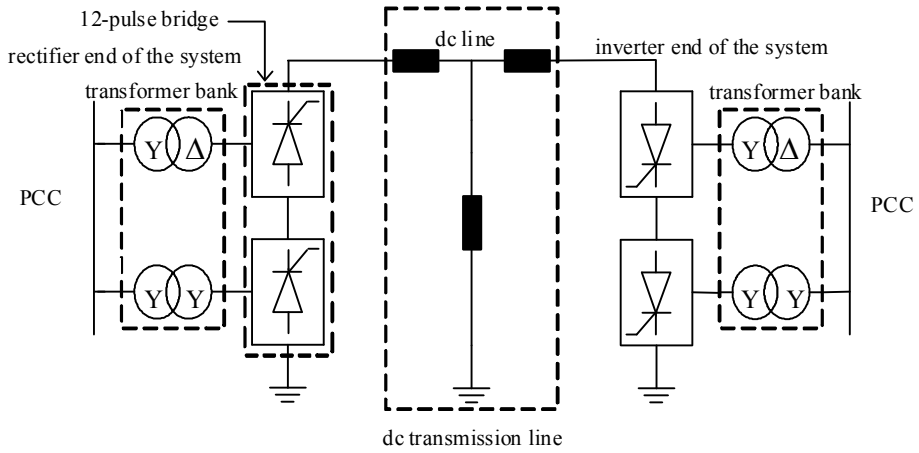

Figure 3-3 Transformer connection in a 12-pulse system

3.2.4 DC line

Different HVDC applications and configurations require different transmission line topologies. As an example, for bulk power transmission over land, overhead transmission lines are a suitable option. Design and selection criteria for HVDC overhead transmission lines require special attention, which is out of the scope of this research. In terms of transient studies and how DP modeling approach can become beneficial to the simulation of the HVDC converter as the main goal of this study, only simple T and π models are used for DC transmission line topologies as in Figure 3-4. Series resistance of the transmission line relies on the physical composition of the conductor at a given temperature. The series inductance and shunt capacitance are produced by the magnetic and electric fields around the conductor and depend on its geometrical arrangement.

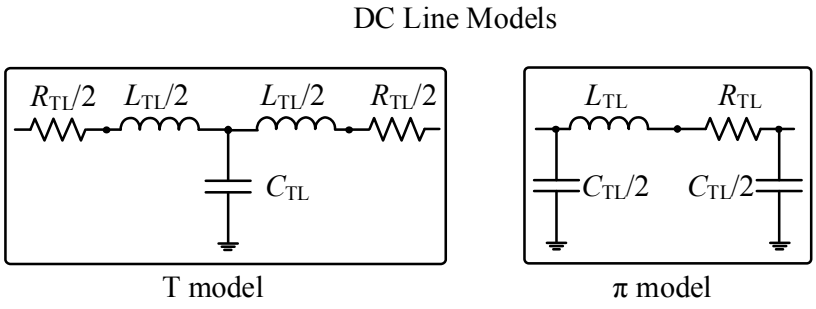

Figure 3-4 DC line models

Beside the RLC line parameters in Figure 3-4, smoothening reactors are also added to the DC line. These reactors are connected in series with the HVDC transmission line or in the intermediate DC circuit of a back-to-back system. Therefore, one can consider two more inductors on each side of the transmission line in Figure 3-4 as part of the model. Decreasing harmonic currents on DC side, reducing the rate of current increment during faults, and improving dynamic stability of HVDC system are among the main usages of such reactors.

3.2.5 Six-pulse bridge converter

A combination of six thyristors as in Figure 3-5 is the building block of a line-commutated converter. Implementing a model for this block using dynamic phasors is the main goal of this study. To achieve this, one should first become familiar with the time domain characteristics of the LCC. Similar to any other electric component, a relationship between its voltage and current waveforms represents its characteristics. Finding such relationships, one can simply transfer them into dynamic phasor domain based on the presented mathematical background as presented in chapter 4.

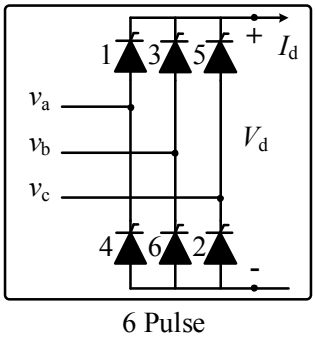

Figure 3-5 Circuit configuration of a 6-pulse Graetz bridge

3.3 LCC-HVDC System Voltage and Current Waveforms Analysis

To investigate the performance of an LCC block, Figure 3-6 is considered with two different connections for transformer on the AC side of the 12-pulse converter. On the DC side, a simple RL load is connected to the bridge.

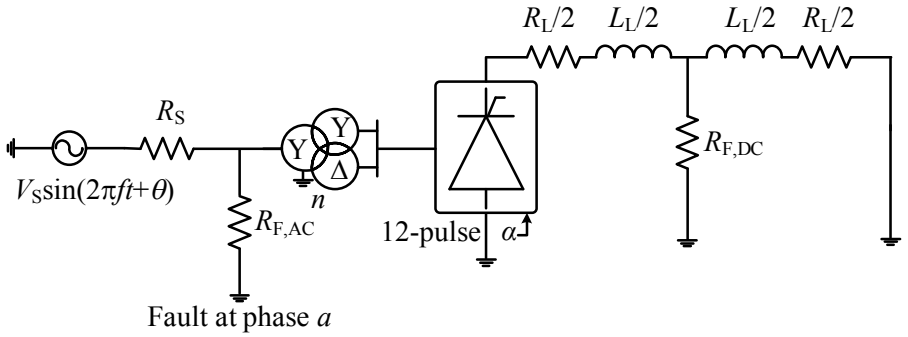

Figure 3-6 Thyristor bridge connected to an ideal AC source

Such case study will provide a numerical overview of the converter operation under different modes of operation. The parameters of the system in Figure 3-6 are presented in Table 3-1.

Table 3-1 System parameters

Parameter	*Symbol*	*Value*
AC voltage	V_s	12 kV
AC voltage frequency	f	50 Hz
AC voltage phase shift	θ	30º
AC system resistance	R_s	0.01 Ω
Transformer MVA	S_T	100 MVA
Transformer turns ratio	n	12/120 kV
Transformer inductance	X_L	0.1 pu
AC side fault resistance	$R_{F,AC}$	0.01 Ω
DC line resistance	R_L	300 Ω
DC line inductance	L_L	5 H
DC side fault resistance	$R_{F,DC}$	0.01 Ω

3.3.1 Normal operation

Firstly the performance of the system under balanced conditions is investigated. During such an operating condition, a purely AC voltage is applied to the Y-connected transformer on the ac side. The transformer will generate two boosted AC voltages on the converter side with 30º phase shift. Then, these two voltages are applied to the two 6-pulse bridges fired at a constant angle thus creating 12-pulse operation. The rectified voltage is then applied to the DC line generating a DC current flow. The relation between AC and DC side voltages and current is investigated next.

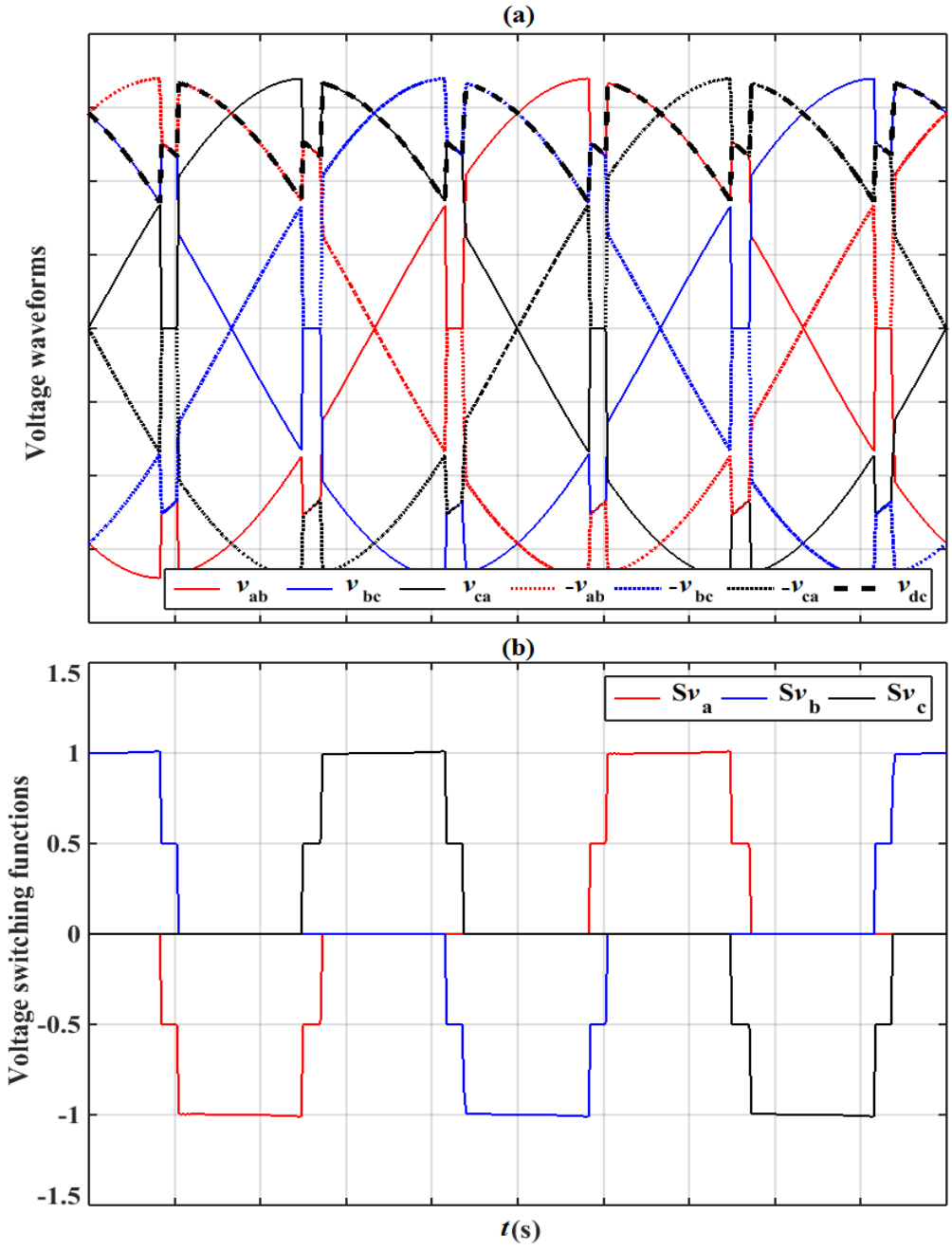

Figure 3-7 Y-connected bridge (a) voltage waveforms (b) voltage switching functions

As Figure 3-7(a) illustrates, over one fundamental-frequency period six pulses exist in the voltage on DC side of the Y-connected bridge. As it can be seen, portions of positive

and negative line-to-line AC voltages may be combined to build the DC voltage. Such an approach results in a set of relations between AC and DC side waveforms referred to as switching functions.

Voltage switching functions can be used as in (3-4) to build the DC side voltage out of AC ones for a 6-pulse bridge.

$$V_{dc} = Sv_a \times v_{ab,S} + Sv_b \times v_{bc,S} + Sv_c \times v_{ca,S} \tag{3-4}$$

Figure 3-7(b) illustrates a set of such switching functions derived from voltage waveforms in Figure 3-7(a). Switching functions normally take 0 or 1 values, except for the short time intervals when there is a transition between conducting valves known as overlap periods. During the overlap time interval when the DC voltage is equal to neither of the two involved AC line voltages, one should use half of the summation of the two AC voltages to build the DC one. Accordingly, the voltage switching functions drop to 0.5 during these time intervals. When a line voltage is no longer contributing to the DC voltage, the switching function becomes equal to zero. Consequently, voltage switching functions constitute of three different levels during each cycle.

On the lower side of the 12-pulse converter where there is a Δ-connected transformer, there will be 30° phase shift in AC voltages and the resulting DC one will be as in Figure 3-8(a). In a similar procedure to what was applied on a Y-connected bridge, voltage switching functions can be extracted out of AC signals as in Figure 3-8(b). The only difference will be the 30° phase shift as expected.

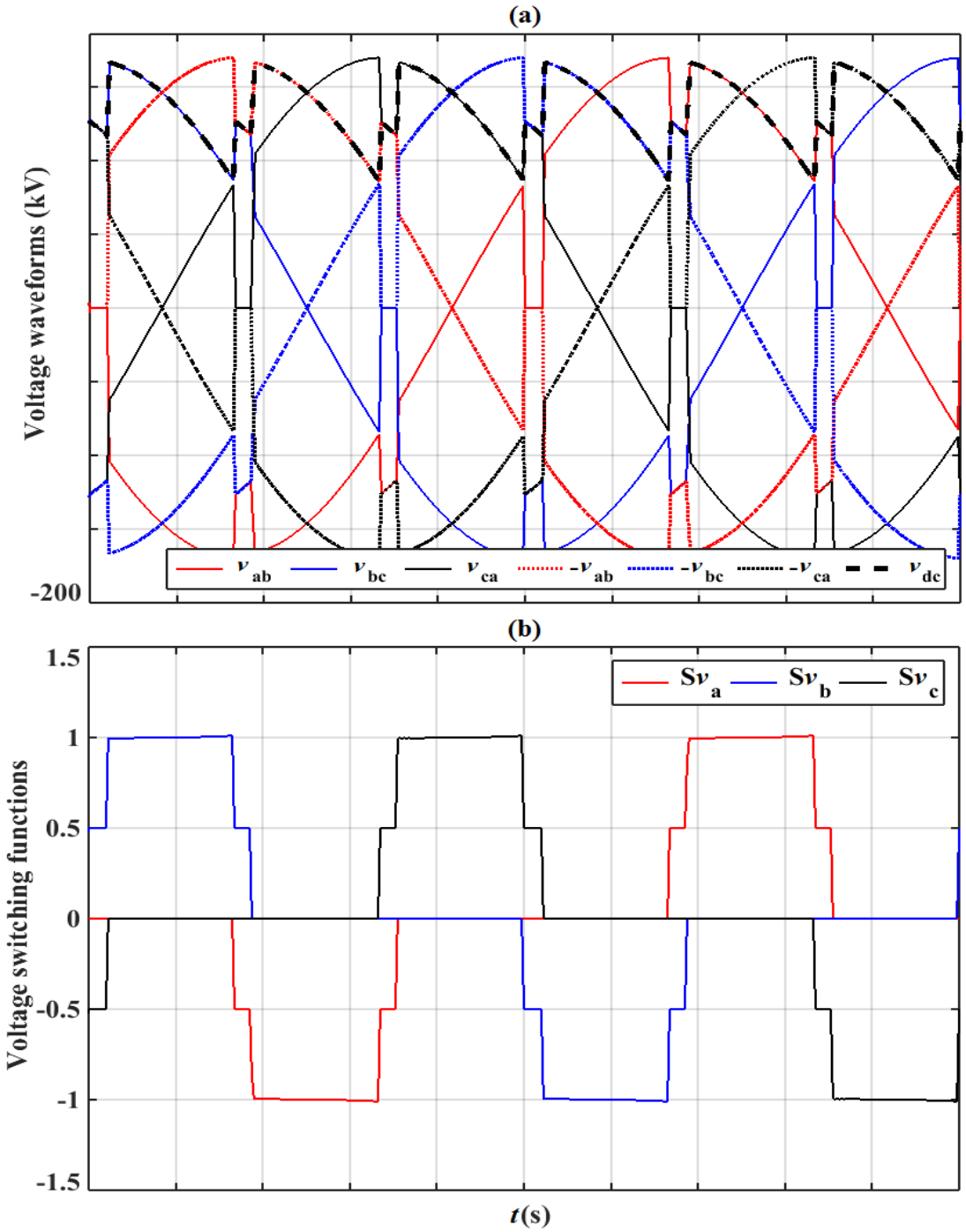

Figure 3-8 Δ-connected bridge (a) voltage waveforms (b) voltage switching functions

Adding the DC side voltage of a Y-connected 6-pulse bridge to that of a Δ-connected one generates a 12-pulse DC voltage as in Figure 3-9. Beside the increment in number of

pulses, the peak-to-peak ripple of the DC voltage also drops markedly thus enhancing its quality.

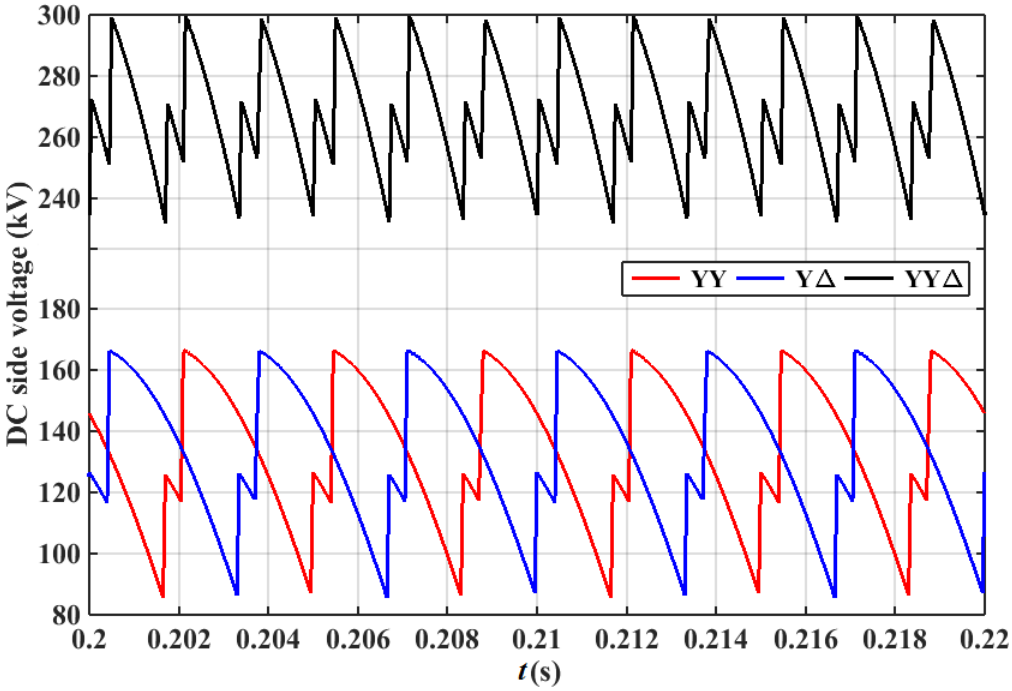

Figure 3-9 Δ-connected bridge (a) voltage waveforms (b) voltage switching functions

Having the DC side voltage, one can apply such a waveform to the DC line and derive the DC current. Then, the current can be used to generate three-phase AC currents as in Figure 3-10(a).

Dividing each AC current by the DC one, one can extract current switching functions as in Figure 3-10(b). There will be only two contact levels for current switching functions; 0 when there is no current and 1 when DC and AC currents are equal. Due to presence of inductive loads, there will be a transition between these two levels rather than a sudden jump. There are different approaches for a transition between these two levels

as in [4]. In this section a linear approximation is applied rather than the original nonlinear ones.

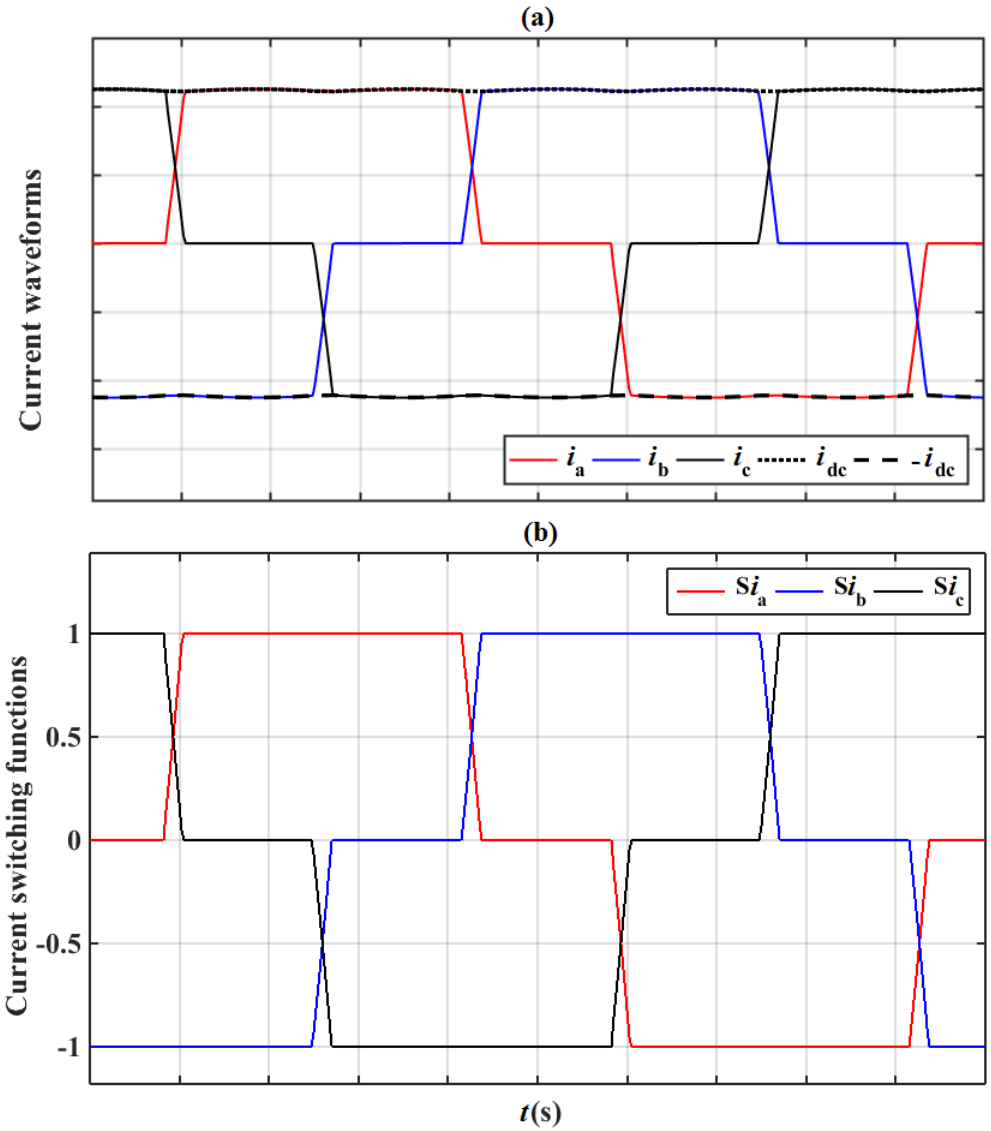

Figure 3-10 Y-connected bridge (a) current waveforms (b) current switching functions

Establishing a set of equations between AC and DC side currents results in current switching functions as in (3-5).

$$i_{a,S} = Si_a \times I_{DC} \qquad i_{b,S} = Si_b \times I_{DC} \qquad i_{c,S} = Si_c \times I_{DC} \tag{3-5}$$

Using Δ connection for the secondary side of the transformer results only in a phase shift in AC currents on the converter side of the transformer as in Figure 3-11.

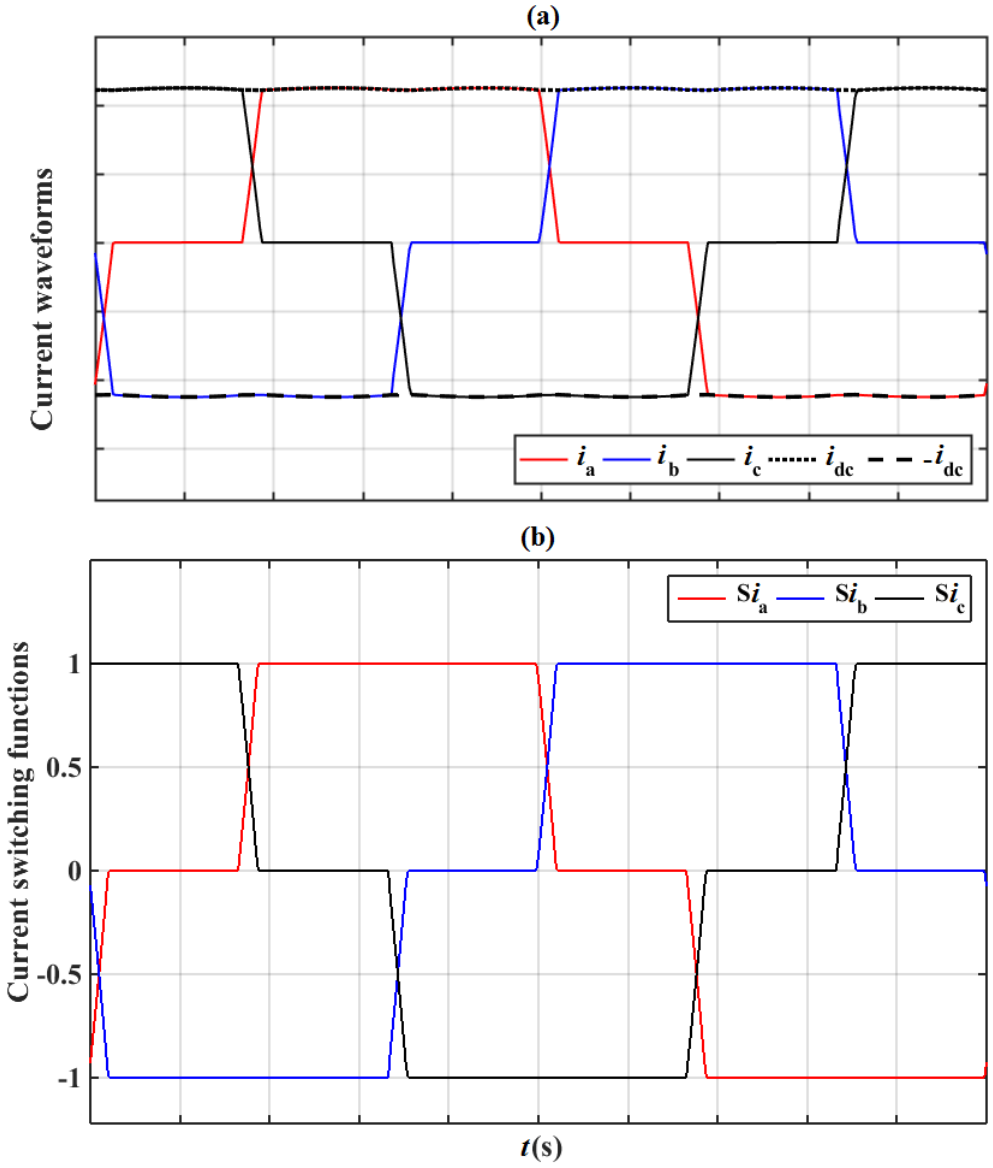

Figure 3-11 Δ-connected bridge (a) current waveforms (b) current switching functions

DC side current waveform of a 12-pulse converter is the result of simultaneous performance of Y- and Δ-connected 6-pulse bridges as in **Error! Reference source not found.**12.

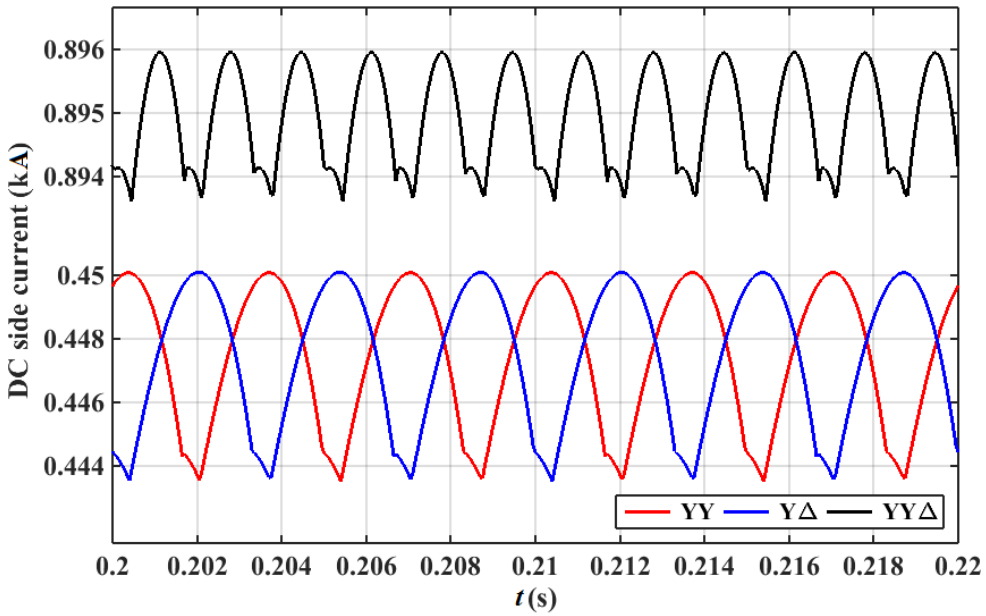

Figure 3-12 DC side current for transformer with Y and Δ connections

Applying fast Fourier transform (FFT) on DC and AC waveforms, one can extract important information about their harmonic contents under normal conditions. Such information will be used in chapter 4 to derive the proposed relaxed model. As Figure 3-13 illustrates, I_{dc} contains harmonics of order $n = 6k$. It can be shown that AC side contains harmonics of order $n = 6k \pm 1$.

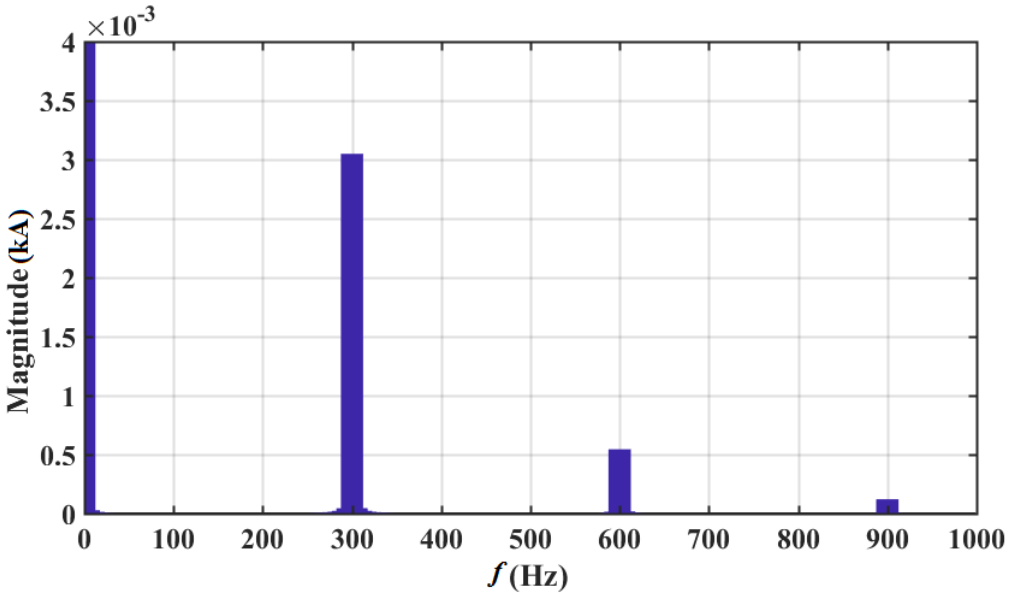

Figure 3-13 Magnitude spectrum of DC side current for Y-connected transformer

The phase information of dominant harmonics in I_{dc} is presented as in Figure 3-14. Such information becomes important for generation of a 12-pulse current.

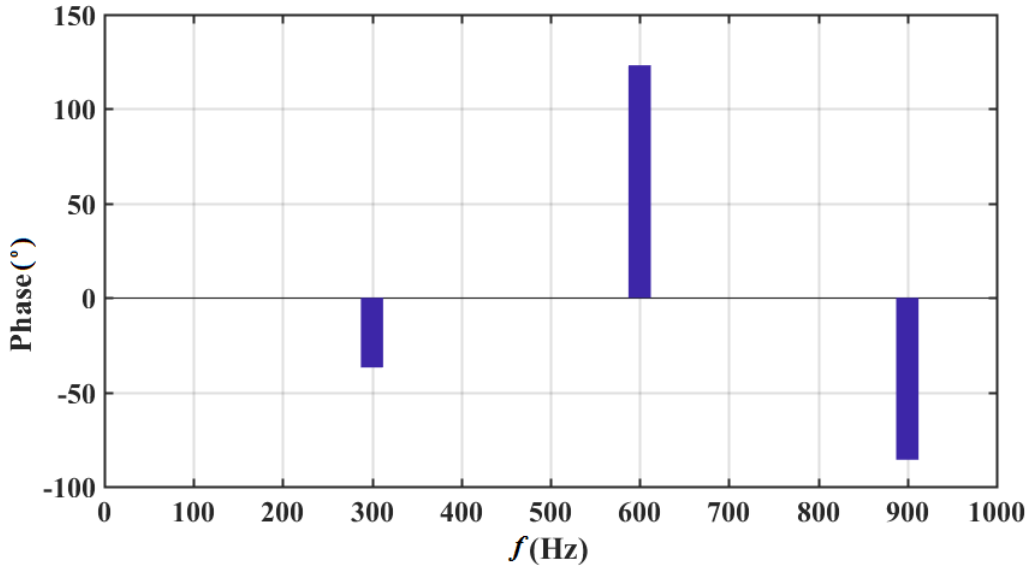

Figure 3-14 Phase spectrum of DC side current for Y-connected transformer

Dominant harmonics of I_{dc} for a Δ-connected transformer are at the same frequency and the same magnitude as a Y-connected one as shown in Figure 3-15.

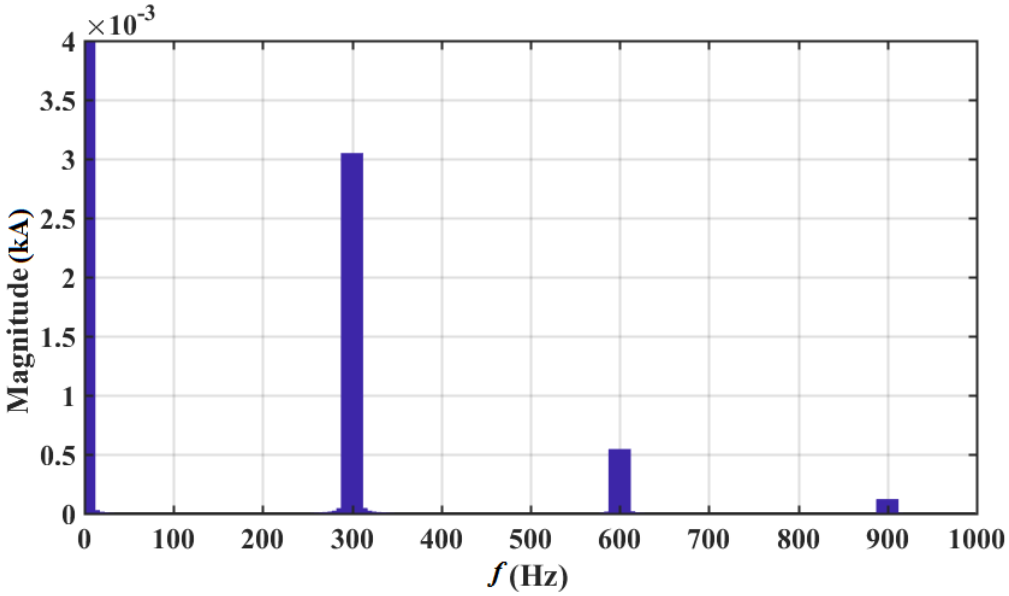

Figure 3-15 Magnitude spectrum of DC side current for Δ-connected transformer

The only difference between Fourier series of the two DC currents appears in their phase information. Figure 3-16 illustrates the phase spectrum of I_{dc} resulting from a Δ-connected transformer. As it can be seen, there is a 180º phase shift between dominant harmonics of order $n = 6(2k\text{-}1)$. Such phase shift results in cancelation of such harmonics when one combines DC voltages of Y- and Δ-connected bridges to build a 12-pulse voltage and the consecutive current.

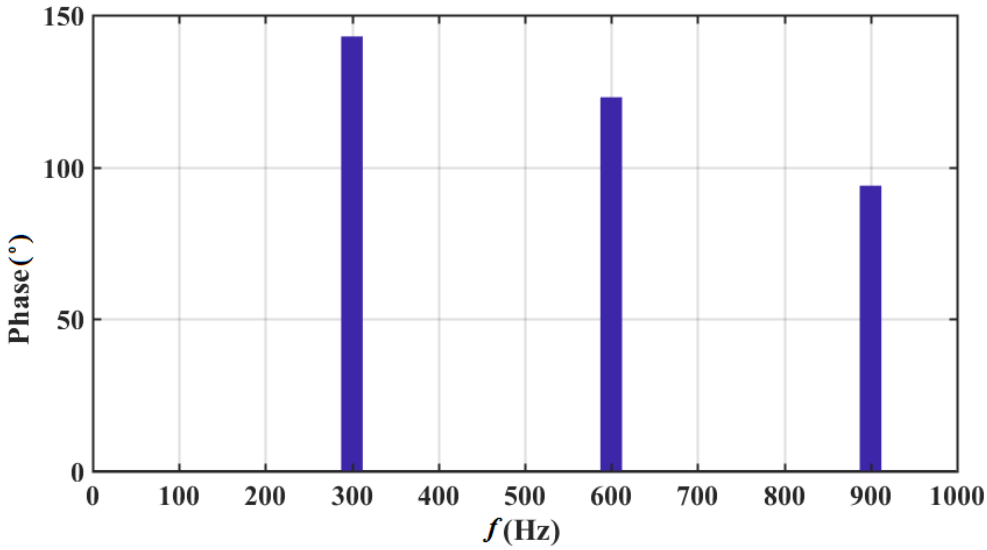

Figure 3-16 Phase spectrum of DC side current for Δ-connected transformer

Figure 3-17 depicts the magnitude of harmonic spectrum extracted from a 12-pulse DC current by considering the interaction between the DC currents of the two 6-pulse bridges. As it can be seen, dominant harmonics now appear only at frequencies of orders $n = 6(2k) = 12k$.

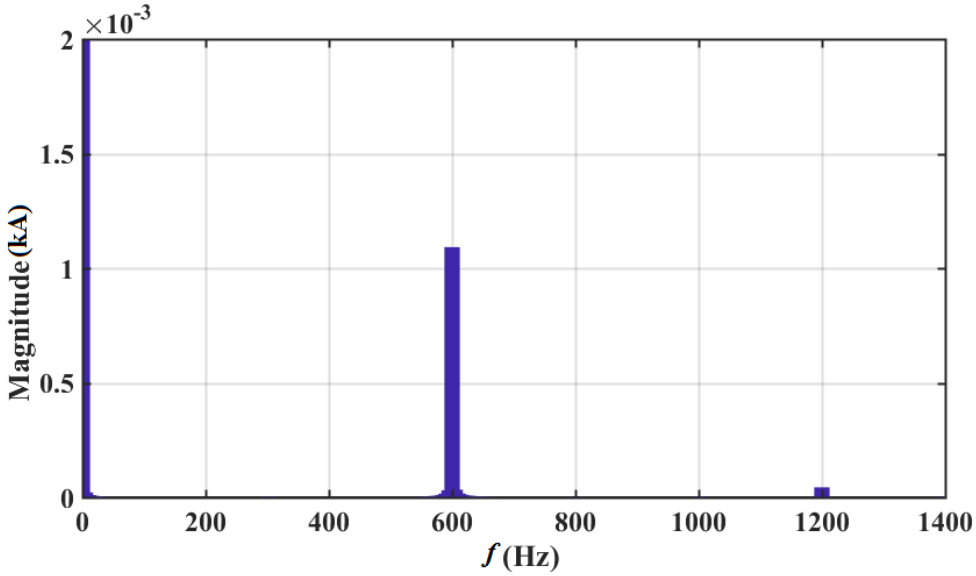

Figure 3-17 Magnitude spectrum of 12-pulse current

Performance of Y- and Δ-connected 6-pulse bridges and their combination as a 12-pulse bridge is investigated and more mathematical details will be presented in chapter 4. A time domain phase shift between generated waveforms of a Y- and Δ-connected bridges can be considered as their main difference. One can model any HVDC system by combining such bridges in different topologies. Therefore, only Y-connection is considered for investigating a 6-pulse bridge performance under various faults.

3.3.2 DC line-to-ground fault

To evaluate the 6-pulse bridge performance under fault condition at DC side, at t = 0.2 s the middle of DC line is grounded for 0.12 s. Since no controller is designed for the bridge, one can expect an increment in DC current as the DC load decreases by 50%.

Figure 3-18 shows how AC and DC voltages are related after fault is applied and the system reaches steady state. Since the AC voltage is strong, there will be no variation in the voltage waveforms during the fault. Therefore, voltage switching functions dose not show any transients due to fault occurrence.

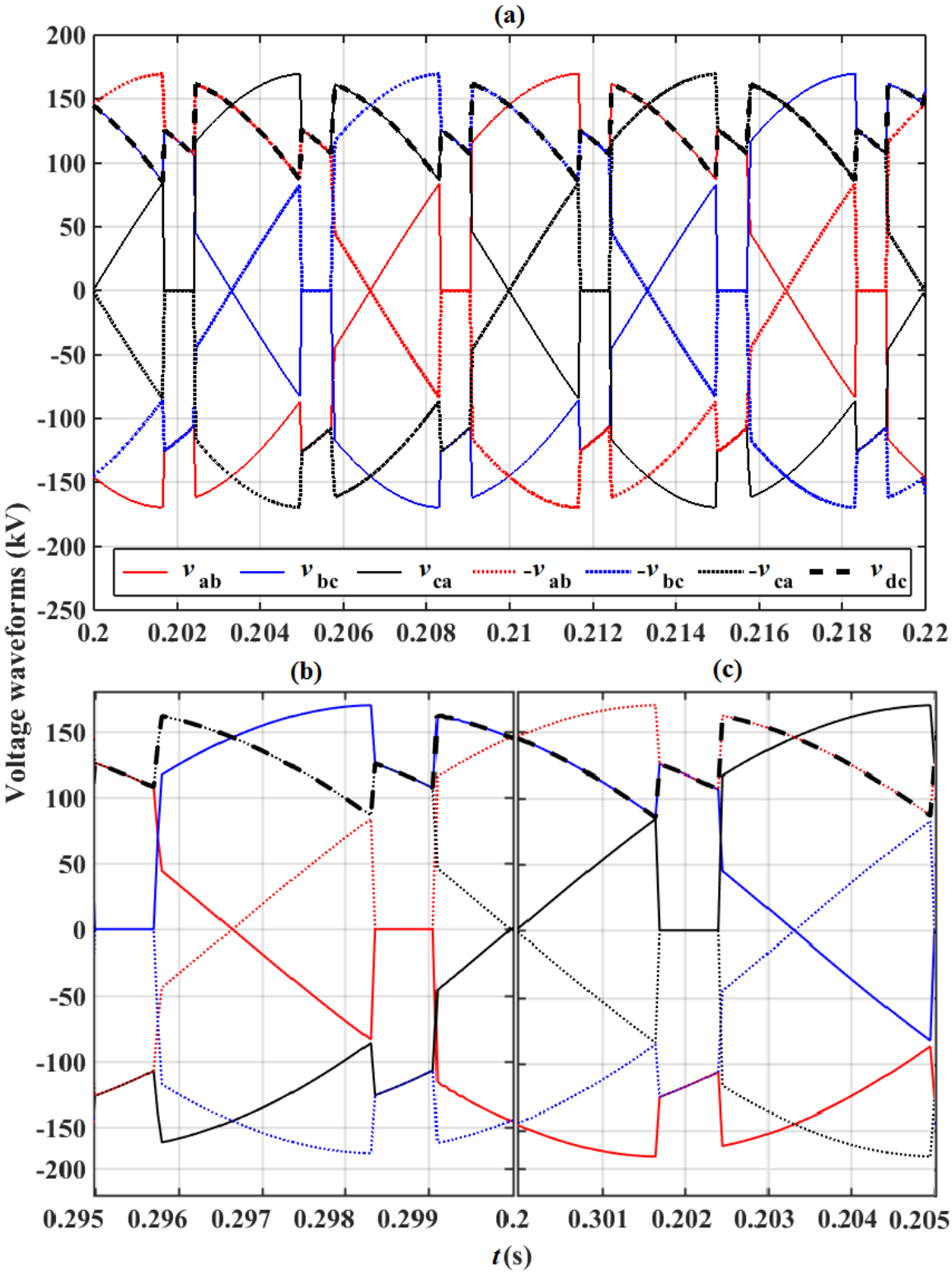

Figure 3-18 DC and AC side voltages for DC Line-to-ground (a) fault duration, (b) pre-fault, and (c) post fault condition

Based on the system conditions, such a DC fault is not making a large difference between the waveforms before and after fault.

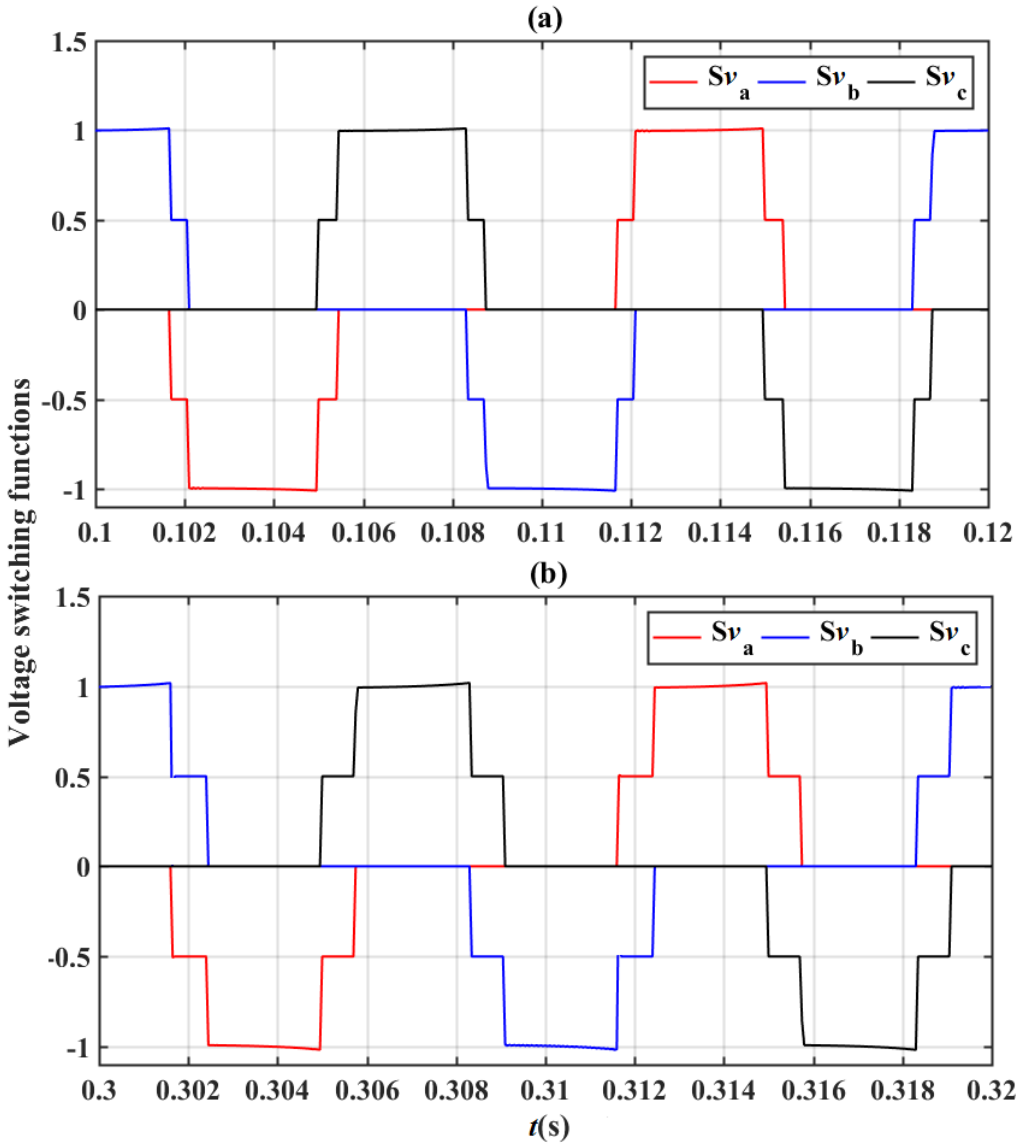

Figure 3-19 Voltage switching functions for (a) pre-fault and (b) post fault conditions of a DC line-to-ground fault

Voltage switching functions can be generated as in Figure 3-19 by building the DC side voltage out of the AC ones. As it can be seen, the non-zero duration of each

switching function increases after a DC line-to-ground fault. However, the three generated waveforms are still balanced and there is 120º phase shift between them.

Applying this DC voltage to the DC load, one can achieve the DC current as in Figure 3-20. Adding the AC current to this figure, one can see how the DC current can be used to generate the AC ones using current switching functions.

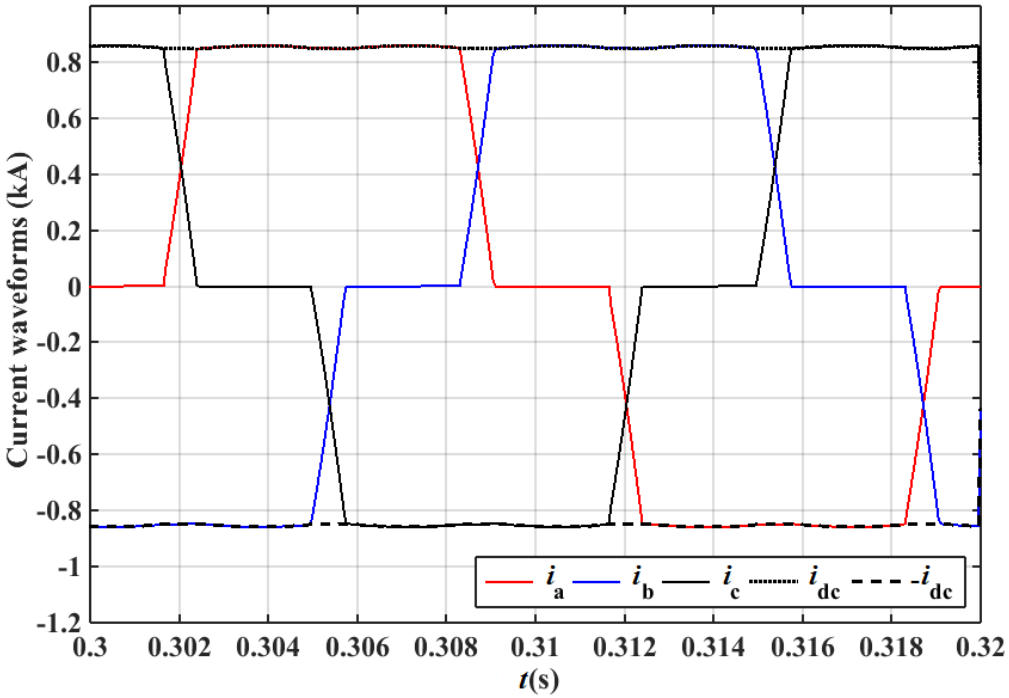

Figure 3-20 DC and AC side currents for DC Line-to-ground fault

Figure 3-21 shows how the current switching functions change after the DC line-to-ground fault.

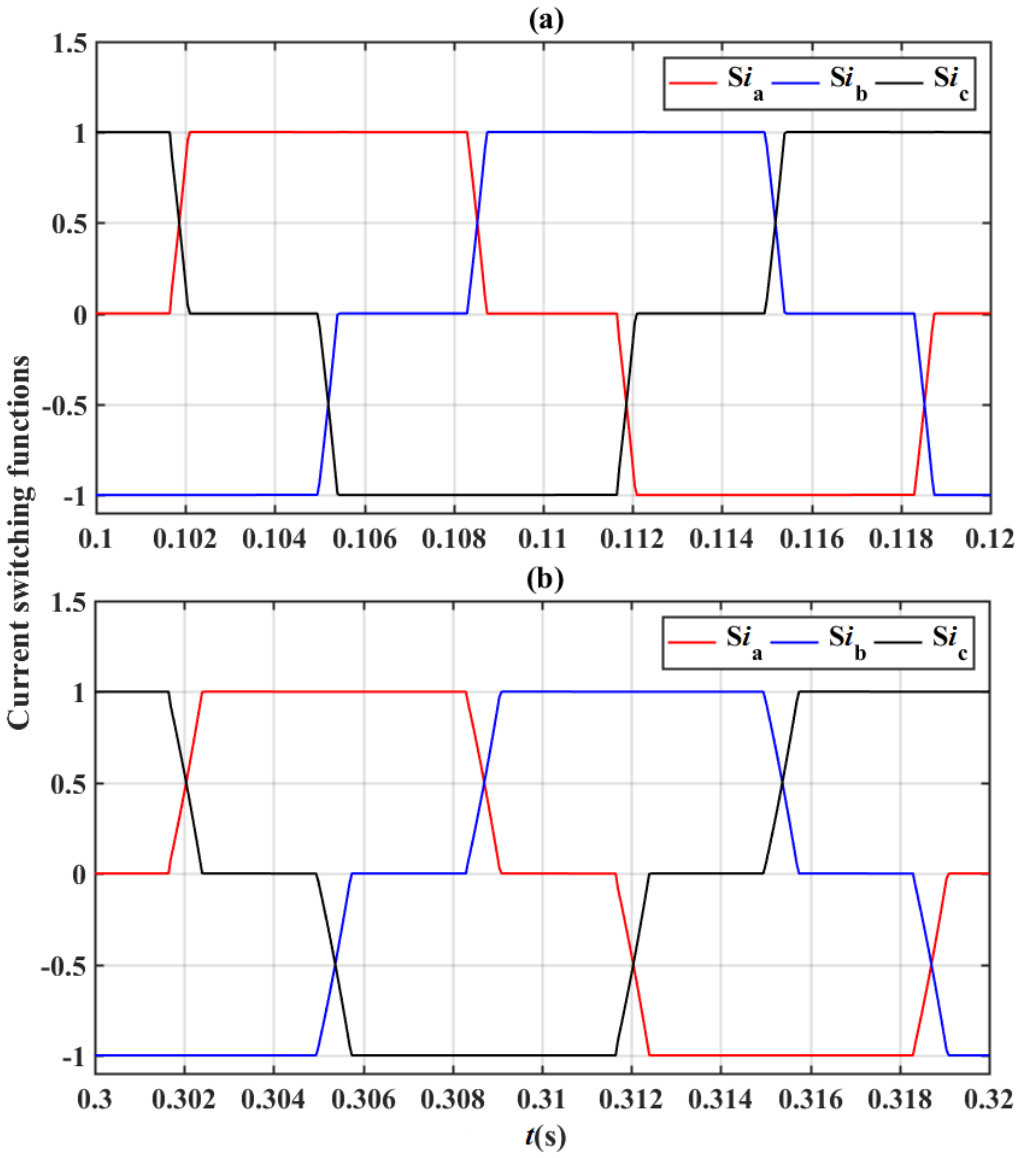

Figure 3-21 Current switching functions for (a) pre-fault and (b) post fault conditions of a DC line-to-ground fault

Switching functions are still balanced and with one of them, one can derive the other two by shifting with ±120º. This is an important feature for switching functions, which can decrease the computational burden of simulations of LCC.

The phase and magnitude spectrum of AC voltages at fundamental frequency on the primary side of the transformer shows no modification in magnitude or phase as in Figure 3-22. This was expected since the AC side voltage is strong and is not much affected by the DC fault. However, a balanced condition is still expected even in absence of a strong AC network. Such information is important, since it will be fed into LCC model as the voltage reference for building relaxed model.

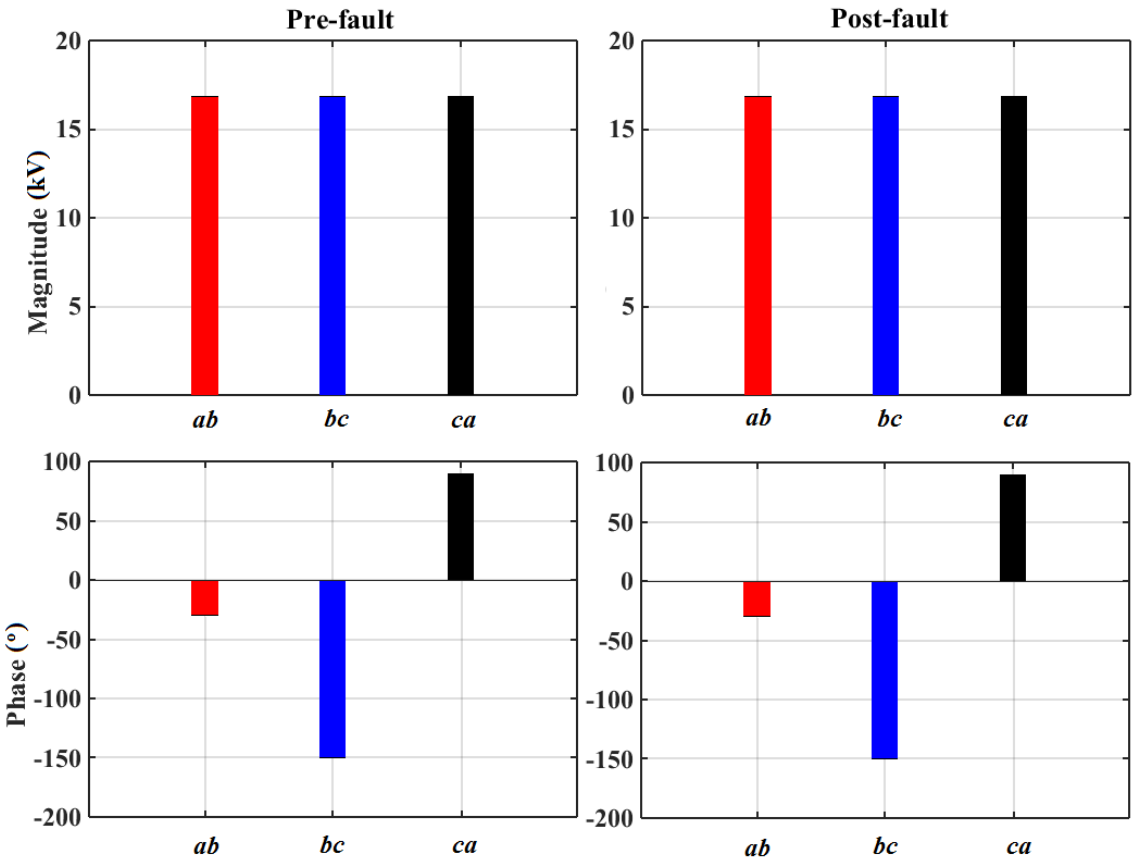

Figure 3-22 Fundamental frequency Fourier analysis of three-phase voltages at transformer primary side for DC line-to-ground fault

3.3.3 Three-phase-to-ground fault

The second operating condition to be investigated is a three-phase-to-ground fault. Such a fault is applied at t = 0.2 s on AC voltage source and lasts 0.12 s. The fault impedance is set in a way to make the AC voltages drop by 50%.

Figure 3-23 shows how AC and DC voltages are related post-fault when fault transients are passed.

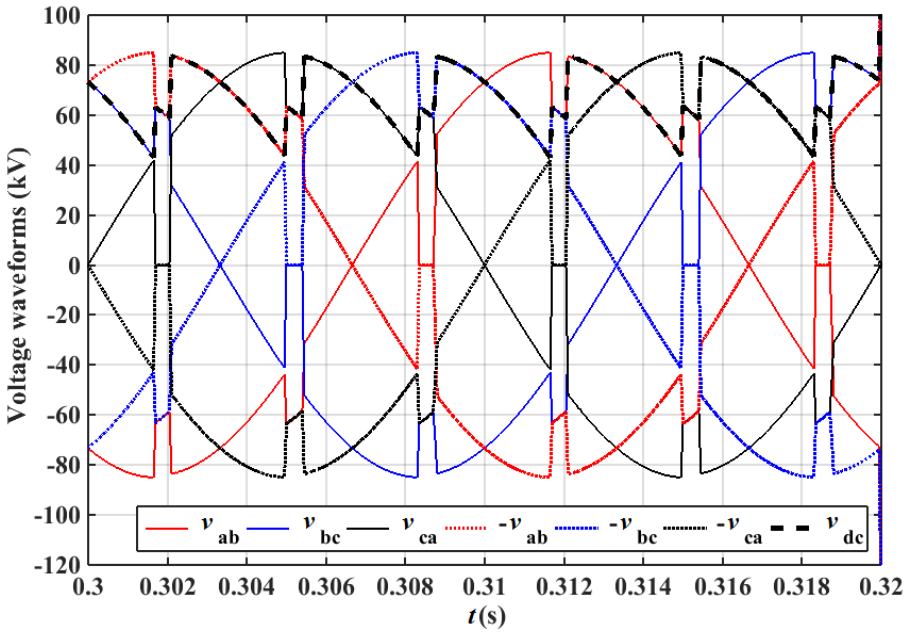

Figure 3-23 DC and AC side voltages for three-phase-to-ground fault

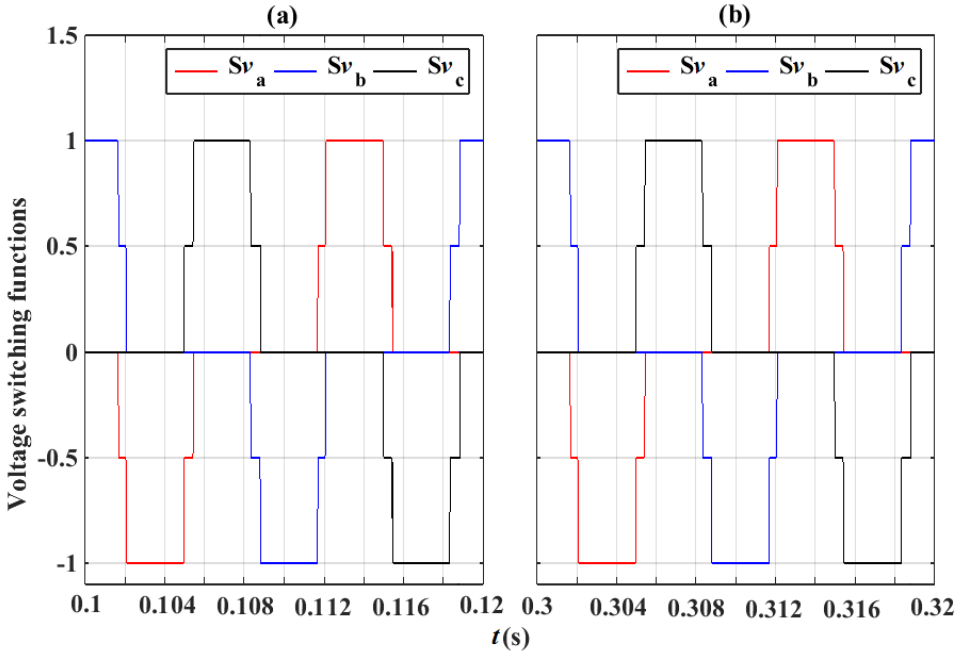

Figure 3-24 Voltage switching functions for (a) pre-fault and (b) post fault conditions of a three-phase-to-ground fault

Voltage switching functions can be generated as in Figure 3-24 by building the DC side voltage out of the AC ones. Since a three-phase-to-ground fault only changes the magnitude of three AC voltages, one can expect no changes in switching functions after the fault. Therefore, one can still benefit from 120º phase shift between three switching functions.

Having the DC voltage one can apply it on DC circuit and measure the DC current as in Figure 3-25. AC side current currents are also included in this figure to compare AC and DC signals for derivation of current switching functions.

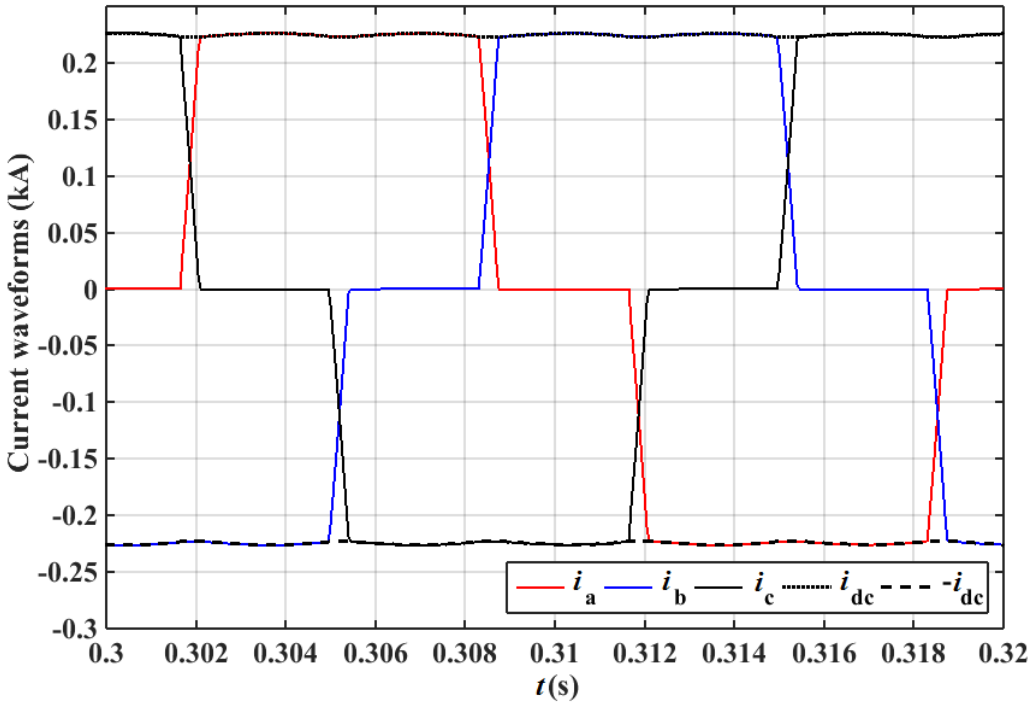

Figure 3-25 DC and AC side currents for three-phase-to-ground fault

Balanced condition is also observed in current waveforms. Therefore, generating a single set of equations between one of the AC side and DC side currents will be enough for generating all three currents switching functions. To do so, one can apply a simple ±120° phase shift. Figure 3-26 shows how the current switching functions remain the same after a three-phase-to-ground fault.

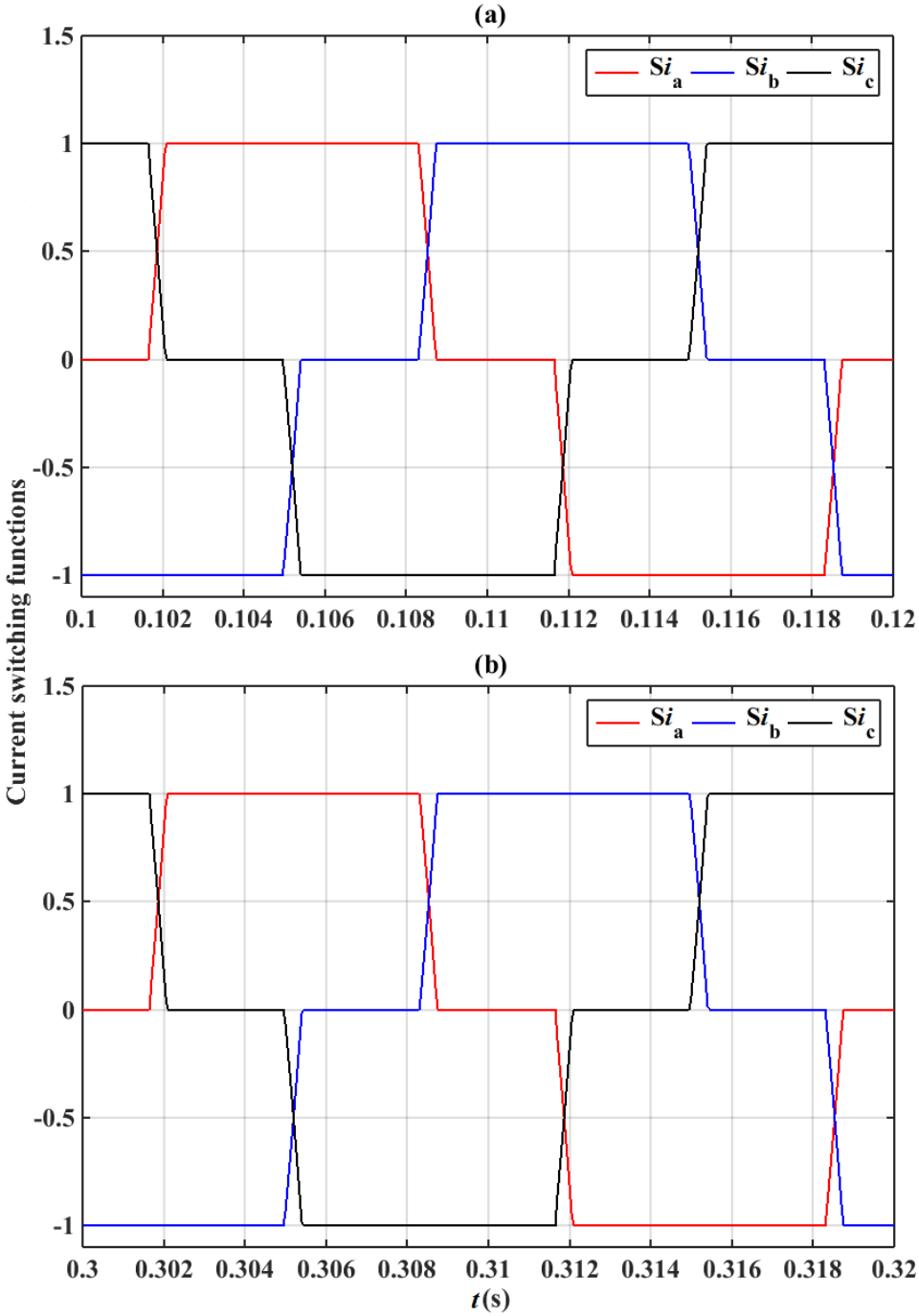

Figure 3-26 Current switching functions for (a) pre-fault and (b) post fault conditions of a three-phase-to-ground fault

The phase and magnitude of AC voltages at fundamental frequency on primary side of the transformer shows decrement in magnitude spectrum as in Figure 3-27 after fault. Phase spectrum does not show any changes after fault application.

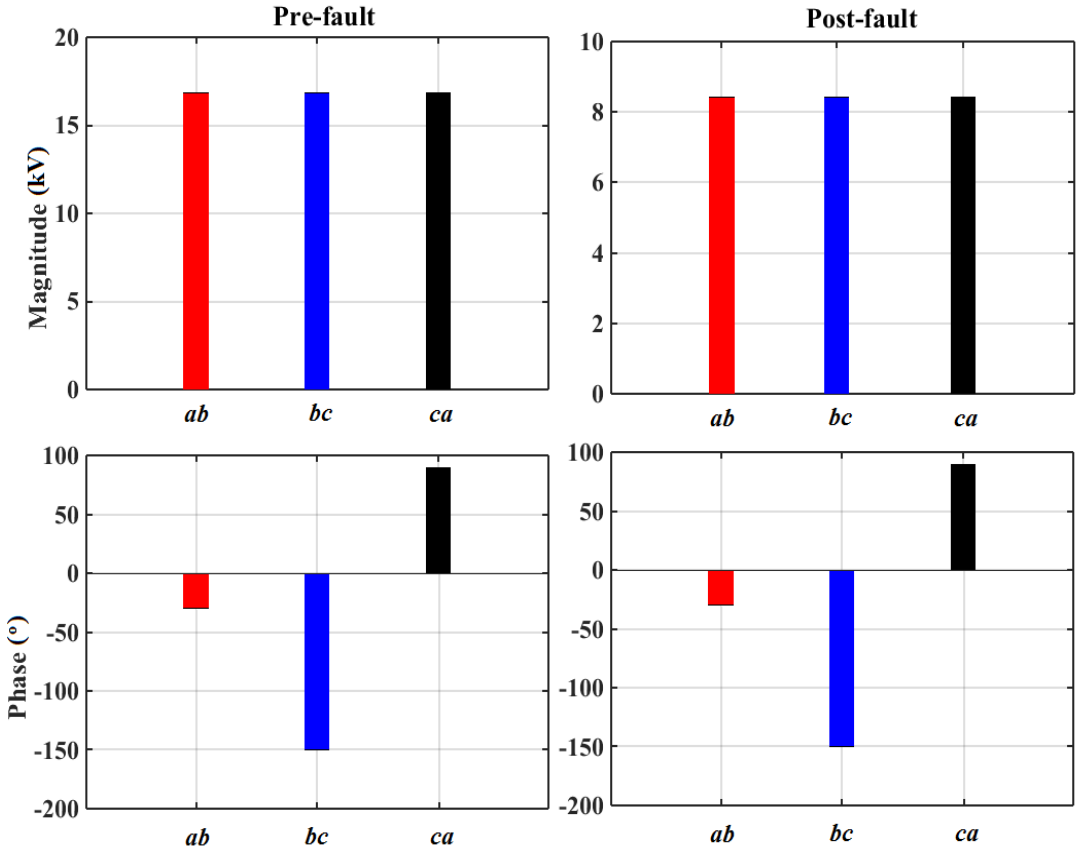

Figure 3-27 Fundamental frequency Fourier analysis of three-phase voltages at transformer primary side for three-phase-to-ground fault

3.3.4 Two-phase-to-ground fault

Deriving switching functions under unbalanced operating conditions is one of the main challenges in using purely mathematical equations for modeling 6-pulse bridge converters. To investigate the effect of such operating conditions, a two-phase-to-ground fault is applied at t = 0.2 s on AC voltage source and lasts 0.12 s. Fault resistance is set in

a way to cause voltages at phases b and c to drop to half of their initial values. As Figure 3-28 shows development of switching functions for this case is quite complicated.

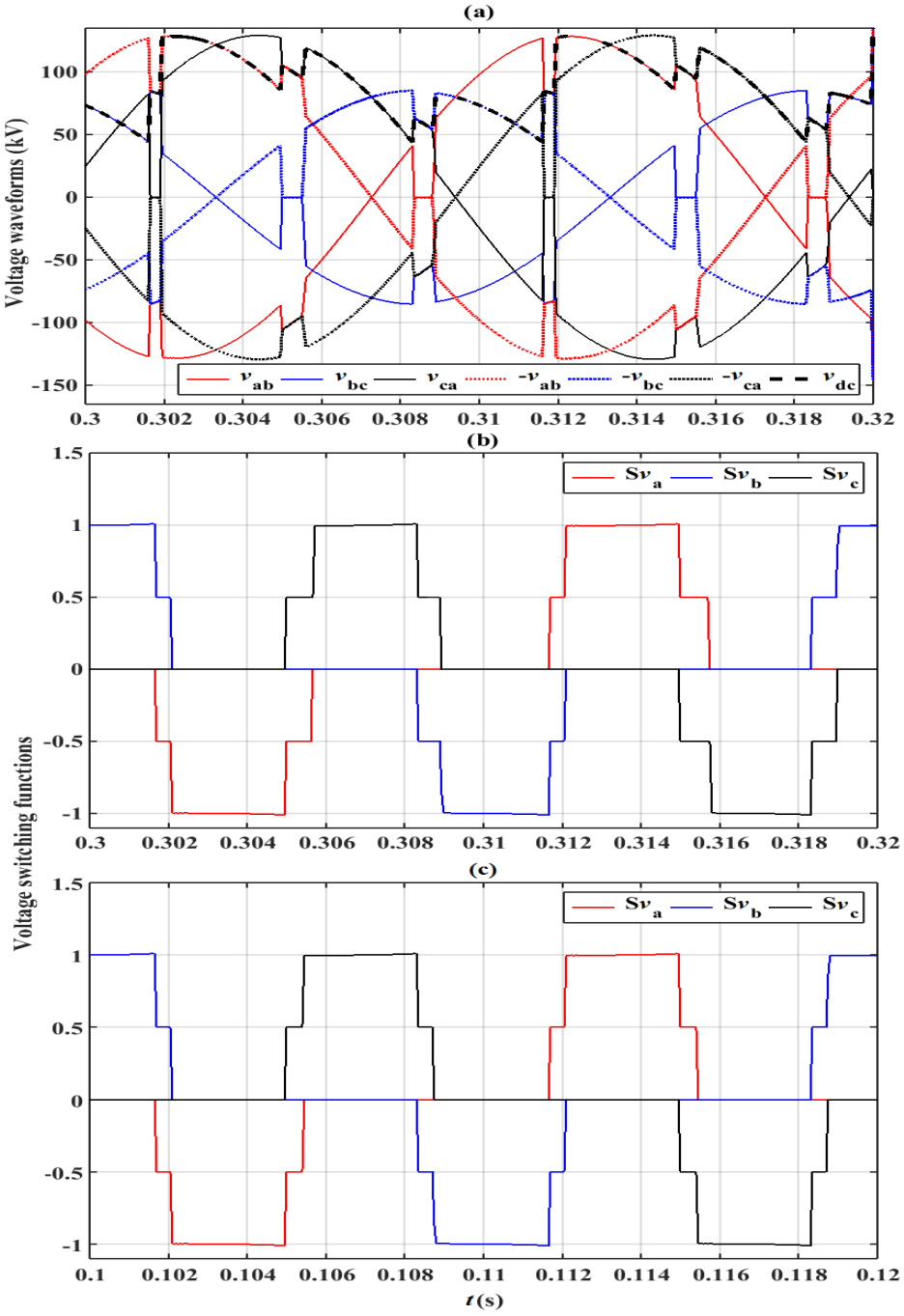

Figure 3-28 DC and AC side (a) voltages and switching functions during (b) post- & (c) pre-fault durations for two-phase-to-ground fault

According to Figure 3-28, the voltage switching functions are no longer symmetrical. Therefore, one cannot benefit from 120º phase shift and needs three different sets of equations for each single switching function. Deriving three equations instead of one will imply additional computational burden on developed model.

Unlike voltage waveforms, AC and DC side currents follow a much simpler pattern as in Figure 3-29.

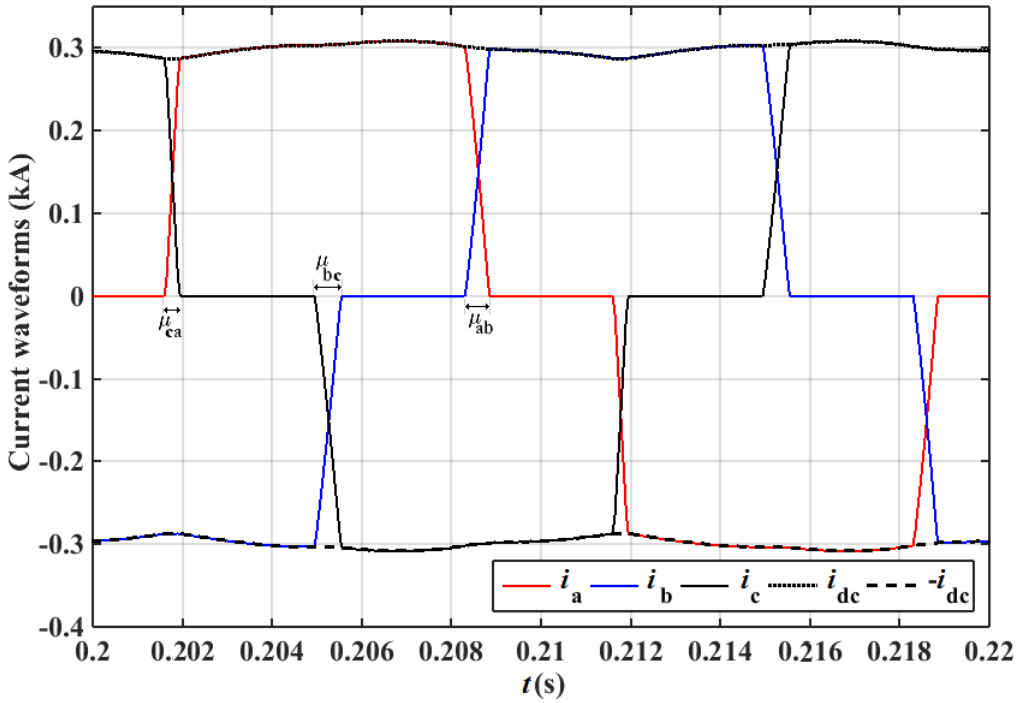

Figure 3-29 DC and AC side currents for two-phase-to-ground fault

Deriving current switching functions would be an easier task in comparison with voltage ones. One can easily divide each AC current by the DC one to find the current switching function for that phase. The effect of asymmetrical operating condition is shown in the measured overlap angles on current switching functions. The measured overlap angles μ_{ca}, μ_{bc}, and μ_{ab} are equal to 7.2º, 10.8º, and 9º respectively.

In the case of a two-phase-to-ground fault at phases *b* and *c* at the primary side of the transformer, one can expect changes in magnitude spectrum for all the line-to-line voltages. However, the important fact that the phase angle of the fundamental component for *bc* voltage remains constant after fault is to be noted.

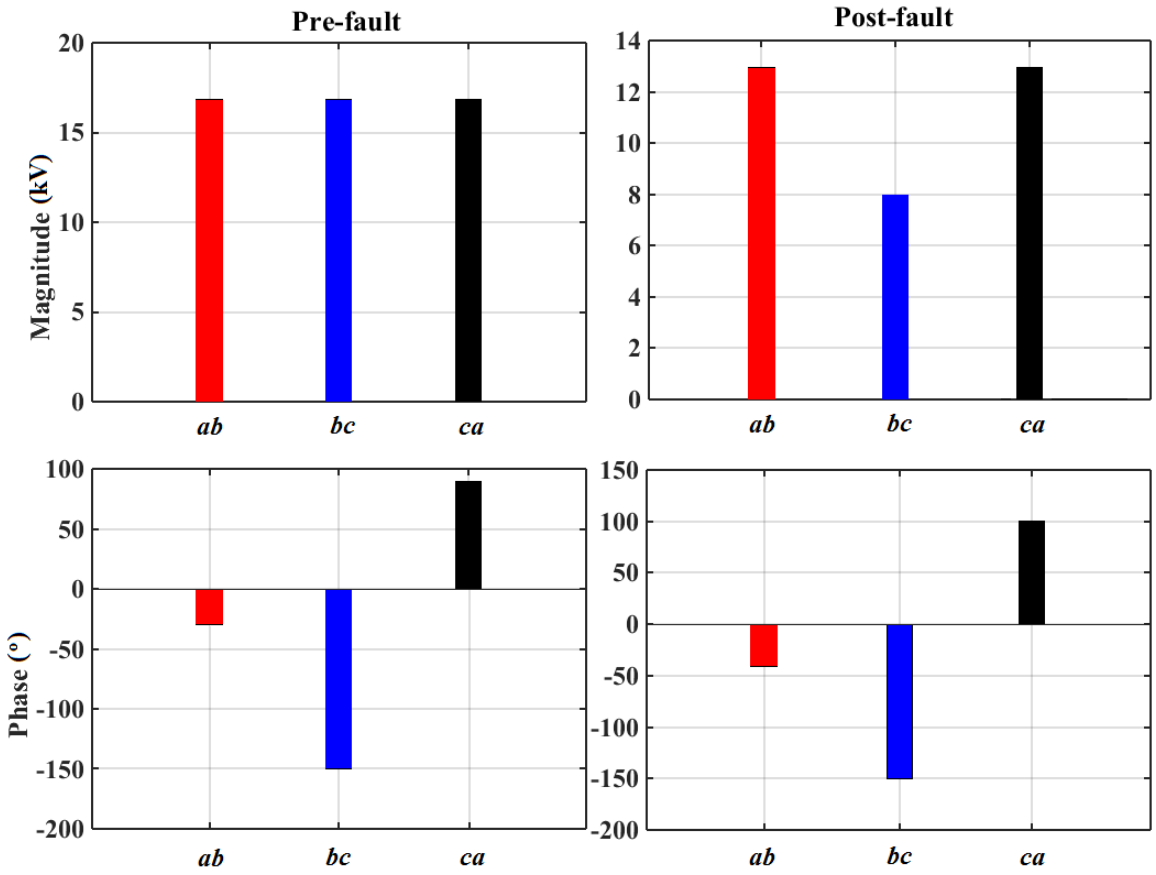

Figure 3-30 Fundamental frequency Fourier analysis of three-phase voltages at transformer primary side for two-phase-to-ground fault

3.3.5 Single-phase-to-ground fault

To further investigate the effect of unbalanced conditions on LCC system performance, a single-phase-to-ground fault is applied on phase a at t = 0.2 s for 0.12 s. Due to this fault the voltage at phase a drops to half of its initial value.

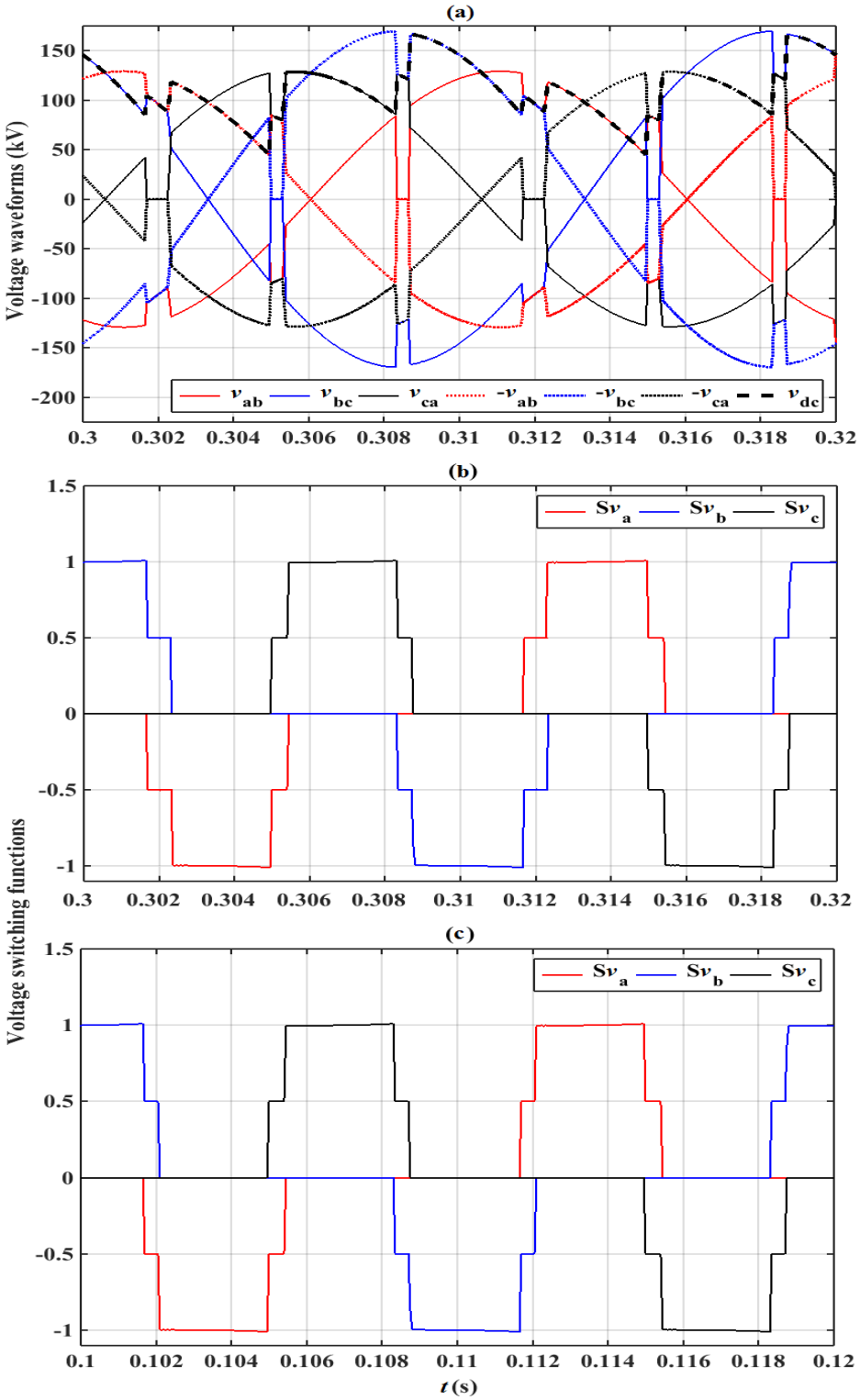

Figure 3-31 DC and AC side (a) voltages and switching functions during (b) post- & (c) pre-fault durations for single-phase-to-ground fault

According to Figure 3-31, voltage switching functions under unbalanced operating conditions become asymmetrical. Therefore, one needs to derive three different equations, one for each phase, for modeling LCC switching performance during this unbalanced fault.

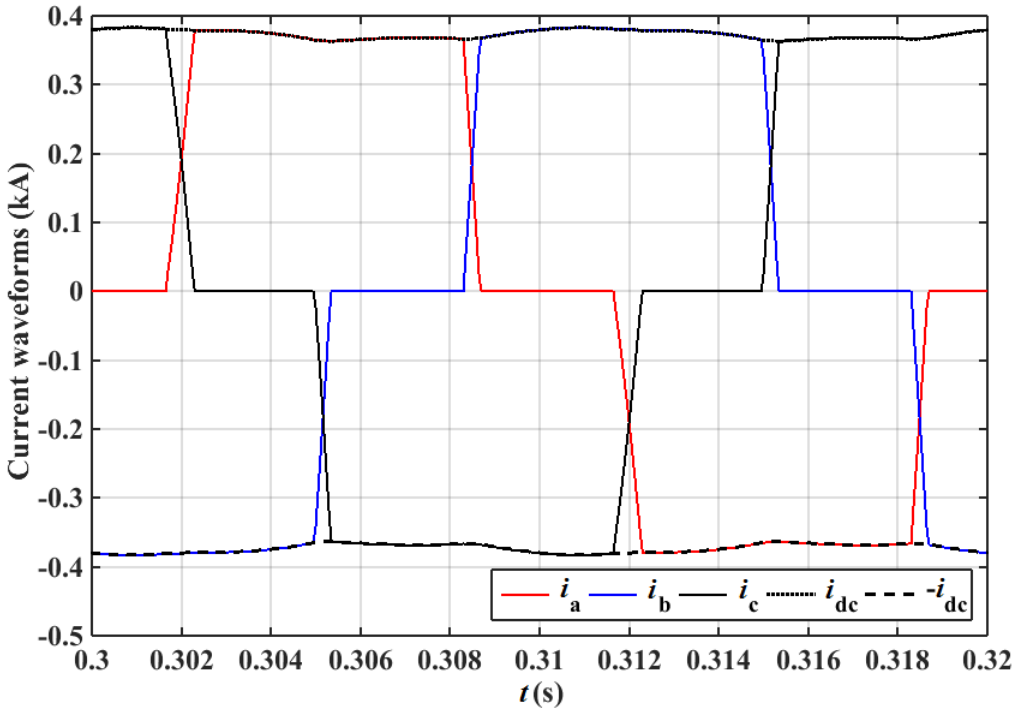

Figure 3-32 DC and AC side currents for single-phase-to-ground fault

Figure 3-22 illustrates the AC and DC side current waveforms. Due to single-phase-to-ground fault at AC busbar, one can expect AC and DC side currents to drop at the terminals of the 6-pulse bridge. The effect of such unbalanced fault on the symmetry of the three AC waveforms is not readily visible. Such negligible effect is due to the system parameters. One way to maximize such effect would be increasing the leakage inductance of the transformer to values close to 0.9 pu, which is not a realistic one. However, such approach can magnify the effect of unbalanced operating condition.

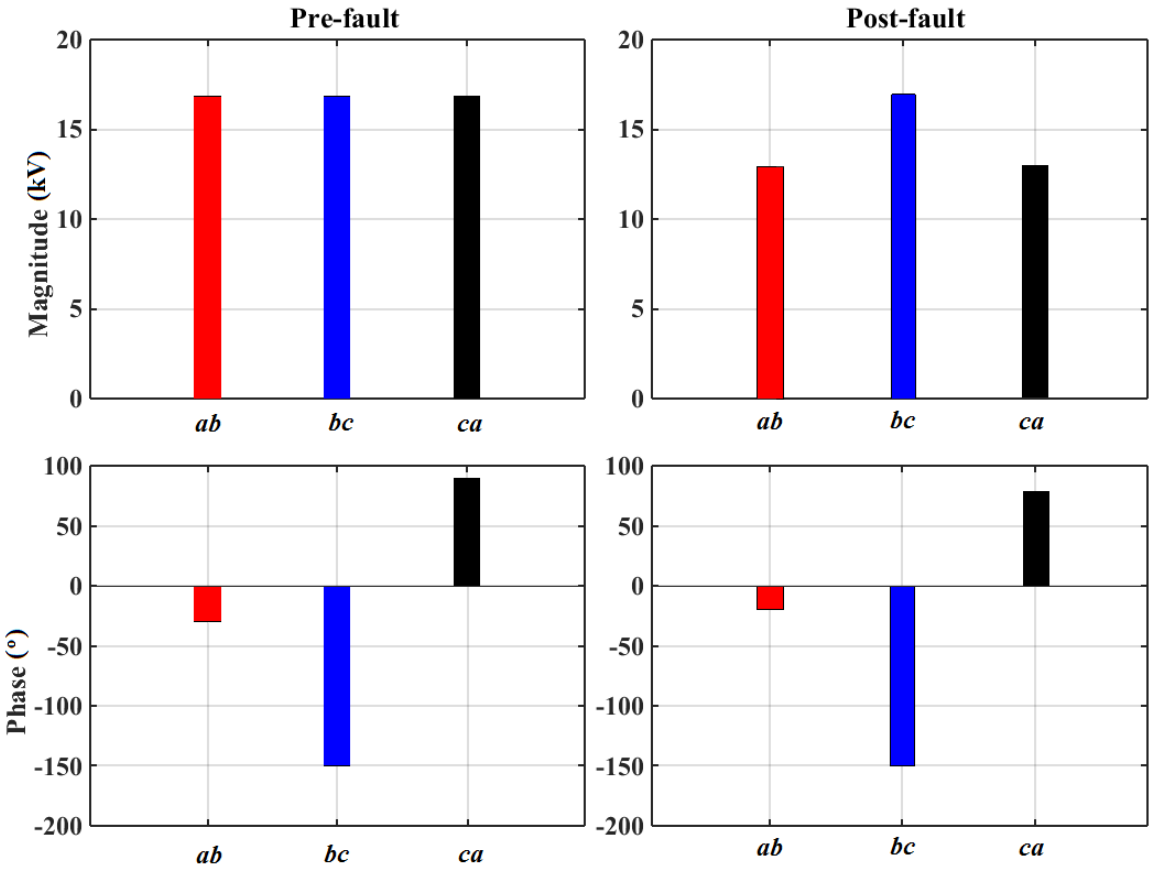

Figure 3-33 Fundamental frequency Fourier analysis of three-phase voltages at transformer primary side for single-phase-to-ground fault

Fourier transform of AC busbar voltage waveforms for pre- and post-fault time intervals shows that the magnitude and phase spectrum of *bc* does not change. Such information can be applied to derive a modified switching function later on in chapter 4.

3.4 Chapter Summary

Various sub-systems of an LCC-HVDC system were introduced based on different examples and establishment of their mathematical background was postponed to the next chapter. The 6-pulse bridge converter as the main building block of an LCC system was

studied in detail. In this regard, various operating conditions were applied on different LCC configurations and their effect on AC and DC waveforms was reported. Furthermore, the concept of switching functions was introduced as a purely mathematical approach for modeling LCC systems. Finally, the challenges toward such modeling approach under different operating conditions were investigated.

Chapter 4

Dynamic Phasor Modeling of LCC-HVDC Systems

4.1 Introduction

Dynamic phasors are a proper response to the need for EMT simulation of large electric networks including switching converters and fast-acting controllers of an LCC system by offering average-value models for converters. In this chapter, a new dynamic phasor-based model is developed for an LCC-HVDC system for normal as well as abnormal operating modes such as system imbalances and commutation failure. The ability to include a user-defined number of harmonics and improved computational efficiency are important features of the developed model. To achieve such a model, the concept of voltage and current switching functions introduced in Chapter 3 must be extended to different operating conditions of LCC system and its effect on the valve control must be clarified.

4.2 LCC-HVDC Valve Control

In order to derive time domain equations between AC and DC side voltages and currents of an LCC, one can start by looking at operating conditions that result in forward biasing of each valve. Since the valves are thyristor-based, whenever the voltage of the anode is greater than that of the cathode and a firing command is received (with a delay angle of α), the valve would start conducting. This current conduction continues as long as it remains positive. Considering three-phase voltages under balanced conditions as in (4-1), the DC side voltage (V_d) and AC side current at phase a (i_a) are as shown in Figure 4-1.

$$\begin{cases} v_a = V_m \sin(\omega t + \pi/6) \\ v_b = V_m \sin(\omega t - \pi/2) \\ v_c = V_m \sin(\omega t + 5\pi/6) \end{cases} \tag{4-1}$$

As Figure 4-1 shows DC side voltage is a combination of all three-phase voltage at AC side of the converter and their inverse. Finding functions that describe this combination results in deriving a time-domain expression for voltage switching functions. The current switching functions can be derived in the same manner by looking at AC side three-phase current and how they are related to the single DC current.

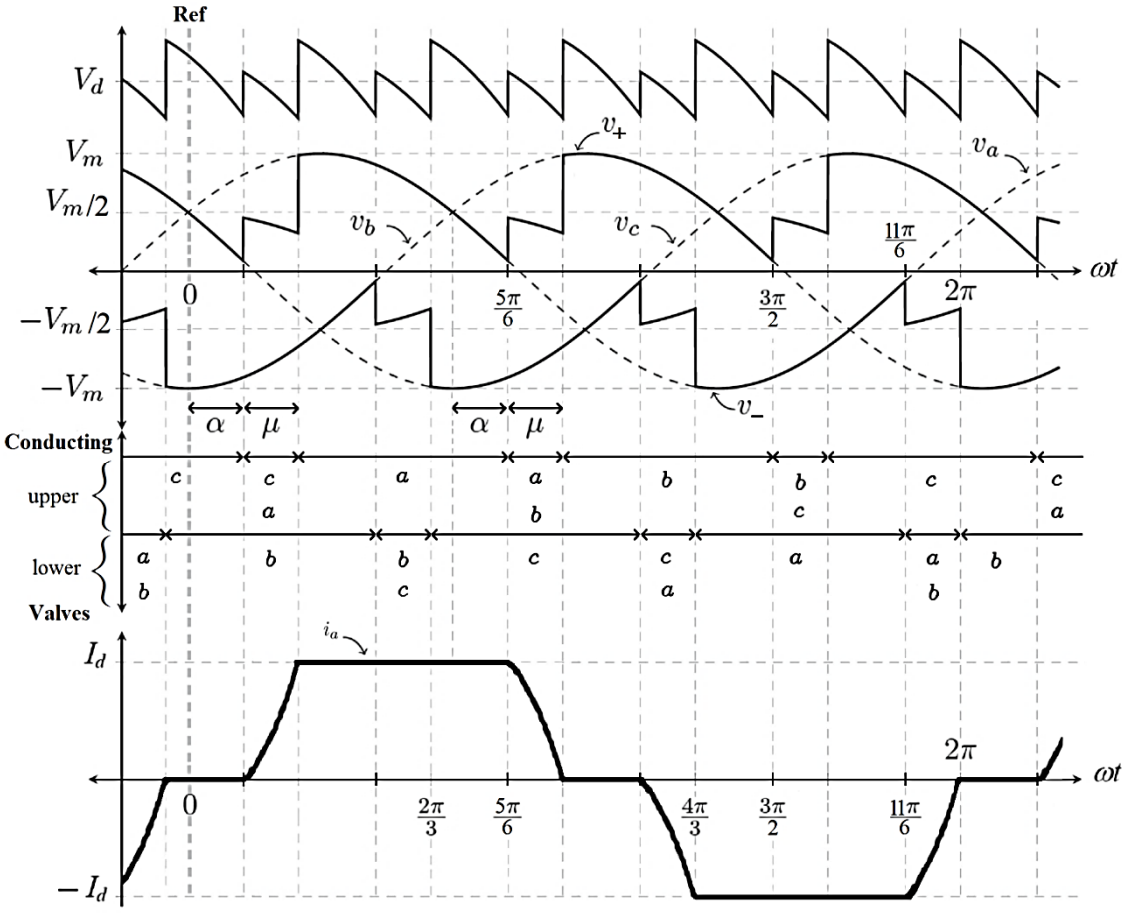

Figure 4-1 Voltage and current waveforms of a 6-pulse Graetz bridge under balanced condition

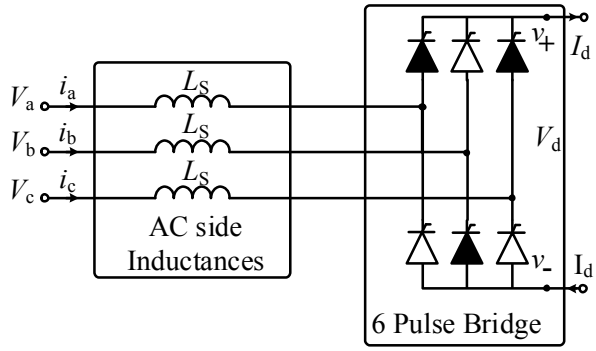

Figure 4-2 Switching sequence during first overlap at upper side valves

During the time periods when only one switch is on, it is easy to derive such equations. The only challenging part is when an overlap (also known as commutation period) happens, which is when outgoing and incoming switches switch over the task of

current conduction. The first overlap happens between phases *a* and *c* at the upper side switches as in Figure 4-2.

The effect of AC side inductances are accumulated in L_S. Starting with voltage switching functions, one can replace two AC voltages connected to v_+ with their Thevenin equivalent circuits as in Figure 4-3. Conducting valves will be replaced with a small resistance R_{on}.

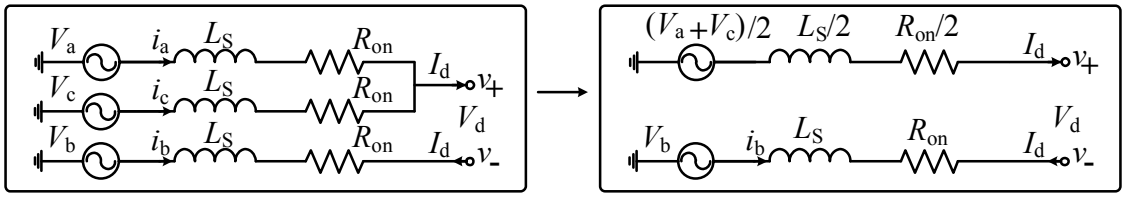

Figure 4-3 Thevenin equivalent circuit for the two overlapping phases

Finally DC side voltage can be calculated by subtracting negative side voltage from positive one as in (4-2).

$$V_d = V_+ - V_- = \frac{v_{ab}}{2} - \frac{v_{bc}}{2} - \frac{3}{2} R_{on} I_d \tag{4-2}$$

Using (4-2) one can establish voltage switching functions based on line-to-line AC voltage v_{ab} as follows.

$$Sv_{ab}(\theta) = \begin{cases} 1/2 & \alpha \le \theta < \alpha + \mu \quad \& \quad \pi/3 + \alpha \le \theta < \pi/3 + \alpha + \mu \\ 1 & \alpha + \mu \le \theta < \pi/3 + \alpha \\ -1/2 & \pi + \alpha \le \theta < \pi + \alpha + \mu \quad \& \quad 4\pi/3 + \alpha \le \theta < 4\pi/3 + \alpha + \mu \\ -1 & \pi + \alpha + \mu \le \theta < 4\pi/3 + \alpha \\ 0 & otherwise \end{cases} \tag{4-3}$$

It can be proved that voltage switching functions for v_{bc} and v_{ca} are achievable by shifting $Sv_{ab}(\theta)$ by $-2\pi/3$ and $2\pi/3$, respectively. One can also find DC side voltage using these switching functions for any given AC voltages as in (4-4).

$$V_d = Sv_{ab}(\theta)\times v_{ab} + Sv_{bc}(\theta)\times v_{bc} + Sv_{ca}(\theta)\times v_{ca} \tag{4-4}$$

Having found voltage switching functions, one only needs the current switching functions to achieve a comprehensive time-domain model of LCC. Once again, the only challenging part would be the overlap or commutation time interval. Considering the system's equivalent circuit during first overlap for i_a as in Figure 4-3, the following equations can be established.

$$i_a + i_c = I_d \rightarrow \frac{di_a}{dt} + \frac{di_c}{dt} = 0 \rightarrow \omega_0 L_S \frac{di_a}{d\theta} + \omega_0 L_S \frac{di_c}{d\theta} = 0 \rightarrow X_S \frac{di_a}{d\theta} + X_S \frac{di_c}{d\theta} = 0 \tag{4-5}$$

$$v_a - L_S \frac{di_a}{dt} + L_S \frac{di_c}{dt} - v_c = 0 \tag{4-6}$$

Combining the last two equations, one can find an equation between AC line voltage and current as follows.

$$v_{ac} = L_S\left(\frac{di_a}{dt} - \frac{di_c}{dt}\right) = 2L_S \frac{di_a}{dt} = 2X_S \frac{di_a}{d\theta} \Rightarrow \frac{di_a}{d\theta} = \frac{v_{ac}}{2X_S} \tag{4-7}$$

Assuming that line-to-line voltages at AC side are purely sinusoidal and the system is working under balanced condition, one can find $i_a(\theta)$ by integrating (4-7).

$$i_a(\theta) = \frac{1}{2X_S}\int_{\alpha}^{\alpha+\theta} v_{ac}(\theta)d\theta = \frac{1}{2X_S}\int_{\alpha}^{\alpha+\theta} \sqrt{3}V_m \sin(\theta)d\theta = \frac{\sqrt{3}Vm}{2X_S}(\cos(\alpha) - \cos(\alpha+\theta)) \tag{4-8}$$

At the end of the first overlap interval the angle θ and current $i_a(\theta)$ become equal to μ and I_d respectively. This would result in DC side current calculation during the overlap interval as follows.

$$i_a(\theta)\big|_{\theta=\mu} = I_d \Rightarrow \frac{\sqrt{3}Vm}{2X_S}(\cos(\alpha) - \cos(\alpha+\mu)) = I_d \tag{4-9}$$

Using (4-9) one can with a formula for μ, $i_a(\theta)$, and $i_c(\theta)$ based on I_d during the overlap angle as follows.

$$\mu = \cos^{-1}(\cos(\alpha) - \frac{2X_S I_d}{\sqrt{3}Vm}) - \alpha \tag{4-10}$$

$$i_a(\theta) = \frac{\cos(\alpha) - \cos(\alpha + \theta)}{\cos(\alpha) - \cos(\alpha + \mu)} I_d \tag{4-11}$$

$$i_c(\theta) = \frac{\cos(\alpha + \theta) - \cos(\alpha + \mu)}{\cos(\alpha) - \cos(\alpha + \mu)} I_d \tag{4-12}$$

It can be shown that for other overlap intervals the same equations are achievable. Finally, current switching functions relating DC side current to the AC side ones for phase *a* would be as in (4-13). It would be easy to prove that current switching functions for i_b and i_c can be achieved by shifting $Si_a(\theta)$ by $-2\pi/3$ and $2\pi/3$, respectively.

$$Si_a(\theta) = \begin{cases} \dfrac{\cos(\alpha) - \cos(\theta)}{\cos(\alpha) - \cos(\alpha + \mu)} & \alpha \le \theta < \alpha + \mu \\ 1 & \alpha + \mu \le \theta < 2\pi/3 + \alpha \\ \dfrac{\cos(\theta - 2\pi/3) - \cos(\alpha + \mu)}{\cos(\alpha) - \cos(\alpha + \mu)} & 2\pi/3 + \alpha \le \theta < 2\pi/3 + \alpha + \mu \\ \dfrac{\cos(\theta - \pi) - \cos(\alpha)}{\cos(\alpha) - \cos(\alpha + \mu)} & \pi + \alpha \le \theta < \pi + \alpha + \mu \\ -1 & \pi + \alpha + \mu \le \theta < 5\pi/3 + \alpha \\ \dfrac{\cos(\alpha + \mu) - \cos(\theta - 5\pi/3)}{\cos(\alpha) - \cos(\alpha + \mu)} & 5\pi/3 + \alpha \le \theta < 5\pi/3 + \alpha + \mu \\ 0 & otherwise \end{cases} \tag{4-13}$$

It is worth mentioning that (4-14) is valid during balanced operating conditions and not otherwise.

$$\begin{cases} i_a(\theta) = Si_a(\theta) \times I_d \\ i_b(\theta) = Si_b(\theta) \times I_d \\ i_c(\theta) = Si_c(\theta) \times I_d \end{cases} \tag{4-14}$$

It is possible to derive dynamic phasor equivalents of the above expression by simply applying the respective principles. In this regard, dynamic phasor equivalents for voltage and current switching functions would be as follows applying the concept in (2-8).

$$\left\langle Sv_{ab}(\theta)\right\rangle_k = \begin{cases} 0 & for \quad k = even \\ \dfrac{e^{-jk\alpha}}{jk2\pi}(1-e^{-jk\pi/3})(1+e^{-jk\mu}) & for \quad k = odd \end{cases} \tag{4-15}$$

$$\left\langle Si_a(\theta)\right\rangle_k = \begin{cases} 0 & for \quad k = even \\ \dfrac{e^{-jk\alpha}}{j\pi}\dfrac{(1-e^{-jk2\pi/3})(\beta_{Ik}+\beta_{IIk})}{(\cos(\alpha)-\cos(\alpha+\mu))} & for \quad k = odd \end{cases} \tag{4-16}$$

where β_{IK} and β_{IIK} are as follows.

$$\beta_{Ik} = \frac{\cos(\alpha)-e^{-jk\mu}\cos(\alpha+\mu)}{k} \tag{4-17}$$

$$\beta_{IIk} = \begin{cases} \dfrac{e^{-j\alpha}(e^{-j2\mu}-1)-j2\mu e^{j\alpha}}{4} & k=1 \\ \dfrac{k\cos(\alpha)+j\sin(\alpha)-e^{-jk\mu}(k\cos(\alpha+\mu)+j\sin(\alpha+\mu))}{1-k^2} & otherwise \end{cases} \tag{4-18}$$

Finally, the proposed DP-based six-pulse converter model is depicted in Figure 4-4(a). The DP interface block is a simple transfer function based on (2-7) and (2-8), which take a time domain variable to dynamic phasor one and vice versa.

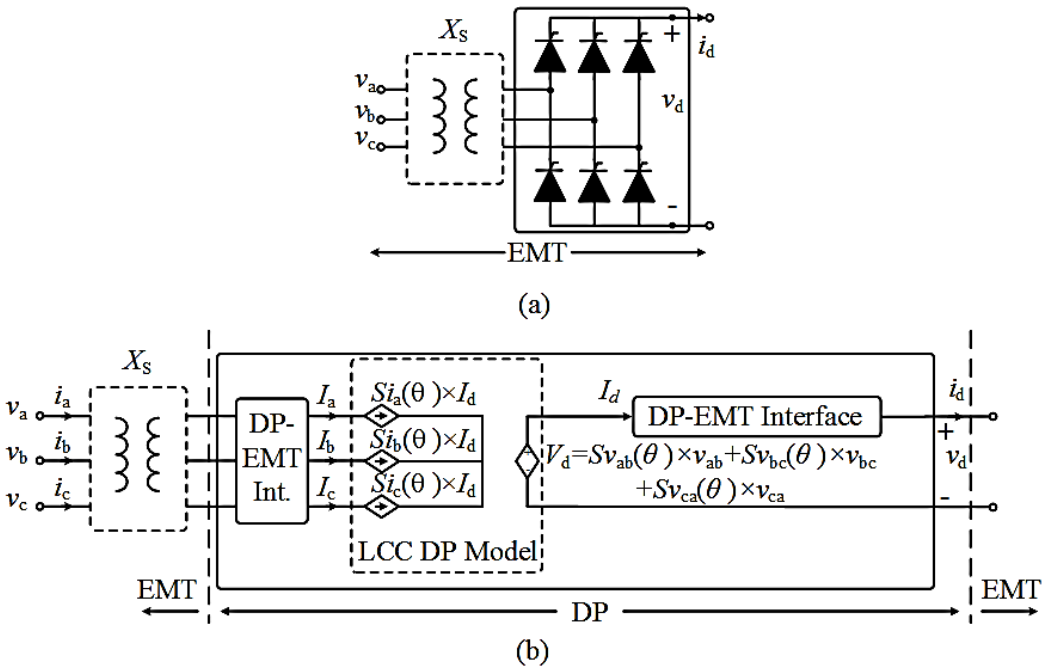

Figure 4-4 Six-pulse LCC models; (a) switch-based model (b) dynamic phasor-based model

As shown the model is readily structured for embedding in an EMT simulator, i.e., the converter model's AC and DC ports are interfaced to arbitrary AC and DC networks in an EMT simulation. The converter is modelled as a controlled voltage source on the DC side and a set of controlled current sources on the AC side. The converter's operation is represented using mathematical switching functions that relate the AC and DC quantities, and are in terms of dynamic phasors rather than natural *abc* quantities. Use of dynamic phasors, rather than original phase-domain switching functions, allows (i) selectivity in terms of inclusion of harmonics, and (ii) use of large simulation time-steps without adversely affecting the accuracy of representing low-frequency transients.

4.3 Relaxed DP Model of LCC

The expressions in (4-15)-(4-18) are valid only under normal and balanced conditions. An LCC-HVDC system may operate under unbalanced AC system conditions or experience commutation failure due to severe faults. Therefore, the model needs to be extended to include such operating conditions as well.

There has been a great deal of research towards development of models for unbalanced operating conditions of LCC-HVDC systems. However, virtually all the existing models are excessively complicated, which may adversely affect their core utility of enhanced computational complexity. Additionally, existing models often require specialized knowledge in order to represent imbalances. For example, the user may need to evoke a certain model with specific a-priori knowledge about the fault, e.g., the amount of negative- and zero-sequence components it introduces, in order to simulate such a fault [4]. This is a major limitation as it makes existing models unable to respond and self-adjust automatically based upon the conditions in the circuits surrounding the converter as conventional EMT models so.

In this section a DP-based model of a six-pulse thyristor bridge is developed. This model is able to represent the converter for system imbalances and merely requires AC voltage measurements in order to detect the imbalance type to adjust its parameters. Development of this model is firstly explained in the context of a simple single-phase fault, and is then extended to arbitrary faults types.

Consider a single-phase-to-ground fault in which the phase-a voltage is reduced in half as follows.

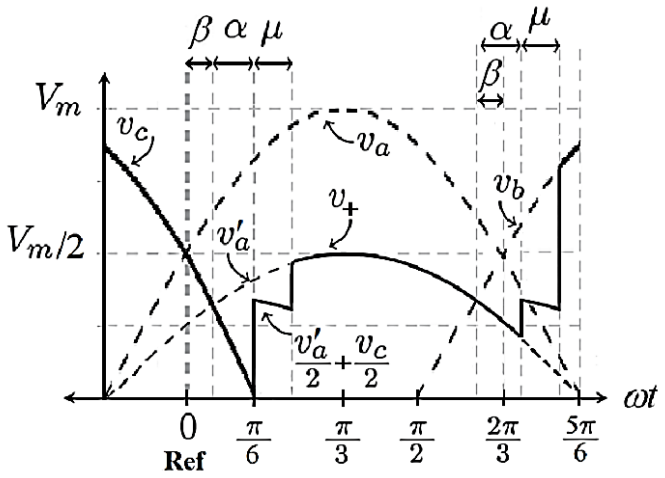

Figure 4-5 AC voltages under single-phase-to-ground fault

The reduction of the phase-a voltage will change the zero-crossing of the line voltage denoted as β in Figure 4-5. This new term facilitates introducing general switching functions for various operating conditions under any fault type. During balanced conditions, this term will be equal to zero. Following AC voltages will be applied on system during single-phase-to-ground fault at phase *a*.

$$\begin{cases} v_a &= V_m/2\sin(\omega t+\pi/6) \\ v_b &= V_m\sin(\omega t-\pi/2) \\ v_c &= V_m\sin(\omega t+5\pi/6) \end{cases} \tag{4-19}$$

One can show that such operating condition would result in following asymmetrical voltage switching functions. As it can be seen, overlap angles are not equal anymore and they will have a specific value for each phase.

$$Sv_{ab}(\theta)=\begin{cases}1/2 & \beta+\alpha\le\theta<\beta+\alpha+\mu_{ca}\\ & \pi/3+\alpha\le\theta<\pi/3+\alpha+\mu_{bc}\\ 1 & \beta+\alpha+\mu_{ca}\le\theta<\pi/3+\alpha\\ -1/2 & \pi+\beta+\alpha\le\theta<\pi+\beta+\alpha+\mu_{ca}\\ & 4\pi/3+\alpha\le\theta<4\pi/3+\alpha+\mu_{bc}\\ -1 & \pi+\beta+\alpha+\mu_{ca}\le\theta<4\pi/3+\alpha\\ 0 & \text{otherwise}\end{cases} \tag{4-20}$$

$$Sv_{bc}(\theta)=\begin{cases}-1 & 0\le\theta<\beta+\alpha\\ & 5\pi/3-\beta+\alpha+\mu_{ab}\le\theta<2\pi\\ -1/2 & \beta+\alpha\le\theta<\beta+\alpha+\mu_{ca}\\ & 5\pi/3-\beta+\alpha\le\theta<5\pi/3-\beta+\alpha+\mu_{ab}\\ 1/2 & 2\pi/3-\beta+\alpha\le\theta<2\pi/3-\beta+\alpha+\mu_{ab}\\ & \pi+\beta+\alpha\le\theta<\pi+\beta+\alpha+\mu_{ca}\\ 1 & 2\pi/3-\beta+\alpha+\mu_{ab}\le\theta<\pi+\beta+\alpha\\ 0 & \text{otherwise}\end{cases} \tag{4-21}$$

$$Sv_{ca}(\theta)=\begin{cases}-1/2 & \pi/3+\alpha\le\theta<\pi/3+\alpha+\mu_{bc}\\ & 2\pi/3-\beta+\alpha\le\theta<2\pi/3-\beta+\alpha+\mu_{ab}\\ -1 & \pi/3+\alpha+\mu_{bc}\le\theta<2\pi/3-\beta+\alpha\\ 1/2 & 4\pi/3+\alpha\le\theta<4\pi/3+\alpha+\mu_{bc}\\ & 5\pi/3-\beta+\alpha\le\theta<5\pi/3-\beta+\alpha+\mu_{ab}\\ 1 & 4\pi/3+\alpha+\mu_{bc}\le\theta<5\pi/3-\beta+\alpha\\ 0 & \text{otherwise}\end{cases} \tag{4-22}$$

where the overlap angles would be as follows.

$$\mu_{ca}=\cos^{-1}(\cos(\alpha+\beta+\pi/6-0.7137)-\frac{2\sqrt{3}}{\sqrt{7}}\frac{2X_S I_d}{\sqrt{3}Vm})-(\alpha+\beta+\pi/6-0.7137) \tag{4-23}$$

$$\mu_{bc} = \cos^{-1}(\cos(\alpha) - \frac{2X_S I_d}{\sqrt{3}Vm}) - \alpha \tag{4-24}$$

$$\mu_{ab} = \cos^{-1}(\cos(\alpha - \beta + \pi/6 - 0.3335) - \frac{2\sqrt{3}}{\sqrt{7}}\frac{2X_S I_d}{\sqrt{3}Vm}) - (\alpha - \beta + \pi/6 - 0.3335) \tag{4-25}$$

Deriving current switching functions under such an unbalanced condition as in Figure 4-5 is also straightforward as shown below. The following terms ϕ_a, ϕ_b, ϕ_c, A, B, and C are defined to facilitate current switching functions representation.

$$\phi_a \equiv \alpha + \beta + \pi/6 - 0.7137 \tag{4-26}$$

$$\phi_b \equiv \alpha - \beta + \pi/6 - 0.3335 \tag{4-27}$$

$$\phi_c \equiv \alpha \tag{4-28}$$

$$A \equiv 1/(\cos(\phi_a) - \cos(\phi_a + \mu_{ca})) \tag{4-29}$$

$$B \equiv 1/(\cos(\phi_b) - \cos(\phi_b + \mu_{ab})) \tag{4-30}$$

$$C \equiv 1/(\cos(\phi_c) - \cos(\phi_c + \mu_{bc})) \tag{4-31}$$

Based on defined parameters and Figure 4-5, one can prove equation (4-32) as current switching function during a single-phase-to-ground fault at phase *a*. The other two current switching functions $Si_b(\theta)$ and $Si_c(\theta)$ can be calculated in the same manner as follows.

$$Si_a(\theta)=\begin{cases} A(\cos(\phi_a)-\cos(\frac{\pi}{6}-0.7+\theta)) & \beta+\alpha\le\theta<\beta+\alpha+\mu_{ca} \\ 1 & \beta+\alpha+\mu_{ca}\le\theta<\frac{2\pi}{3}-\beta+\alpha \\ B(\cos(\frac{\pi}{6}-0.3+\theta-\frac{2\pi}{3})-\cos(\phi_b+\mu_{ab})) & \frac{2\pi}{3}-\beta+\alpha\le\theta<\frac{2\pi}{3}-\beta+\alpha+\mu_{ab} \\ A(\cos(\frac{\pi}{6}-0.7+\theta-\pi)-\cos(\phi_a)) & \pi+\beta+\alpha\le\theta<\pi+\beta+\alpha+\mu_{ca} \\ -1 & \pi+\beta+\alpha+\mu_{ca}\le\theta<\frac{5\pi}{3}-\beta+\alpha \\ B(\cos(\phi_b+\mu_{ab})-\cos(\frac{\pi}{6}-0.3+\theta-\frac{5\pi}{3})) & \frac{5\pi}{3}-\beta+\alpha\le\theta<\frac{5\pi}{3}-\beta+\alpha+\mu_{ab} \\ 0 & \text{otherwise} \end{cases} \tag{4-32}$$

$$Si_b(\theta)=\begin{cases} -1 & 0\le\theta<\frac{\pi}{3}+\alpha\ \&\ \frac{5\pi}{3}-\beta+\alpha+\mu_{ab}\le\theta<2\pi \\ C(\cos(\phi_c+\mu_{bc})-\cos(\theta-\frac{\pi}{3})) & \frac{\pi}{3}+\alpha\le\theta<\frac{\pi}{3}+\alpha+\mu_{bc} \\ B(\cos(\phi_b)-\cos(\phi_b+\theta-\frac{2\pi}{3})) & \frac{2\pi}{3}-\beta+\alpha\le\theta<\frac{2\pi}{3}-\beta+\alpha+\mu_{ab} \\ 1 & \frac{2\pi}{3}-\beta+\alpha+\mu_{ab}\le\theta<\frac{4\pi}{3}+\alpha \\ C(\cos(\theta-\frac{4\pi}{3})-\cos(\phi_c+\mu_{bc})) & \frac{4\pi}{3}+\alpha\le\theta<\frac{4\pi}{3}+\alpha+\mu_{bc} \\ B(\cos(\frac{\pi}{6}-0.3+\theta-\frac{5\pi}{3})-\cos(\phi_b)) & \frac{5\pi}{3}-\beta+\alpha\le\theta<\frac{5\pi}{3}-\beta+\alpha+\mu_{ab} \\ 0 & \text{otherwise} \end{cases} \tag{4-33}$$

$$Si_c(\theta)=\begin{cases} 1 & 0\le\theta<\beta+\alpha \;\&\; \frac{4\pi}{3}+\alpha+\mu_{bc}\le\theta<2\pi \\ A(\cos(\frac{\pi}{6}-0.7+\theta)-\cos(\phi_a+\mu_{ca})) & \beta+\alpha\le\theta<\beta+\alpha+\mu_{ca} \\ C(\cos(\theta-\frac{\pi}{3})-\cos(\phi_c)) & \frac{\pi}{3}+\alpha\le\theta<\frac{\pi}{3}+\alpha+\mu_{bc} \\ -1 & \frac{\pi}{3}+\alpha+\mu_{bc}\le\theta<\pi+\beta+\alpha \\ A(\cos(\phi_a+\mu_{ca})-\cos(\frac{\pi}{6}-0.7+\theta-\pi)) & \pi+\beta+\alpha\le\theta<\pi+\beta+\alpha+\mu_{ca} \\ C(\cos(\phi_c)-\cos(\theta-\frac{4\pi}{3})) & \frac{4\pi}{3}+\alpha\le\theta<\frac{4\pi}{3}+\alpha+\mu_{bc} \\ 0 & \text{otherwise} \end{cases} \tag{4-34}$$

With these time domain expression for all voltage and current switching functions, the dynamic phasor extractor may be applied next to obtain their dynamic phasor equivalents.

$$\langle Sv_{ab}(\theta)\rangle_k=\begin{cases} 0 & for \quad k=even \\ \frac{e^{-jk\alpha}}{jk2\pi}\left[e^{-jk\beta}(1+e^{-jk\mu_{ca}})-e^{-jk\pi/3}(1+e^{-jk\mu_{bc}})\right] & for \quad k=odd \end{cases} \tag{4-35}$$

$$\langle Sv_{bc}(\theta)\rangle_k=\begin{cases} 0 & for \quad k=even \\ \frac{e^{-jk\alpha}}{jk2\pi}\left[e^{-jk\beta}(1+e^{-jk\mu_{ca}})-e^{-jk(2\pi/3-\beta)}(1+e^{-jk\mu_{ab}})\right] & for \quad k=odd \end{cases} \tag{4-36}$$

$$\langle Sv_{ca}(\theta)\rangle_k=\begin{cases} 0 & for \quad k=even \\ \frac{e^{-jk\alpha}}{jk2\pi}\left[e^{-jk(2\pi/3-\beta)}(1+e^{-jk\mu_{ab}})-e^{-jk\pi/3}(1+e^{-jk\mu_{bc}})\right] & for \quad k=odd \end{cases} \tag{4-37}$$

For current switching functions, fundamental component should be calculated separately as follows, since a zero by zero division happens at $k = 1$.

$$\begin{aligned}\langle Si_a(\theta)\rangle_{k=1} &= \frac{e^{-j\alpha}}{-j2\pi}\Big[\\ &\Big((2A\cos\phi_a - 2 - A\cos(\phi_a+\mu_{ca}))e^{-j\mu_{ca}} + j\mu_{ca}e^{j\phi_a} + jA\sin\phi_a\Big)e^{-j\beta} + \\ &(2+2B\cos(\phi_b+\mu_{ab}) - B\cos\phi_b - Be^{j\phi_b} + jB\sin(\phi_b+\mu_{ab})e^{-j\mu_{ab}} - j\mu_{ab}e^{j\phi_b})e^{-j(\frac{2\pi}{3}-\beta)}\ \Big]\end{aligned} \tag{4-38}$$

$$\begin{aligned}\langle Si_b(\theta)\rangle_{k=1} &= \frac{e^{-j\alpha}}{-j2\pi}\Big[\\ &\Big(-2/C + 2\cos\phi_c + j\sin\phi_c - 2\cos(\phi_c+\mu_{bc}) - j\sin(\phi_c+\mu_{bc})e^{-j\mu_{bc}} + j\mu_{bc}e^{j\phi_c}\Big)Ce^{-j\frac{\pi}{3}} + \\ &((-2/B + 2\cos\phi_b - 2\cos(\phi_b+\mu_{ab}) + j\sin(\phi_b+\mu_{ab}) + j\mu_{ab}e^{j(\phi_b+\mu_{ab})})e^{-j\mu_{ab}} + j\sin\phi_b)Be^{-j(\frac{2\pi}{3}-\beta)}\ \Big]\end{aligned} \tag{4-39}$$

$$\begin{aligned}\langle Si_c(\theta)\rangle_{k=1} &= \frac{e^{-j\alpha}}{-j2\pi}\Big[\\ &\Big((2/C - 2\cos\phi_c + 2\cos(\phi_c+\mu_{bc}) + j\sin(\phi_c+\mu_{bc}))e^{-j\mu_{bc}} - j\mu_{bc}e^{j\phi_c} - j\sin\phi_c\Big)Ce^{-j\frac{\pi}{3}} + \\ &(2/A - 2\cos\phi_a + 2\cos(\phi_a+\mu_{ca}) - j\sin\phi_a - j\mu_{ca}e^{j\phi_a} + j\sin(\phi_a+\mu_{ca})e^{-j\mu_{ca}})Ae^{-j\beta}\ \Big]\end{aligned} \tag{4-40}$$

It can be shown that all even components of current switching functions will be equal to zero. The rest of the components will be as follows.

$$\begin{aligned}\langle Si_a(\theta)\rangle_k &= \frac{e^{-j\alpha}}{j\pi k(1-k^2)}\Big[\ -(1-k^2)e^{-jk(\frac{2\pi}{3}-\beta)} + (1-k^2)e^{-jk(\beta+\mu_{ca})} + \\ &A(-(1-k^2)\cos\phi_a - k^2\cos(\phi_a+\mu_{ca}) - jk\sin(\phi_a+\mu_{ca}))e^{-jk(\beta+\mu_{ca})} + \\ &A(\cos\phi_a + jk\sin\phi_a)e^{-jk\beta} + B(\cos(\phi_b+\mu_{ab}) + jk\sin(\phi_b+\mu_{ab}))e^{-jk(\frac{2\pi}{3}-\beta+\mu_{ab})} + \\ &B(-(1-k^2)\cos(\phi_b+\mu_{ab}) - k^2\cos\phi_b - jk\sin\phi_b)e^{-jk(\frac{2\pi}{3}-\beta)}\ \Big]\end{aligned} \tag{4-41}$$

$$\begin{aligned}\left\langle Si_b(\theta)\right\rangle_k = \frac{e^{-j\alpha}}{j\pi k(1-k^2)}\Big[\ & (1-k^2)e^{-jk\frac{\pi}{3}} + (1-k^2)e^{-jk(\frac{2\pi}{3}-\beta+\mu_{ab})} + \\ & C((1-k^2)\cos(\phi_c+\mu_{bc}) + k^2\cos\phi_c + jk\sin\phi_c)e^{-jk\frac{\pi}{3}} + \\ & C(-\cos(\phi_c+\mu_{bc}) - jk\sin(\phi_c+\mu_{bc}))e^{-jk(\frac{\pi}{3}-\mu_{bc})} + B(\cos\phi_b + jk\sin\phi_b)e^{-jk(\frac{2\pi}{3}-\beta)} \\ & B(-(1-k^2)\cos\phi_b - k^2\cos(\phi_b+\mu_{ab}) - jk\sin(\phi_b+\mu_{ab}))e^{-jk(\frac{2\pi}{3}-\beta+\mu_{ab})}\ \Big]\end{aligned} \tag{4-42}$$

$$\begin{aligned}\left\langle Si_c(\theta)\right\rangle_k = \frac{e^{-j\alpha}}{j\pi k(1-k^2)}\Big[\ & -(1-k^2)e^{-jk\beta} - (1-k^2)e^{-jk(\frac{\pi}{3}+\mu_{bc})} + \\ & A(-(1-k^2)\cos(\phi_a+\mu_{ca}) - k^2\cos\phi_a - jk\sin\phi_a)e^{-jk\beta} + \\ & A(\cos(\phi_a+\mu_{ca}) + jk\sin(\phi_a+\mu_{ca}))e^{-jk(\beta+\mu_{ca})} + C(-\cos\phi_c - jk\sin\phi_c)e^{-jk\frac{\pi}{3}} + \\ & C((1-k^2)\cos\phi_c + k^2\cos(\phi_c+\mu_{bc}) + jk\sin(\phi_c+\mu_{bc}))e^{-jk(\frac{\pi}{3}+\mu_{bc})}\ \Big]\end{aligned} \tag{4-43}$$

The switching functions for unbalanced operating conditions are clearly asymmetrical and their shapes depend on the type and level of the asymmetrical fault. In order to create such switching functions for arbitrary faults, one needs to measure the terminal voltages and phase angles (using three independent phase-locked loops) and then solve equations similar to the ones in (4-26)-(4-31) to obtain ϕ_a, ϕ_b, ϕ_c, A, B, and C for a specific fault. Although asymmetrical switching functions, such as those obtained above, are able to represent the converter's operation with great accuracy, their asymmetrical shape and more importantly their dependence on nonlinear equations to solve for their parameters make their usage cumbersome and inconvenient. As such the following section introduces an approximation (relaxation) of these asymmetrical switching functions that yields symmetry and simplifies the form of the voltage and current switching functions in exchange for an insignificant amount of inaccuracy. Figure 4-6 depicts a simple circuit for comparing the DP models based upon both the asymmetrical and the relaxed

symmetrical switching functions. The circuit consists of an AC system connected to a six-pulse bridge rectifier through a Y/Y transformer. A resistive phase-to-ground fault on phase-a is applied. To isolate the dynamics of the system's response, the firing angle (α = 30º) is maintained constant.

A single-phase-to-ground fault with a resistance of 0.01 Ωwill cause 50% voltage drop in phase-a according to source resistance. However, the performance of the developed model of LCC is not depended on the quality of the AC system waveform. As such, one can decrease the fault resistance to zero and make the AC voltage to drop to zero and still expect the same performance from the DP-based model of LCC.

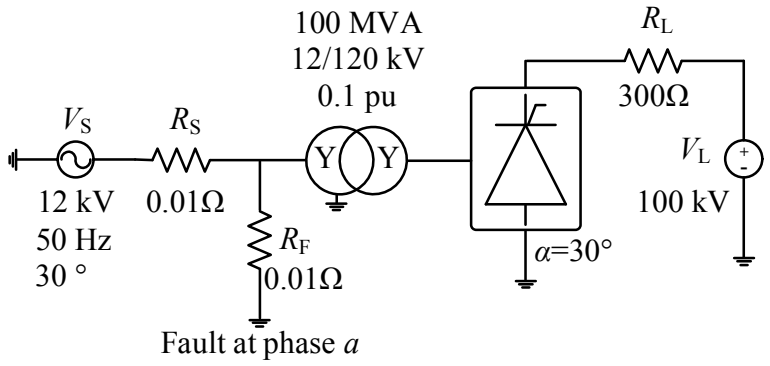

Figure 4-6 Simple case study for comparing asymmetrical and relaxed DP models of LCC-HVDC system

DC voltage and current waveforms in Figure 4-7 are obtained from a purely EMT model; these traces clearly show how the symmetrical and balanced operation of the converter prior to the fault at t = 1 s is disturbed as a result of the asymmetrical fault.

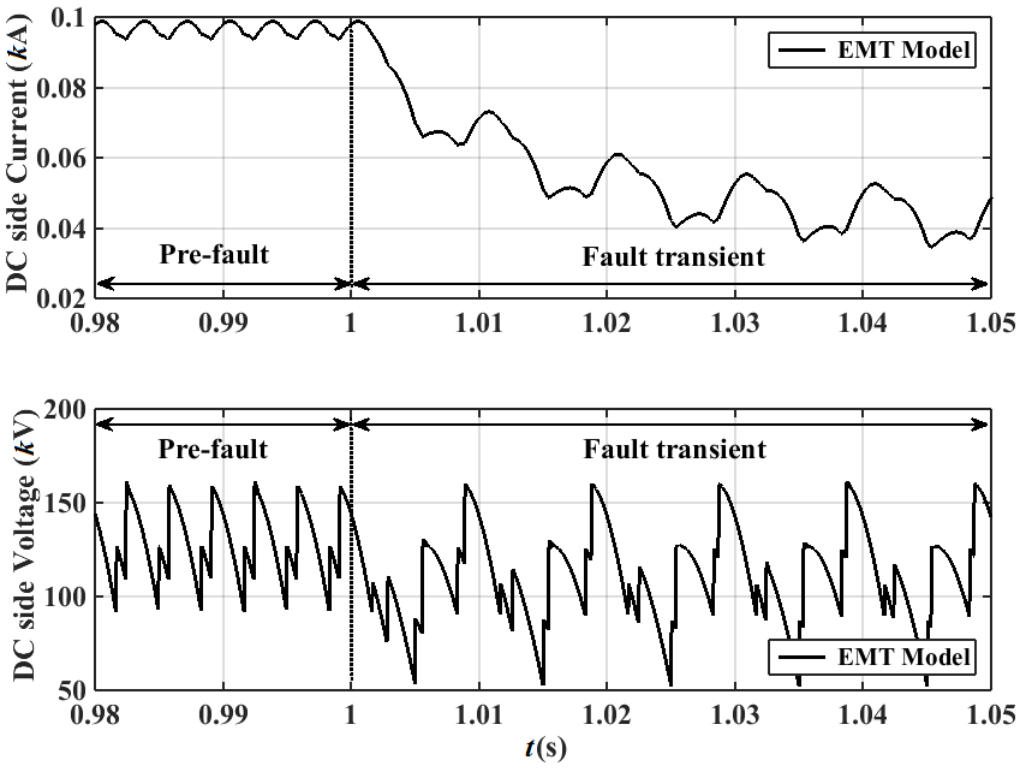

Figure 4-7 DC Current and voltage for pre- and post-fault conditions

Figure 4-8 shows the overlaps angles of the converter. Prior to t = 1 s the overlap angles are all equal as the converter operates symmetrically. They are, however, different when the fault occurs. Figure 4-8 also illustrates the relaxed overlap angles (using (4-24) and (4-44)), which is used to generate the relaxed and symmetrical switching functions.

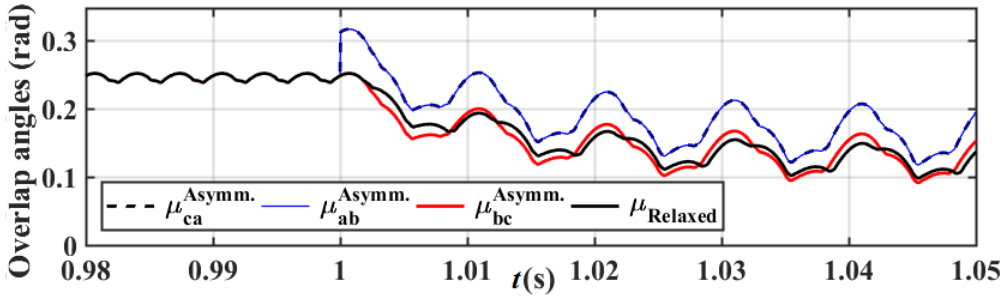

Figure 4-8 Overlap angles for pre- and post-fault conditions

In order to achieve a set of symmetrical switching functions, relaxations are introduced in the underlying conditions for their derivation. Specifically, the overlap angles (see (4-23)-(4-25)) are assumed to follow the form in (4-10); the term V_{m} in (4-10) is, however, replaced based on the rms value of the line-to-line voltage of the two phases whose voltage difference does not change before and after the fault. Furthermore, the phase angle of such a voltage is used to determine the starting point of the symmetrical switching functions. Hereinafter, these symmetrical switching functions are referred to as relaxed switching functions to denote the relaxation (approximation) that is used to derive them. For example, for a single phase-to-ground fault at phase a, or a two-phase-to-ground fault at phases b and c, one needs to use μ_{bc} and V_{bc} for generating symmetrical switching functions based on the following formula for V_{m}.

$$V_{\mathrm{m}} = \mathrm{rms}(v_{\mathrm{b}} - v_{\mathrm{c}})\sqrt{2} \tag{4-44}$$

To generate the rms value of line-to-line voltages as well as the phase angle for shifting the switching functions, a dynamic phasor-based phase-locked loop (PLL) is implemented based upon the fundamental-component extraction method given in [59].

Figure 4-9 shows the pre- and post-fault switching functions of phase-*b* voltage and current, which clearly depicts the difference between asymmetrical and symmetrical ones.

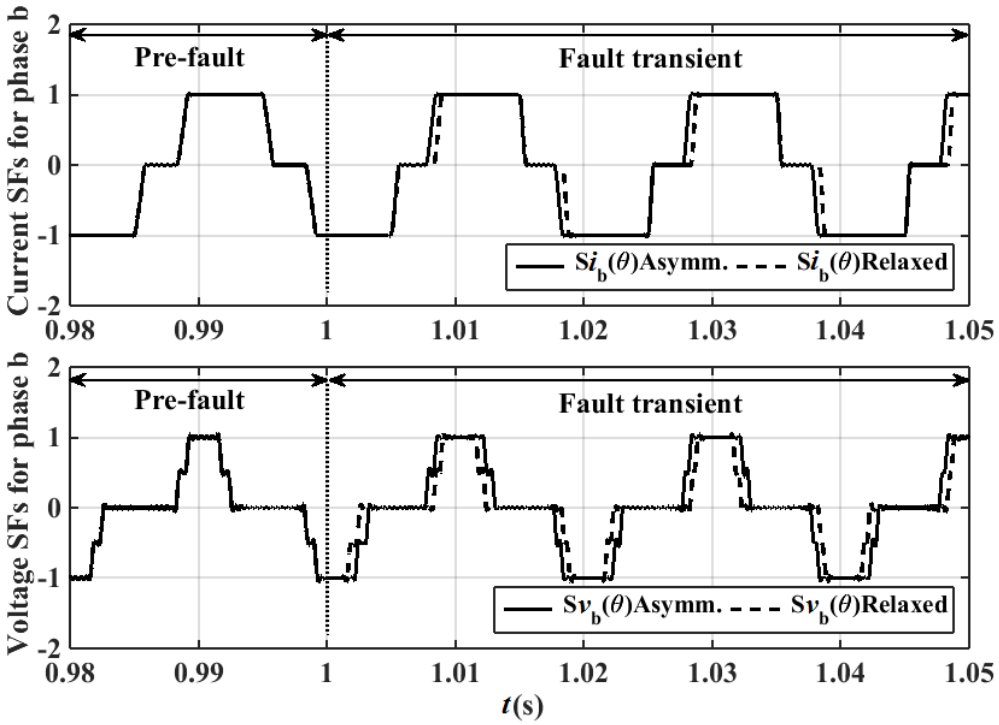

Figure 4-9 Phase-b current and voltage SFs for pre- and post-fault conditions

By measuring only the line-to-line voltages, the parameters for the above symmetrical relaxed switching functions are derived. These relaxed switching functions have the capability of working under any operating condition. Therefore, not only do these relaxed symmetrical switching functions are able to represent various balanced and unbalanced operating conditions, but also self-adjust their parameters using only AC terminal voltage measurements. The method presented in [4] is used to guarantee the performance of the proposed model during commutation failure.

Figures 4-10 and 4-11 show the original (asymmetrical) and the new relaxed (symmetrical) voltage and current switching functions by combining the first five sets of dominant harmonic components (i.e., fundamental, and $6n\pm1$ for n = 1,…, 4). The same number of sequential harmonics (i.e., fundamental, 5, 7, 11, 13, 17, 19, 23, 25) is used in

the following chapters as well. To highlight the variations in switching functions the time interval [1,1.02] s is not included.

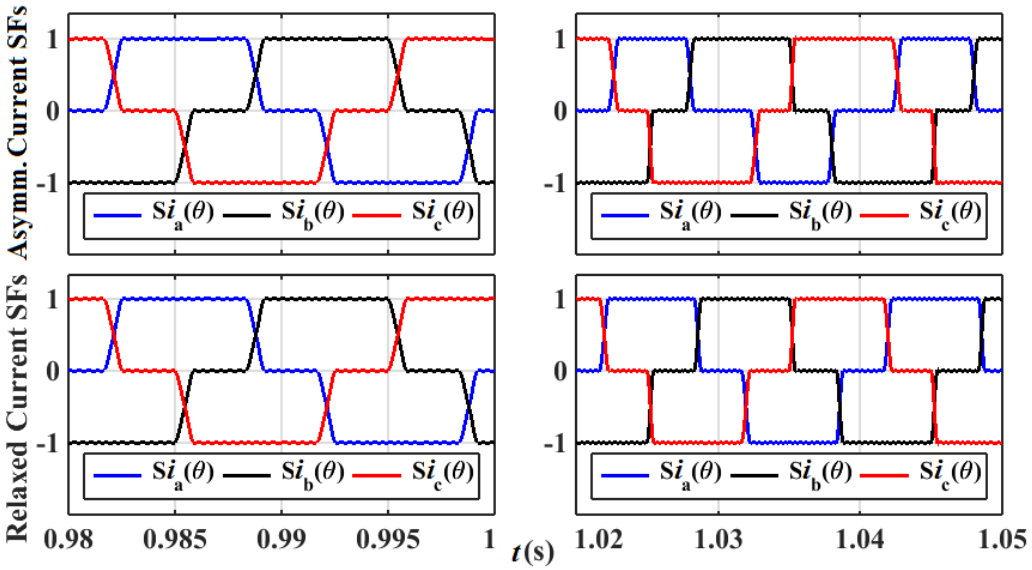

Figure 4-10 Current switching functions for asymmetrical and relaxed models

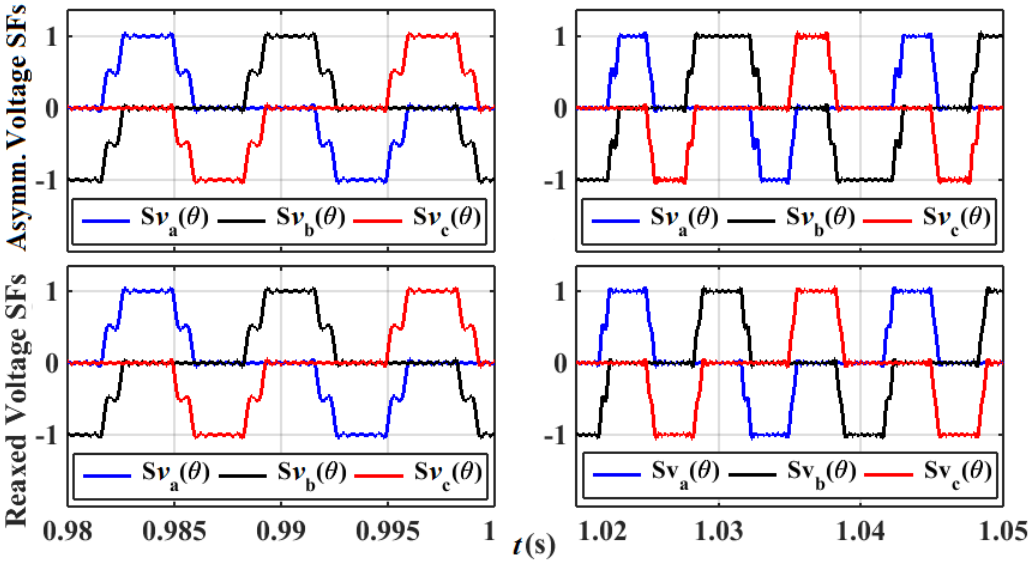

Figure 4-11 Voltage switching functions for asymmetrical and relaxed models

It must be noted that before the onset of the fault there is no difference between the two sets of switching functions, as both models represent balanced operation. The

difference only appears during the fault, which in the presented example is applied at t = 1 s and lasts 0.12 s. Using both sets of switching functions, dynamic phasor models of the converter system in Figure 4-6 are implemented in PSCAD/EMTDC simulator.

According to Figure 4-12, both DP-based models match the detailed EMT results before and after the fault when the converter operates under balanced conditions. During the fault, the original asymmetrical switching functions produce matching results with the detailed EMT model; the model with relaxed (symmetrical) switching functions, however, is slightly different due to its relaxed (approximate) nature. As the number of harmonics used to develop the relaxed response increases, a more accurate response becomes achievable at the expense of a lower computational gain.

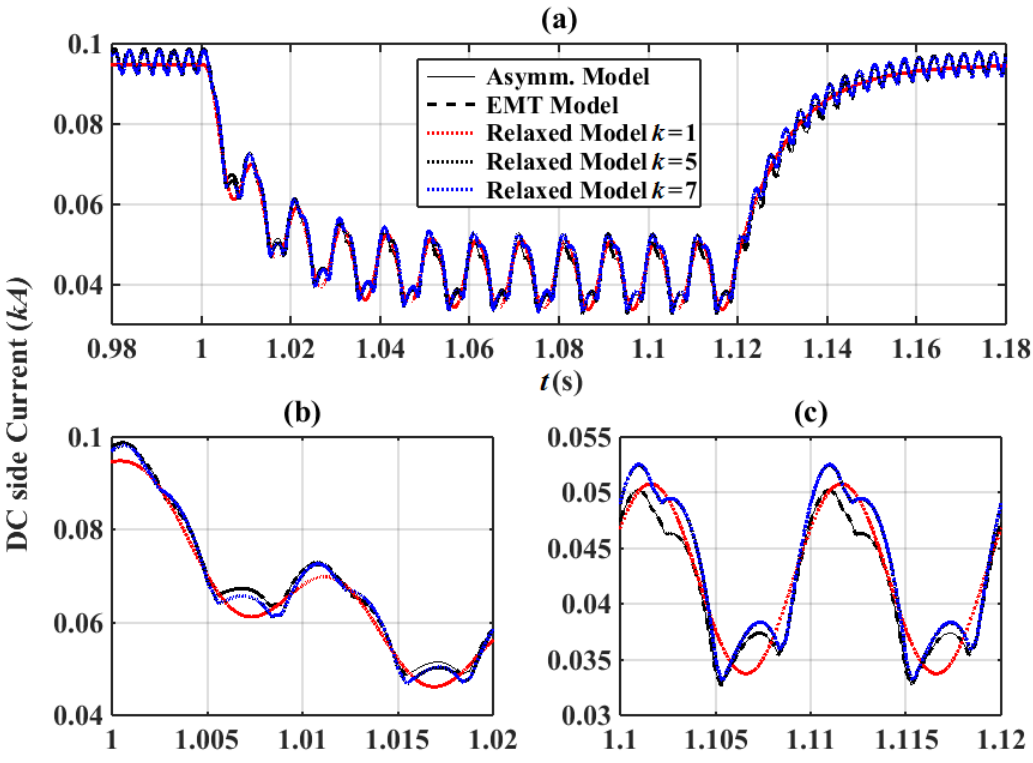

Figure 4-12 DC current for (a) fault, (b) fault transients, and (c) fault steady state of A-G fault

According to Figure 4-12, there is a small difference between the results of including 5 and 7 harmonics. Various fault types with different severity based on the fault impedance have been applied to ensure the validity of the proposed relaxed model.

Table 4-1 Computational time comparison

Model Type	*CPU Time (sec)*	*Time gain*
EMT	5.58	N/A
Asymm. DP	4.32	5.58/4.32=1.3
Relaxed DP (k = 1)	1.66	5.58/1.66=3.4
Relaxed DP (k = 5)	2.16	5.58/2.16=2.6
Relaxed DP (k = 7)	2.57	5.58/2.57=2.2

The proposed relaxed model benefits from simple symmetrical switching functions with an acceptable accuracy during system transients and computational time gain as shown in Table 4-1. Three different harmonic sets are considered for the relaxed DP-based models; these include a model with only the fundamental component (k = 1), a model with the first five sets of harmonics (k = 5, i.e., harmonics 1, 5, 7, 11, 13, 17, 19, 23, 25), and one with the first seven sets of harmonics (k = 7, i.e. harmonics 1, 5, 7, 11, 13, 17, 19, 23, 25, 29, 31). The developed models are run in PSCAD/EMTDC on a Corei7 2.67 GHz Intel® Xeon® CPU with 12 GB of RAM and a 64-bit operating system. To measure the CPU time, runtime messages of PSCAD/EMTDC are used and the reported values are confirmed against the ones achieved from a custom component developed for the same purposes. The measurements are for a 2-s simulation of network in Figure 4-6. According to Table 4-1, both DP-based models outperform the EMT model in terms of required CPU time to complete the same simulation, even though all models

use the same simulation time-step. The savings are due to the fact that converter switches and electrical nodes associated with them are replaced with mathematical switching functions. This has implications on the size of the admittance matrix of the network and its inversion during switching events. Additionally, elimination of switches removes the need for time-consuming interpolation calculations that are commonly used in EMT simulators to improve the accuracy of switching instants. It is while the present dynamic phasor based models with the capability of working under unbalanced conditions use two sets of switching functions. Such sets of functions are for balanced and unbalanced operating conditions and usually they include *abc* to *dq*0 transformation, which makes their processing time consuming.

Table 4-2 Normalized error in DC current for pre-, post-, and during fault transients including different harmonics (k=1,5,7)

Model Type	*Pre-flt. (%)*	*Flt. Transient (%)*	*Post-flt. (%)*
EMT	-	-	-
Asymm. DP	0.01	0.01	0.01
Relaxed DP ($k = 1$)	4.1	11.56	4.17
Relaxed DP ($k = 5$)	0.58	0.42	1.18
Relaxed DP ($k = 7$)	0.57	0.40	1.17

The normalized error between the detailed EMT and the DP-based model with relaxed switching functions during fault is merely 5%, which is negligible in most system-level studies as shown in Table 4-2. According to the reported errors resulting from various number of harmonics, considering a single harmonic for building the switching functions does not result in an acceptable level of accuracy. It is while there is

a negligible difference between inclusion of the first five ($k = 5$) or the first seven ($k = 7$) sets of sequential harmonics.

4.4 Simulation Results for Large Electric Networks

To assess the performance of the proposed relaxed dynamic phasor model, CIGRE HVDC benchmark [39] and IEEE 12-bus [42] systems have been considered as large electric networks with high number of nodes. These two case studies have been implemented in PSCAD-EMTDC software based on both DP modeling approach for HVDC valves and the prepared blocks in PSCAD library. Results from dynamic phasor model in PSCAD have been validated against the ones from the software library.

4.4.1 CIGRE HVDC benchmark system

A single-line diagram of the 12-pulse mono-polar LCC-HVDC system based on CIGRE HVDC benchmark is presented in Figure 4-13. It must be mentioned that the whole system has also been redesigned for 60 Hz applications but only results for 50 Hz system have been presented. Furthermore, only the valve part which includes fast switching transients has been modeled based on proposed relaxed dynamic phasor method and the rest of the system is in time domain. A DP interface has been employed for connecting these two types of model, which both run with the same simulation time-step. All other system parameters are presented in Table 4-3.

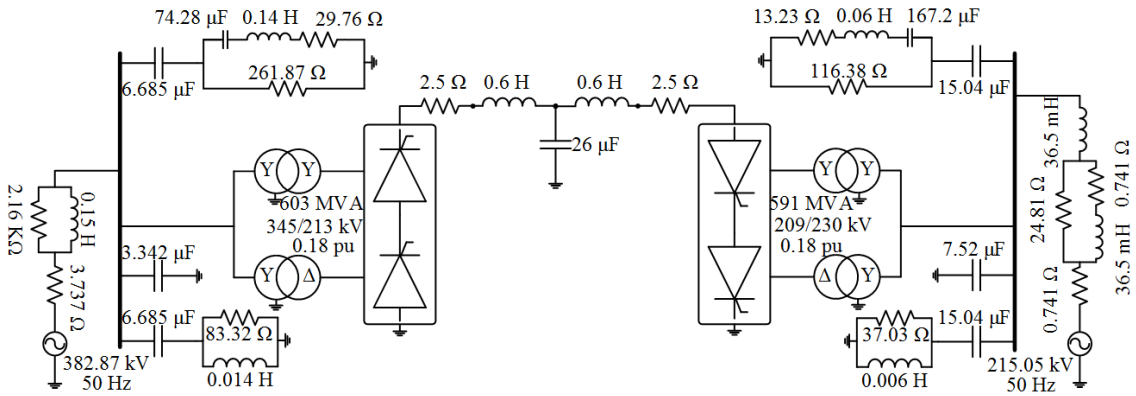

Figure 4-13 CIGRE Benchmark Model at 50 Hz

Table 4-3 CIGRE HVDC benchmark system data

Model Type	*Rectifier*	*Inverter*
AC voltage	345 kV	230 kV
Nominal DC voltage	500 kV	500 kV
Nominal DC current	2 kA	2 kA
Base MVA	1000 MVA	1000 MVA
Filter VAr supply	625 MVAr	625 MVAr
Nominal angle	α=15º	γ=15º

The SCR at the point of common coupling (PCC) for both rectifying and inverting sides is equal to 2.5. This means that the AC system is a weak one and more overvoltage would occur during load rejection in comparison with a strong network.

Getting familiar with CIGRE subsystems, it is time to investigate system performance. For this purpose, a two-phase-to-ground fault at phases b and c (AB-G) has been applied (with fault resistance 0.37 Ω) on inverting side at t = 3 s lasting for 0.12s.

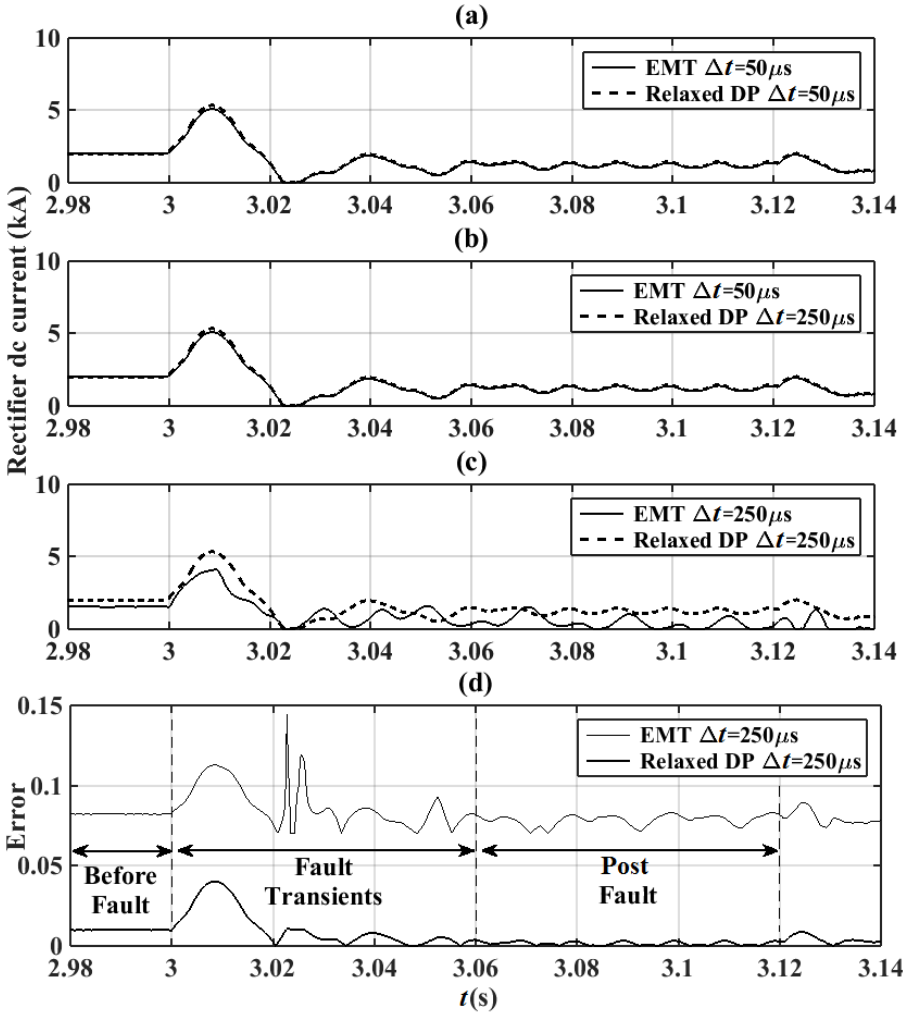

Figure 4-14 DC current for AB-G fault (a) 50 μs for both models, (b) different time-steps, and (c) 250 μs time-step for both models, and (d) the resulting error

Close conformity between EMT and DP-based simulation results is observed when both models are run with a 50-μs time-step. When the simulation time-step is increased to 250 μs, the relaxed DP-based model remains its acceptable accuracy (closely matching the EMT results with a 50-μs time-step) while the EMT model with 250-μs time-step shows significant inaccuracy. This is an additional benefit of the proposed DP-based model, which illustrates greater accuracy at time-steps for which conventional EMT

solutions lose accuracy. Such property enables use of larger simulation time-steps, which in turn further expedite large system simulations.

The computational benefits of using relaxed model are summarized in Table 4-4, which shows CPU time gains of over 700% when larger time-steps are used without significant loss of accuracy as shown in Table 4-5. The maximum accuracy loss for the relaxed DP model happens during fault transients and is around 4%.

Table 4-4 Computational time comparison for various time-steps in CIGRE benchmark model

Model Type	*CPU Time (sec)*	*CPU Time gain*
EMT 50 μs	9.36	N/A
Relaxed 50 μs	3.02	9.36/3.02=3.1
Relaxed 250 μs	1.285	9.36/1.285=7.3

Table 4-5 Normalized error in DC current for pre-fault, fault transients, and post-fault intervals

Model Type	*Pre-fault (%)*	*Fault transients (%)*	*Post-fault (%)*
EMT 50 μs	N/A	N/A	N/A
EMT 250 μs	8.23	14.43	8.31
Relaxed 50 μs	0.73	1.39	0.07
Relaxed 250 μs	0.99	4.03	0.32

4.4.2 IEEE 12-bus system

Figure 4-15 depicts single-line diagram for the IEEE 12-bus system with generators, lines, loads, and transformers parameters as presented in [42]. This system is a large electric network with electromechanical transients and need for a big simulation time-

step in order of $m$sec. Therefore, with the presence of power electronic devices in such system, EMTDC models may not be able to show an acceptable level of accuracy.

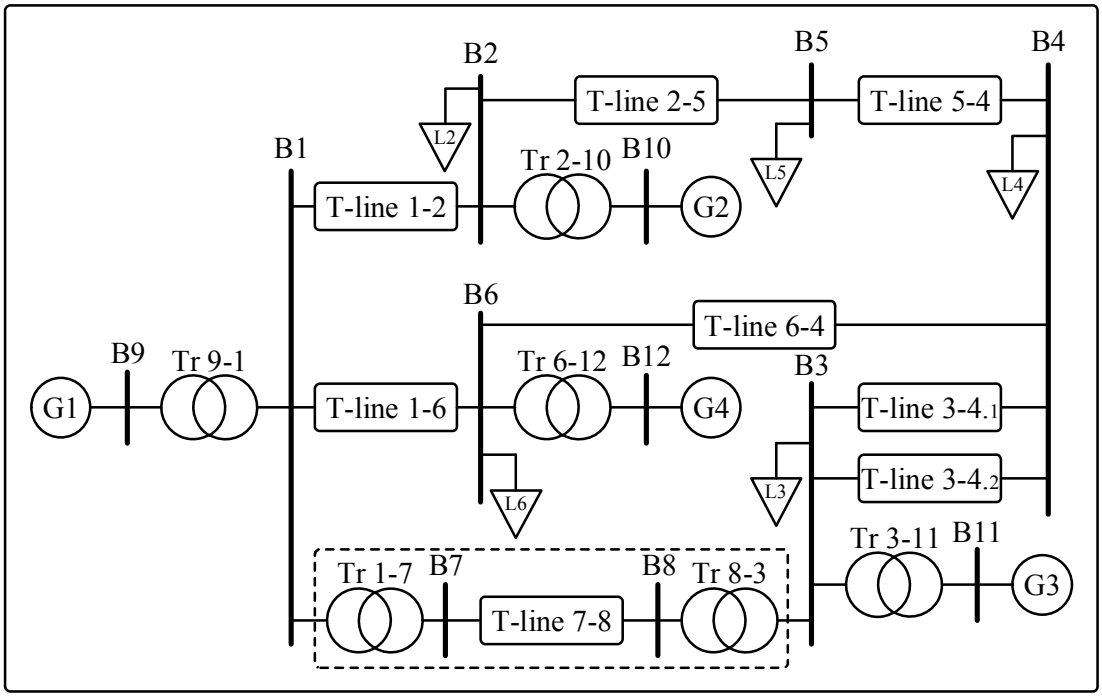

Figure 4-15 IEEE 12-bus system

To assess the performance of the proposed relaxed DP model for LCC-HVDC, transmission line between buses 7 and 8 and its transformers have been replaced with a 12-pulse mono-polar HVDC system as depicted in Figure 4-16. DC line parameters are derived from Bipole II HVDC transmission line. Bipole II operates at ±500kV with line parameters L = 939 mH, R = 14.7 Ω, and C = 5.51 μF for a π model which are evenly distributed over approximately 980km DC line. These parameters are being scaled for a 600 km DC line replacing the AC line connecting bus numbers 7 and 8.

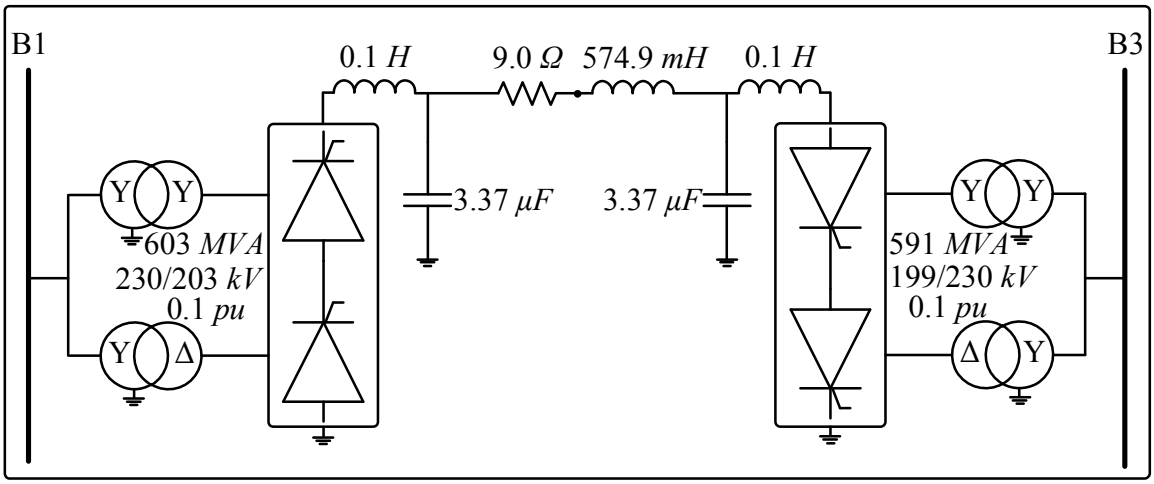

Figure 4-16 LCC-HVDC system replacing transmission line T-Line 7-8

Now based on this new system configuration and using Power Transmission System Planning Software (PSS/E), a power flow analysis would be conducted to reach the new system settings for generators. Based on this new operating condition, the whole system will be simulated in PSCAD using EMTDC and relaxed DP models for the valve groups. To investigate system performance during transients, a three-phase-to-ground fault has been applied at bus number4. Furthermore, to show the advantage of DP model over EMTDC one, a large simulation time step has been employed as well as a small one.

According to Figure 4-17 the relaxed DP-based model with both 50-μs and 250-μs time-steps closely matches the EMT results with a 50-μs time-step. It is also notable as the DP-based model maintains accuracy even at a large simulation time-step while the EMT model's accuracy deteriorates at 250-μs time-step as shown in Figure 4-17(c). Since the number of harmonic factors is limited (k = 5), some high-frequency content of transients at the beginning of the fault are not fully captured, although the difference between the two waveforms is marginal.

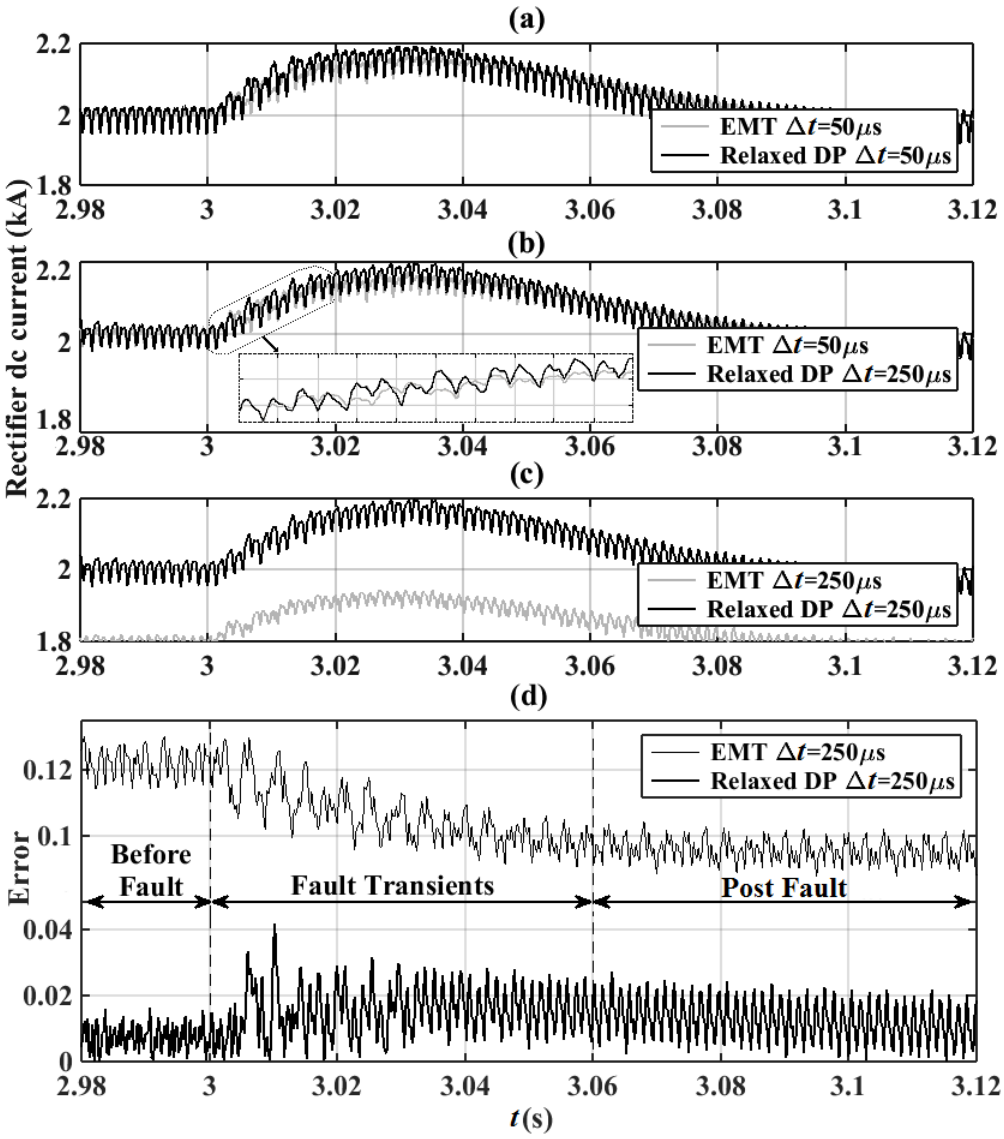

Figure 4-17 DC current for 3Φ-G fault (a) 50 μs for both models, (b) different time-steps, and (c) 250 μs time-step for both models, and (d) the resulting error

Table 4-6 Computational time comparison for various time-steps in IEEE 12-bus system

Model Type	*CPU Time (sec)*	*CPU Time gain*
EMT 50 μs	33.71	N/A
Relaxed 50 μs	6.64	33.71/6.64=5.08
Relaxed 250 μs	3.07	33.71/3.07=10.98

Table 4-6 shows the computational gain of various models using a larger time-step with a DP-based model rather than a conventional EMT one. In this regard, the computational burden on CPU is decreased by 90.89%. It is while using such large time-step for EMT model results in accuracy loss.

Table 4-7 Normalized error of DC current in IEEE 12-bus for pre-fault, fault transients, and post-fault intervals

Model Type	*Pre-fault (%)*	*Fault transients (%)*	*Post-fault (%)*
EMT 50 μs	N/A	N/A	N/A
EMT 250 μs	12.29	12.97	10.16
Relaxed 50 μs	0.85	1.62	1.26
Relaxed 250 μs	1.01	4.52	2.48

Table 4-7 shows the accuracy loss of using a relaxed DP-based model in comparison with EMT one at different time-steps. Increasing the time-step for relaxed DP model causes less than 5% loss of accuracy while for the EMT one this value is more than 10%.

4.5 Chapter Summary

In this chapter relaxed dynamic phasor model for LCC-HVDC transmission system was introduced and its operation under balanced as well as unbalanced conditions was studied. To achieve such a model, the following steps were taken:

- Developing time-domain expressions for switching functions based on voltage and current waveforms
- Extracting dynamic phasor equivalents for developed time-domain expressions

- Simplifying and replacing exact DP-based switching functions with their approximate ones based on symmetry in the resulting functions.

It was shown that such relaxed model would benefit from less complexity of simplified switching functions and at the same time would keep the accuracy at an acceptable level. Then this model was used in CIGRE benchmark and IEEE 12-bus systems and its accuracy was proved by comparing its results with EMTDC.

Chapter 5

Real-Time Implementation of the DP-Based LCC-HVDC Model

5.1 Introduction

Planning, design, and testing of power generation and transmission systems rely extensively on power system simulators. The first simulators were large and expensive physical systems whose operation and maintenance required highly skilled technical teams. With the advancement of computing hardware and development of sophisticated power system component modelling techniques, these so-called analogue simulators are now replaced with purely digital (real-time) ones. Electromagnetic transients, protection, control, and electromechanical transient studies are among the applications for such real-time simulators. The system in [60] is considered as the first DSP-based real-time simulator initially introduced for control system testing of an HVDC system [58] combining real-time features of analogue HVDC simulators with the accuracy and flexibility of digital simulation programs.

5.2 Real-Time Model for LCC

LCC-HVDC systems offer many advantages to the power system due to their fast, flexible, and effective control systems. Therefore, an appropriate control and protection strategy becomes an inevitable part of HVDC design. Despite the fact that control concepts are well stablished, new installations have their own challenges necessitating specialized control strategies for LCC-HVDC systems.

The importance of testing and achieving reliable and accurate control software and hardware before installation was the main motivation for using the first real-time digital simulator [58]. In this regard, having accurate models for converter valve groups including transformers, thyristor valves, valves arresters and snubber circuits is of great importance. As shown in Chapter 4, a DP-based model for a valve group shows proper performance in large electric networks. Therefore, such a model can also facilitate real-time testing of control schemes for HVDC-LCC systems if it is appropriately migrated to a real-time simulator. The real-time simulation platform used in this study is RTDS real-time simulator, whose user interface software wherein new component models may be developed is called RSCAD.

RSCAD is a digital simulation program associated with electromagnetic transient phenomena; it benefits from real-time operation using dedicated hardware. All such programs are essentially based on Dommel's methods [55] where inductors and capacitors are modeled as current sources, known also as history terms, in parallel with resistors. The same approach can be applied to other electric components such as transformers, switching valves, transmission lines, etc.

Since with such an approach the entire electric network becomes a combination of current sources and resistors, nodal analysis becomes a convenient method for finding the system solution at the beginning of each simulation time step.

Before the introduction of RTDS, digital electromagnetic transient simulation was limited to non-real-time applications and hence many obstacles in physical equipment testing existed. In non-real-time simulators such as PSCAD/EMTDC or EMTP, simulation of a certain time period will take a length of time that is determined by the computer's resources and the complexity of the system under consideration. However, for field-like testing of control and protection devices, one needs to input simulated waveforms in real-time. In this regard, all the calculations must be conducted within a single simulation time step to maintain synchronism with a real clock.

The relaxed DP-based model introduced in Chapter 4 not only benefits from simpler computations compared to the other DP models, but also has fewer nodes compared with existing EMT models used in RSCAD (see Figure 5-1). In real-time simulators, two electric nodes will be assigned to each component in the simulation platform. As the number of electric nodes increases in the system under consideration, more processing power will be needed for simulating the case study. Implementing a real-time model for a 6-pulse bridge, one can save four electric nodes by applying DP model rather than the EMT one. This will make the proposed model a more convenient option for real-time applications with reduced number of nodes and less hardware requirements accordingly.

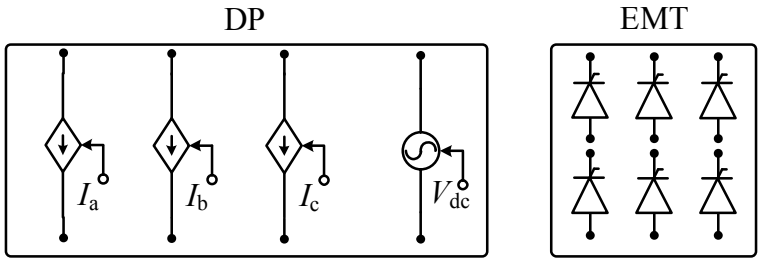

Figure 5-1 Nodes requirement for DP- and EMT-based 6-pulse bridges

The same set of current and voltage sources as in Figure 5-1 are applied in RSCAD to implement the proposed relaxed DP model. Figure 5-2 illustrates the necessary components beside controlled voltage and current sources for developing the relaxed DP-based model in RSCAD.

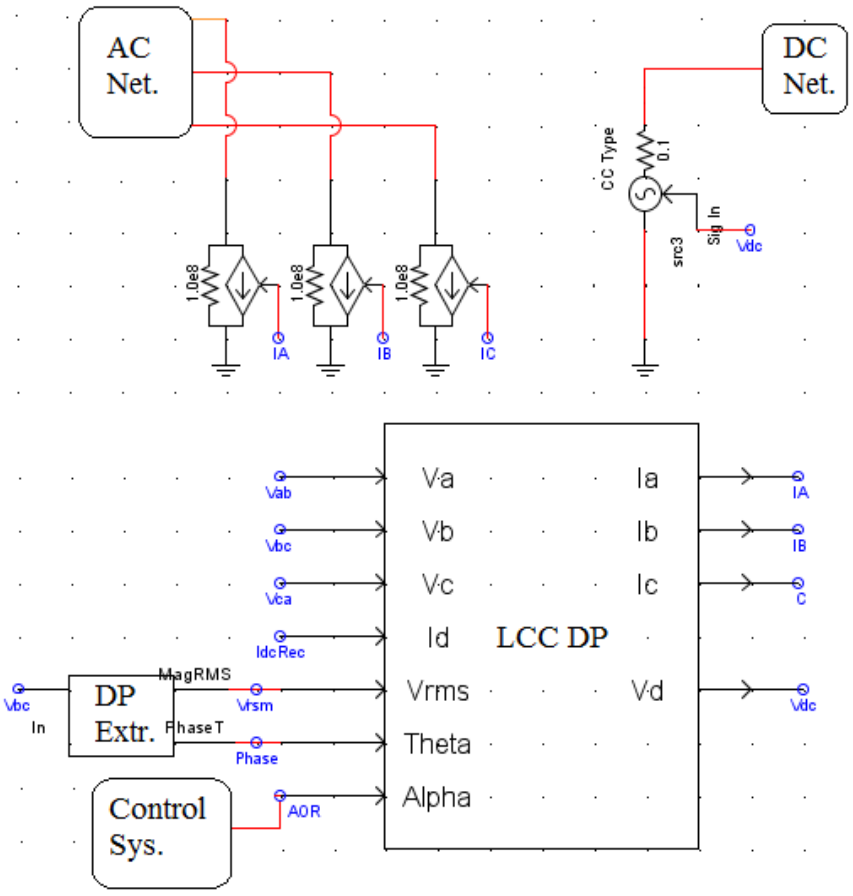

Figure 5-2 Relaxed DP-based model of LCC in RSCAD

The DP extractor block, as its name suggests, generates magnitude and phase of the input signal based on the concept introduced in [59]. Such information is used in LCC DP block where the AC side currents and DC side voltage are built out of the DC current and AC voltages, respectively. This is done based on the concept of switching functions.

In order to validate the developed model in RSCAD, the system in Figure 4-6 is used. The only difference will be the fault time. In this section, a single-phase-to-ground fault at phase-*a* is applied at t = 0.1 s. Figure 5-3 shows the DC current waveform for four different models: EMT in PSCAD/EMTDC, relaxed DP in PSCAD/EMTDC, EMT in RSCAD, and relaxed DP in RSCAD. Five harmonics are used in DP-based models and the simulation time step in both DP and EMT RSCAD and DP PSCAD/EMTDC models is set to 150 μs. The EMT model PSCAD/EMTDC executed with a 50 μs time-step is used as the reference waveform for benchmarking the other models.

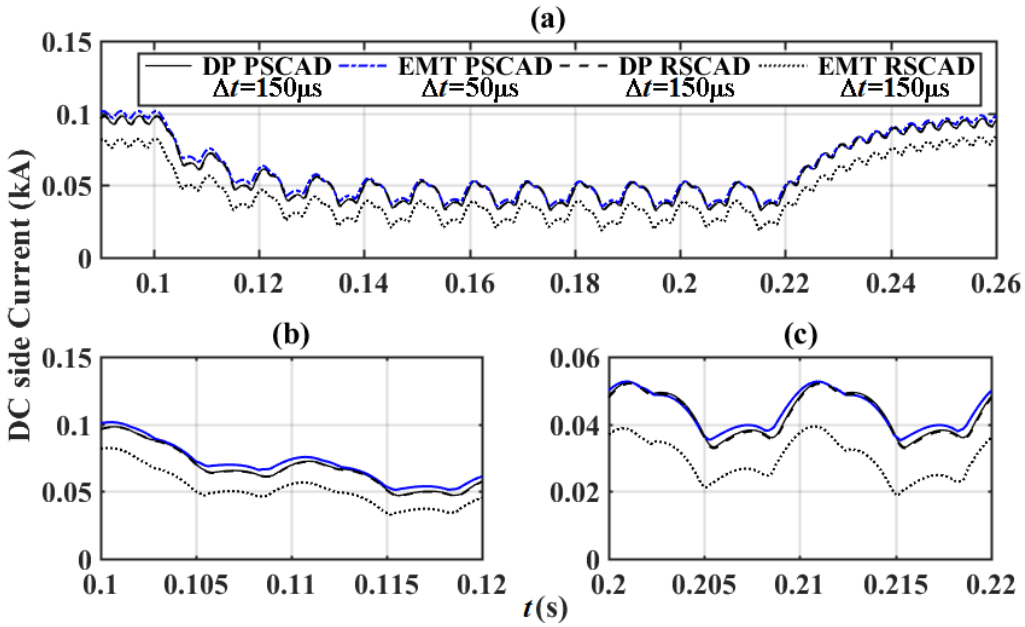

Figure 5-3 DC current (a) during, (b) prior, and (c) after phase-a-to-ground fault

As Figure 5-3 illustrates, there is perfect matching between DP models in PSCAD/EMTDC and RSCAD even during fault transients. Such performance can be considered as the proof for validity of developed relaxed DP-based model in RSCAD.

Since a large time step is applied in deriving the result, the inaccuracy in simulation results is not negligible when one compares the EMT-based model in RSCAD with the one in PSCAD/EMTDC. Table 5-1 compares the normalized error for each model in comparison with the EMT PSCAD/EMTDC one for various time intervals.

Table 5-1 Normalized error in DC current before fault, during its transients, and in steady state for different models

Model Type	*Pre-flt. (%)*	*Flt. Transient (%)*	*Post-flt. (%)*
EMT PSCAD/EMTDC (Δt = 50 μs)	-	-	-
Relaxed DP PSCAD/EMTDC (Δt = 150 μs)	0.58	0.42	1.18
EMT RSCAD (Δt = 150 μs)	21.61	48.21	16.62
Relaxed DP RSCAD (Δt = 150 μs)	0.58	0.42	1.18

According to Table 5-1, the inaccuracy in generating the DC current can reach almost 50%, which is not acceptable.

Although the PSCAD/EMTDC and RSCAD/RTDS are both EMT-based simulation platforms, the former benefits from more detailed models since it does not face the real-time simulation limits while the latter has to apply specialized techniques to be able to support real-time simulation requirements. For example, real-time simulations do not include interpolation techniques that allow usage of larger simulation time steps without sacrificing accuracy of simulating switching events.

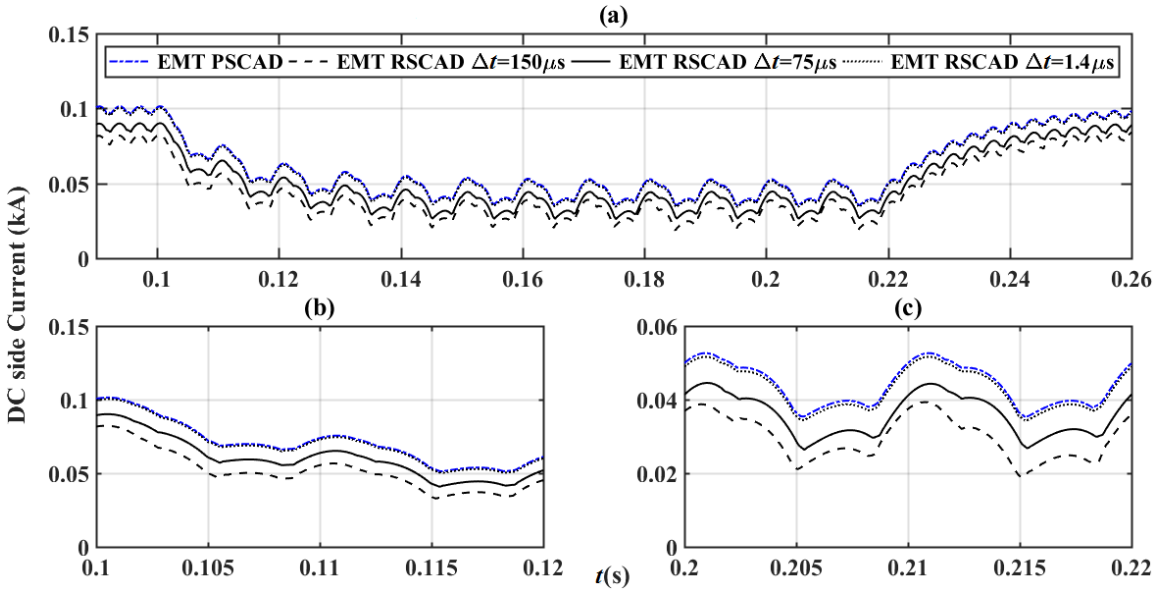

Figure 5-4 DC current (a) during, (b) prior, and (c) after phase-a-to-ground fault for various time steps in RSCAD

In order to improve the accuracy level of the real-time EMT simulation model, one must decrease the simulation time step as shown in Figure 5-4. As the simulation time step decreases from 150 μs to 1.4 μs, the DC current waveform gets closer to the EMT model result from PSCAD/EMTDC. However, reaching a small time step as low as 1.4 μs requires application of a new set of models in the small time step library of RSCAD. It is with the developed relaxed DP model in RSCAD the LCC dynamics may be simulated accurately even with a large 150 μs time step.

Table 5-2 shows the effect of reducing the simulation time step on performance of EMT-based model of LCC in RSCAD. As the simulation time step decreases, the difference between EMT-based LCC model in RSCAD and PSCAD also decreases.

Table 5-2 Normalized error in DC current before fault, during its transients, and in steady state for various simulation time steps

Model Type	*Pre-flt. (%)*	*Flt. Transient (%)*	*Post-flt. (%)*
EMT PSCAD/EMTDC (Δt = 50 μs)	-	-	-
EMT RSCAD (Δt =150 μs)	21.61	48.21	16.62
EMT RSCAD (Δt = 75 μs)	12.38	28.97	10.44
EMT RSCAD (Δt = 1.4 μs)	0.49	0.52	0.38

Beside the fact that using small time steps requires use of a specialized library of components in RSCAD, the applicable time step itself is also limited. The user can only apply a time step between 1.4 μs – 3.75 μs, which implies heavy computations and additional use of limited of hardware.

To further investigate the validity of developed DP-based model in RSCAD, DC side voltage waveform is included as in Figure 5-5.

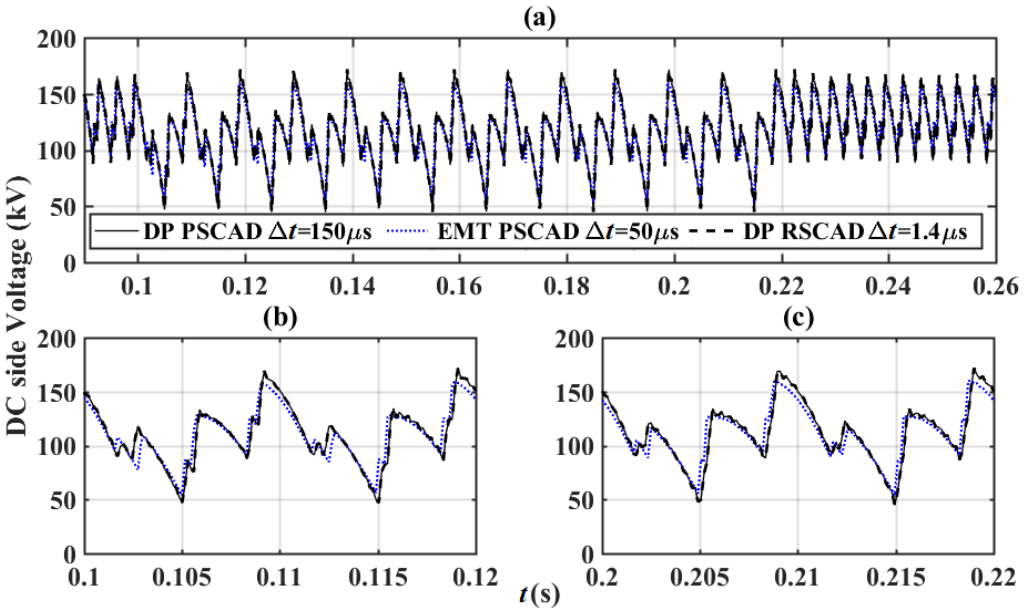

Figure 5-5 DC voltage (a) during, (b) prior, and (c) after phase-a-to-ground fault

Figure 5-6 depicts phase-a current at AC side of the bridge. There is perfect conformity between PSCAD/EMTDC and RSCAD models even during fault transients.

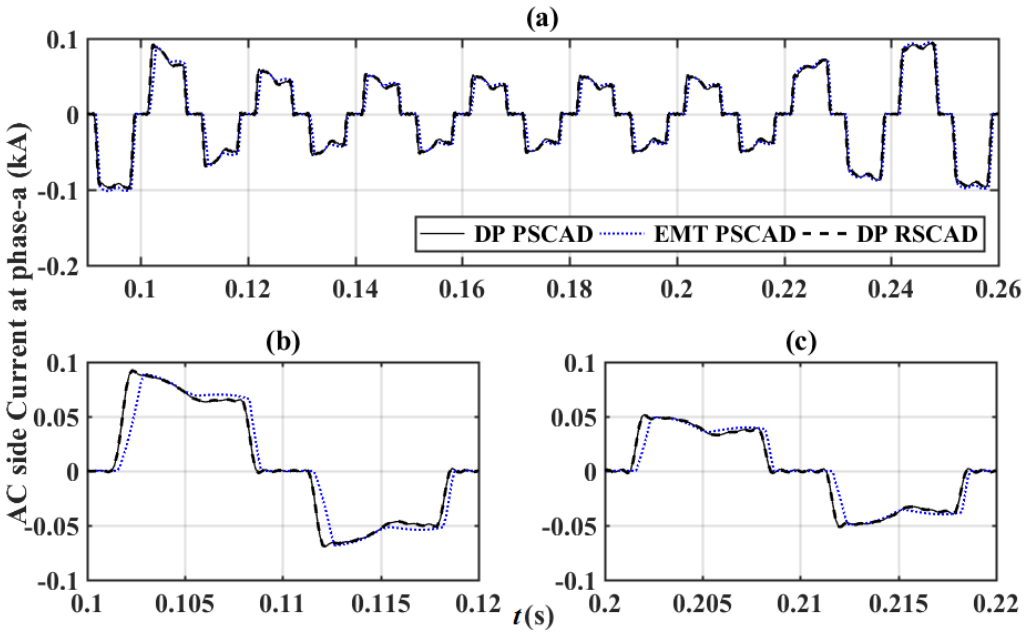

Figure 5-6 AC current (a) during, (b) prior, and (c) after phase-a-to-ground fault

5.3 HIL Simulations of the Proposed DP-based LCC Model

As previously discussed, designing, tuning, and testing of a real HVDC controller in hardware-in-the-loop setup can be considered as one of the main advantages of having a real-time model of LCC [58]. In this regard, one needs to be familiar with basic control strategies for different HVDC schemes.

The basic control strategy for a conventional point-to-point HVDC scheme is operating one side of the DC system as a voltage source and the other as a current source

[61]. However, there is a need to include many other additional features to such a simple controller due to the presence of circuit and control limitations, characteristics of AC grid, fault conditions, etc. It becomes even more complicated to control the HVDC terminals when one includes multi-terminal schemes where there may be more than one sending and receiving end [62].

In general, basic control methods for point-to-point HVDC systems can be investigated in four categories:

- Current Margin Control [63-67]
- Coordinated Current Control [68-70]
- Voltage Margin Control [71-73]
- AC Voltage Control [74-77]

Using some form of Current Margin Control (CMC) is inevitable in almost all LCC-based HVDC systems. Initially, CMC was developed for LCC-based systems to ensure maintenance of maximal voltage level permitted by the AC system at the DC terminals to minimize their power losses and reactive power consumption. This can be achieved by operating either the sending end (rectifier side) with minimum firing angle, α_{min}, or the receiving end (inverter side) with minimum excitation angle, γ_{min}. With such an arrangement, DC voltage becomes dependent on DC current based on equivalent commutation resistance [61] of LCC as in Figure 5-7(b).

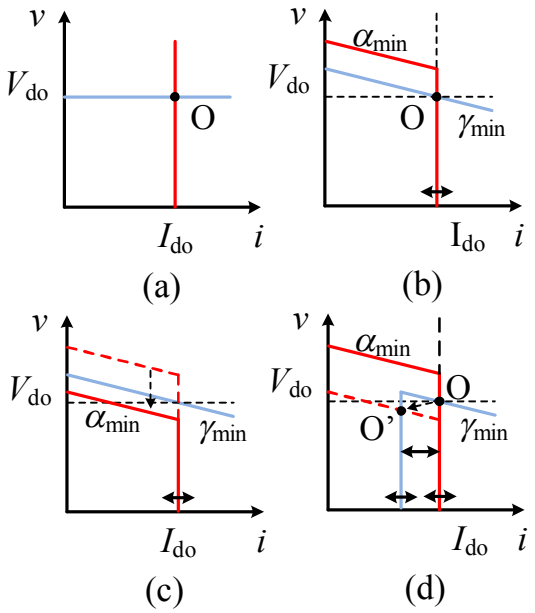

Figure 5-7 Current Margin Control of LCC-HVDC systems based on (a) simple V-I, (b) $\alpha_{min}/\gamma_{min}$ (c) voltage sag, and (d) cooperative ends

The AC terminal at the current controlling end might experience a voltage sag as shown in Figure 5-7(c), which results in loss of operating point. In order to prevent it, both the sending and receiving ends have to incorporate a constant-current control mode as depicted in Figure 5-7(d).

To guarantee stable performance of LCC-HVDC system during possible variations in AC grid impedance, the basic CMC requires some modifications [78]. For example, if the AC grid impedance increases at the receiving end, then I-V characteristic will have a steeper slope as shown in Figure 5-8(a).

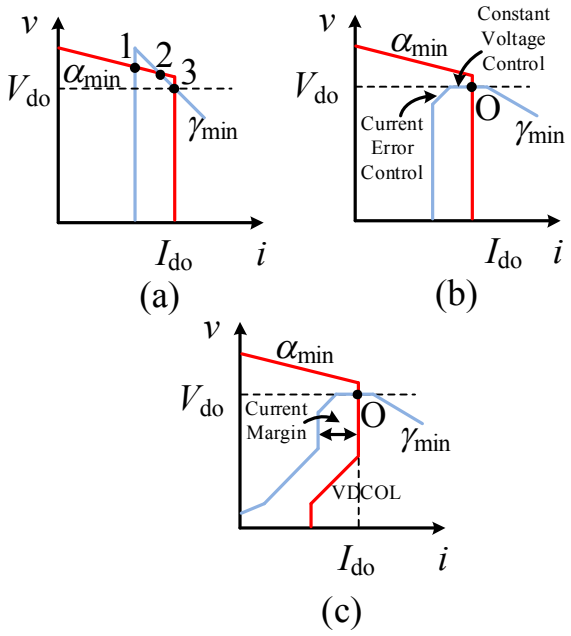

Figure 5-8 Improvements in Current Margin Control with (a) steeper slope, (b) adding positive slope, and (c) VDCOL

Adding a constant firing angle mode (positive slope) or constant voltage mode or combination of both can prevent formation of multiple operating points [78] as in Figure 5-8(b).

Figure 5-8(c) illustrates the inclusion of Voltage Dependant Current Order Limits (VDCOL) for reducing terminal current during AC voltage sag or fault and limiting the power flow accordingly [79]. Furthermore, limiting the minimum firing angle of the inverter side results in avoiding inadvertent change from inversion to rectification mode.

Better dynamic response can be achieved in a DC link by using droop control, which allows sending and receiving ends to participate in current regulation as in Coordinated Current Control (CCC) mode [68-70]. CCC can be considered as a modified version of CMC where droop characteristics are incorporating into both ends control to reduce the reliance on commutation as shown in Figure 5-9. To do so, a current-dependant voltage

source characteristic is assigned to the controller through lines AB and CD. However, such modification results in higher losses and more reactive power consumption due to the operation at a lower DC voltage level.

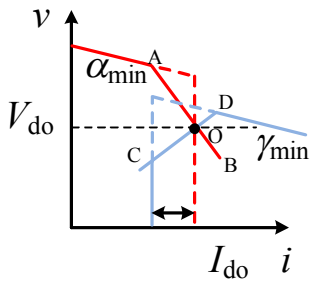

Figure 5-9 Coordinated Current Control of LCC-HVDC systems

Voltage Margin Control (AMC) and AC Voltage Control (AVC) are applied in VSC-based HVDC systems, which is out of scope of this research. Therefore, no details are included regarding their performance and only some references are provided for the readers [71-77].

5.3.1 HIL testing of a PI CMC for Relaxed DP-based LCC

A basic Current Margin Control is implemented on a DSP-based processor to control the proposed relaxed DP-based model in a six-pulse rectifier configuration as in Figure 5-10.

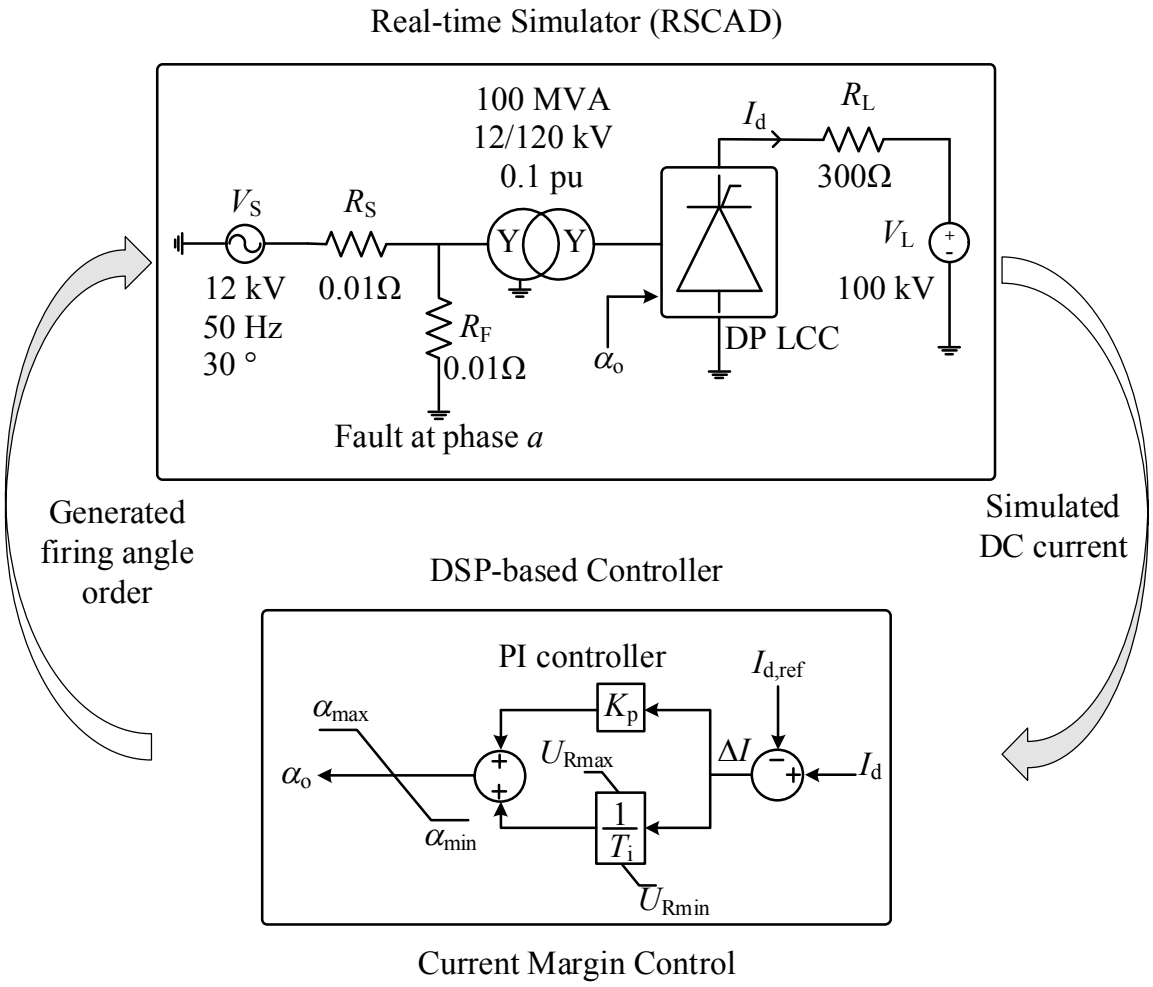

Figure 5-10 Simple DC current controller HIL test model

The DP LCC's firing angle is controlled with a feedback control system with parameters as in Table 5-3.

Table 5-3 Current controller parameters

Parameter	***Value***
K_p	0.63
T_i	0.001524
U_{Rmax}, U_{Rmax}	1.0,-1.0
α_{max}, α_{min}	150.0, 5.0

To set the DC current to its reference level, DC voltage will be regulated according to the generated firing angle according to the following equation.

$$V_d = \frac{3\sqrt{2}}{\pi} v_l \cos(\alpha) - \frac{3}{\pi} X_l I_d \tag{5-1}$$

For example, if there is need for more current, then firing angle will be decreased and will cause an increment in DC voltage. The limit for such increment will be $\alpha_{\min}$, which is usually set to 5º to allow a successful turn-on of the valves.

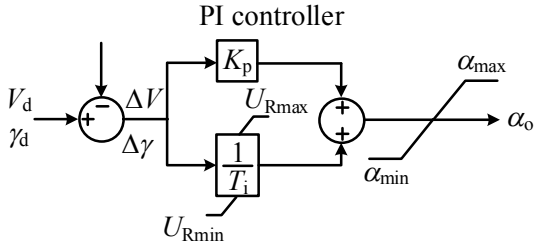

Figure 5-11 Simple excitation angle or voltage controller model

On the inverter side, extinction angle γ or voltage control are the two common controlling approaches where the former benefits from its simplicity and the later has advantages in increased stability margin and less reactive power consumption. Both methods can be implemented in a feedback control system like Figure 5-11.

The basic current controller of Figure 5-10 is implemented on a DSP-based card connected to the DP-based LCC model in RSCAD and the results are validated against the same system built entirely in RSCAD using DP-based model.

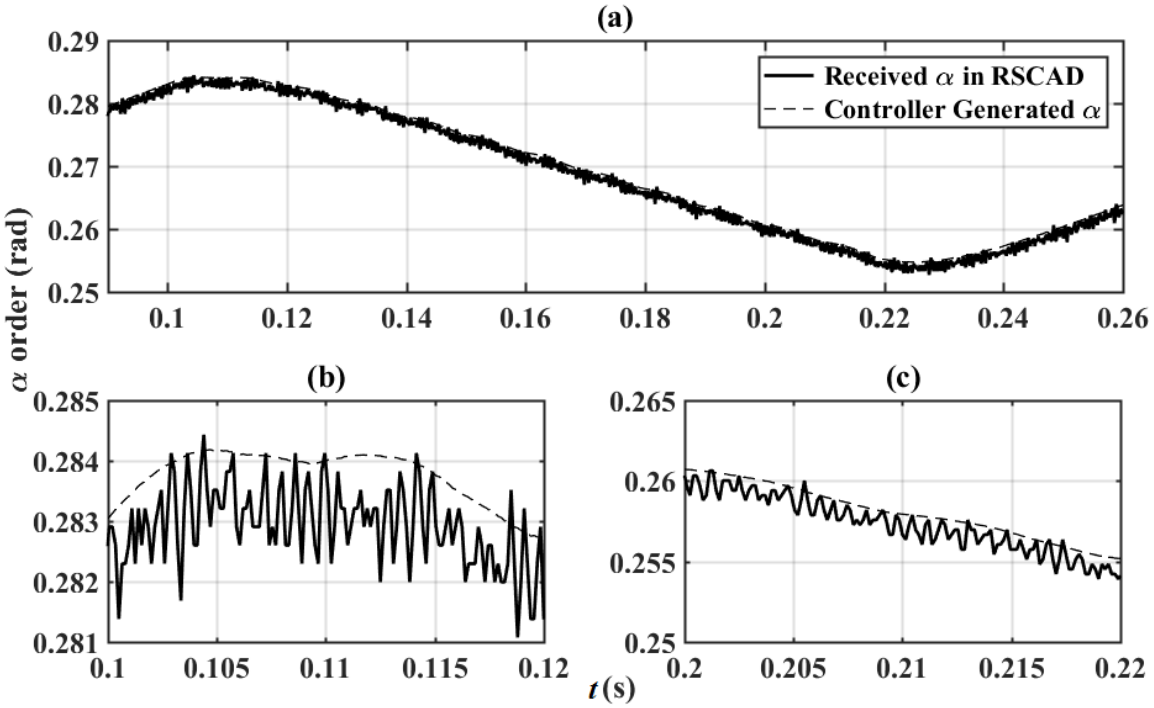

Figure 5-12 Actual controller generated firing angle (a) during, (b) prior, and (c) after phase-a-to-ground fault

As Figure 5-12 illustrates, the firing angle being generated in the actual controller is accompanied with some noise when received in RSCAD simulator through a Giga-Transceiver Analog Input (GTAI) card. The source for such noise is external and it not related to the switching of LCC system. Noise cancelation methods can be applied to improve the receiving signals if their quality is not satisfactory. In the same way, the measured DC current in RSCAD will be accompanied by some noise when it is transferred through the Giga-Transceiver Analog Output (GTAO) card as shown in Figure 5-12. However, less noise is observed in the current rather than the firing angle because firing angle is always changing over time as an output of DP-extractor block.

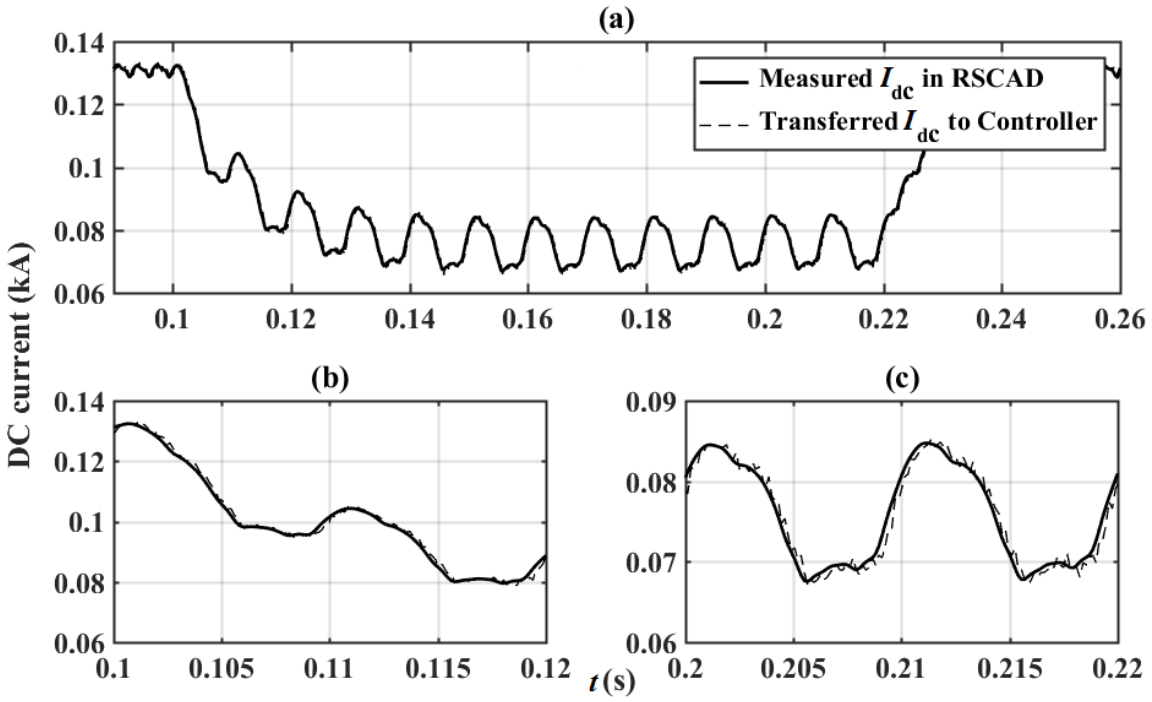

Figure 5-13 Actual controller generated DC current (a) during, (b) prior, and (c) after phase-a-to-ground fault

In order to investigate the validity of the generated current and firing angle, one must build the exact same controller in RSCAD and apply the same fault. An acceptable overlap between the two systems' results will show the accuracy of the HIL test setup.

In this regard, the generated firing angles of actual and simulated controllers are shown in Figure 5-14. Beside small errors in the actual controller's firing angle, there is also some delay between the two signals. Such time delay is expected due to the time it takes to transfer information to the actual controller and then generate the firing angle. If one considers the time it takes to transfer the firing angle back to RTDS, there will be more time delay and inaccuracy.

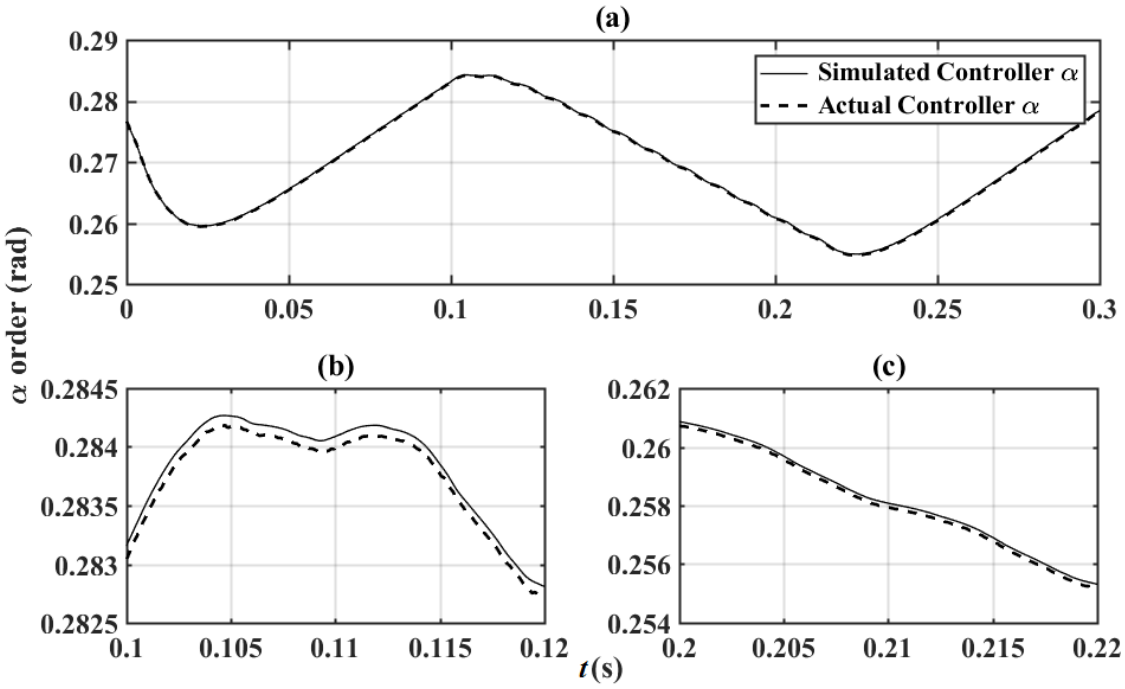

Figure 5-14 Simulated and Actual controller generated firing angles (a) during, (b) prior, and (c) after phase-a-to-ground fault

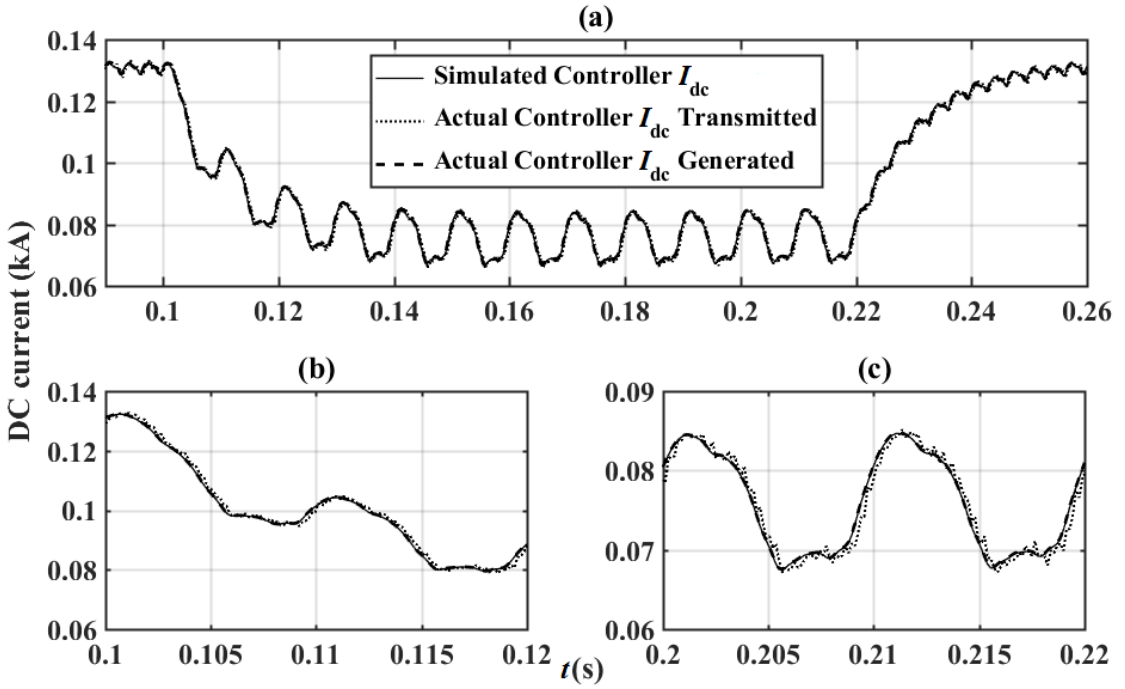

Figure 5-15 Simulated and Actual controller DC currents (a) during, (b) prior, and (c) after phase-a-to-ground fault

As Figure 5-15 illustrates, the actual controller generates an acceptable DC current level in the RSCAD when the firing angle information is transmitted back into the RSCAD model and used to control the DP-based LCC model.

5.3.2 HIL testing of a PI CMC for IEEE 12-bus system

Combining the extinction angle γ control with DC current control results in a simple control strategy for a DC link that is embedded into the IEEE 12-bus system and replaces the AC line between buses 7 and 8 as introduced in the last chapter. Figure 5-16 depicts the control system implemented in a DSP-based controller for a HIL test of the modified IEEE 12-bus system simulated in RSCAD.

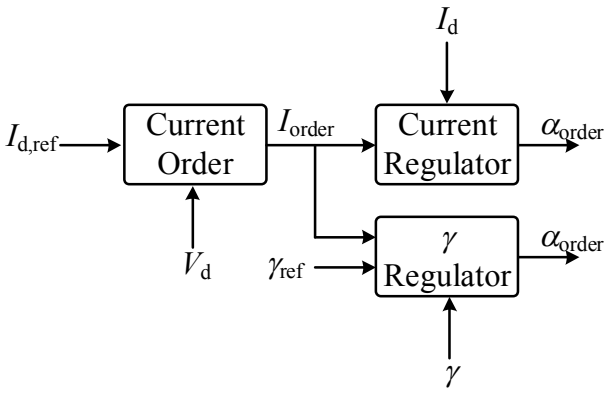

Figure 5-16 Current Control and Constant Extinction Angle combination

Applying a three-phase-to-ground fault at bus number 4 at t = 0.1 s results in a DC current as depicted in Figure 5-17.

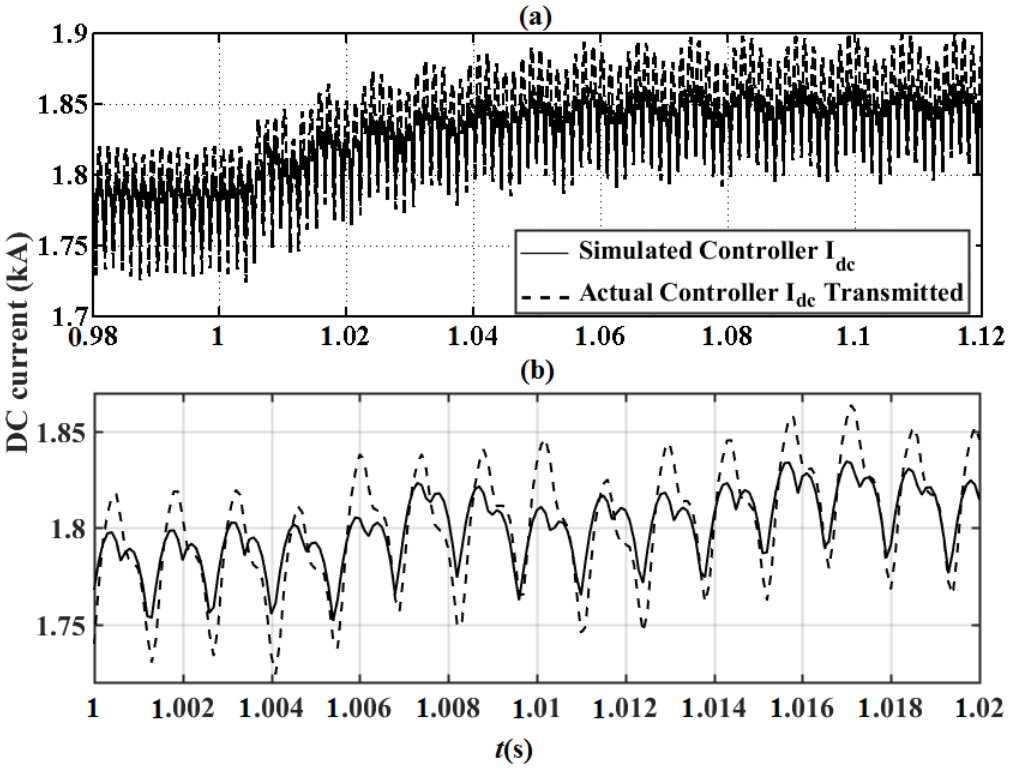

Figure 5-17 Simulated and Actual controller DC currents for a three-phase-to-ground fault (a) during fault and (b) right after the fault

As Figure 5-17 depicts, there is an acceptable overlap between the two controllers results.

5.4 Chapter Summary

In this chapter the proposed relaxed dynamic phasor model for LCC-HVDC transmission system was redeveloped in a real-time digital simulator and its performance under balanced as well as unbalanced conditions was studied. For this purpose, various control methods of LCC were introduced and a simple version was implemented in a DSP-based controller for a HIL test of the model. It was shown that the relaxed model

benefits from less number of nodes and a better accuracy in large simulation time steps. This would eliminate the need for developing a new set of library in a software such as RSCAD to achieve the accuracy level achievable using a small time step.

Chapter 6

Contributions, Conclusions and Recommendations for Future Work

6.1 Introduction

This thesis has contributed to the development of a new dynamic phasor model for an LCC-HVDC system. The performance of the developed model is examined under balanced and unbalanced operating conditions and validated against EMT-based models in both off-line and real-time simulators. The proposed DP-based model benefits from simple symmetrical switching functions, which offer marked computational benefits while maintaining a high level of accuracy, beside a reduced number of nodes in the equivalent circuit. The DP-based model is readily embeddable in an off-line or real-time EMT simulator and replaces the conventional, switch-based models commonly used for EMT studies. This replacement allows use of larger simulation time steps with negligible impact on accuracy and offers marked gains in simulation speed and node requirements, as evidenced by the simulation results presented in the thesis. The research quantified the

accuracy and simulation time acceleration gains of the proposed DP-based model in the context of several examples. This chapter summarizes the contributions of the thesis and also identifies future research directions.

6.2 Main Contribution of the Thesis

The followings are the main contributions of this thesis:

1) This thesis proposed a novel technique in applying dynamic phasors for modelling a 6-pulse Graetz bridge. It was then extended to include any arbitrary pulse-number bridges in PSCAD/EMTDC as an off-line EMT-based simulation software. Such implementation provided the opportunity for comparing switch-based EMT models with the DP-based ones in time domain in terms of accuracy and computational requirements.
2) Developing a real-time version of the proposed relaxed dynamic phasor-based model of LCC was another important achievement in this work. With a real-time implementation, one can test actual HVDC controllers by applying the new LCC model, which results in a better tuning due to the accuracy offered by this new model without recourse to excessively small time steps. Furthermore, since the proposed model needs fewer electric nodes in comparison with the switch-based models in RSCAD library, application of DP-based model would require less computation power and it will facilitate simulation of large electric networks.

6.2.1 Thesis Publications

The aforementioned contributions have led to the following publications so far.

- A. Bagheri-Vandaei and S. Filizadeh, "Generalised extended-frequency dynamic phasor model of LCC-HVDC systems for electromagnetic transient simulations," *IET Gener., Transm. & Distrib.*, Mar. 2018.
- A. B. Vandaei, S. Filizadeh, K. Mudunkotuwa and E. Tara, "Real-time implementation of an enhanced dynamic phasor-based three-phase phase-locked loop for line-commutated converters," *2018 IEEE International Conference on Industrial Technology (ICIT)*, Lyon, France, 2018, pp. 812-817.

6.3 Future Work

Lack of operating information such as a direct γ measurement signal, can be considered as one of the main limitations for the proposed models in both PSCAD and RSCAD. Adding such a feature would provide the opportunity to use the proposed model in real world study applications. Furthermore, since multiples of fundamental frequency are added to build switching functions, if subharmonics exist, they will not be addressable. In that case, adding a different base frequency can extend the generality of the developed model.

6.3.1 Suggestions for Future Work

This research has laid the foundations for relaxed DP-based modelling of LCC-HVDC systems. The findings of this study open up further research opportunities in the following areas.

1) Applicability of the proposed DP extractor as a replacement for conventional PLLs as presented in the conference paper. This should be further investigated and the possibility of implementing the DP-based PLL in real world must be explored.
2) The thesis showed that the DP model can be applied in large time-steps such as 150-µs. However, the system frequency range and its effect on maximum possible simulation time step needs to be studied in depth.
3) With the addition of a complete set of controlling signals, one can further investigate the applications of proposed real-time model by connecting it to an actual HVDC controller.
4) Further improvement can be achieved in processing time of the DP-based LCC model by applying parallel processing techniques in derivation of three switching functions for each of three AC phases.
5) To extend the generality of the proposed model, switching functions can be modified in a way to address additional operating phenomena such as long overlap periods resulting in simultaneous conduction of more than three switches.

Bibliography

[1] V.J. Marandi, V. Dinavahi, K. Strunz, J.A. Martinez, A. Ramirez, "Interfacing Techniques for Transient Stability and Electromagnetic Transient Programs," *IEEE Trans. Power Delivery*, Vol 24, No. 4, pp. 2385-2395. 2009.

[2] R. R. O. Yang, "A Comparison of EMT, Dynamic Phasor, and Traditional Transient Stability Models," M.Sc. Thesis, University of Manitoba, 2014.

[3] Juan A. Martinez-Velasco, *Transient Analysis of Power Systems:* Solution Techniques, Tools and Applications, Wiley-IEEE Press, 2014.

[4] M. Daryabak *et al*., "Modeling of LCC-HVDC Systems Using Dynamic Phasors," *IEEE Transactions on Power Delivery*, Vol. 29, No. 4, pp. 1989-1998, Aug. 2014.

[5] S. Chiniforoosh *et al*., "Definitions and Applications of Dynamic Average Models for Analysis of Power Systems," *IEEE Transactions on Power Delivery*, Vol. 25, No. 4, pp. 2655-2669, Oct. 2010.

[6] R. L. Sellick and M. Åkerberg, "Comparison of HVDC Light (VSC) and HVDC Classic (LCC) site aspects, for a 500MW 400kV HVDC transmission scheme," 10th IET International Conference on AC and DC Power Transmission (ACDC 2012), Birmingham, 2012, pp. 1-6.

[7] A. Davoudi and J. Jatskevich, "Parasitics Realization in State-Space Average-Value Modeling of PWM DC–DC Converters Using an Equal Area Method," *IEEE Transactions on Circuits and Systems I: Regular Papers*, Vol. 54, No. 9, pp. 1960-1967, Sept. 2007.

[8] V. A. Caliskan, O. C. Verghese, A. M. Stankovic, "Multifrequency averaging of dc-dc converters," *IEEE Trans. Power Electronics*, vol. 14, pp. 124-133, Jan 1999.

[9] Z. Ye, P. K. Jain and P. C. Sen, "Phasor-Domain Modeling of Resonant Inverters for High-Frequency AC Power Distribution Systems," in *IEEE Transactions on Power Electronics*, vol. 24, no. 4, pp. 911-923, April 2009.

[10] D. Maksimovic, A. M. Stankovic, V. J. Thottuvelil and G. C. Verghese, "Modeling and simulation of power electronic converters," *Proceedings of the IEEE*, vol. 89, no. 6, pp. 898-912, Jun 2001.

[11] P. Mattavelli, G. C. Verghes e, and A. M. Stankovic, "Phasor dynamics of thyristor-controlled series capacitor systems," *IEEE Trans. on Power Systems,* vol. 12, no. 3, pp. 1259-1267, Aug 1997.

[12] P. C. Stefanov and A. M. Stankovic, "Modeling of UPFC operation under unbalanced conditions with dynamic phasors," *IEEE Trans. on Power Systems,* vol. 17, no. 2, pp. 395-403, May 2002.

[13] S. Rajesvaran and S. Filizadeh, "Modeling modular multilevel converters using extended-frequency dynamic phasors," *2016 IEEE Power and Energy Society General Meeting (PESGM)*, Boston, MA, 2016, pp. 1-5.

[14] H. Saad *et al*., "Dynamic Averaged and Simplified Models for MMC-Based HVDC Transmission Systems," in *IEEE Transactions on Power Delivery*, vol. 28, no. 3, pp. 1723-1730, July 2013.

[15] A. Stankovic, B. Lesieutre, and T. Aydin, "Modeling and analysis of single-phase induction machines with dynamic phasors," *IEEE Trans. on Power Systems,* vol. 14, no. 1, pp. 9-14, Feb 1999.

[16] A. M. Stankovic, S. R. Sanders, and T. Aydin, "Dynamic phasors in modeling and analysis of unbalanced polyphase AC machines," *IEEE Trans. on Energy Conversion,* vol. 17, no. 1, pp. 107-113, March 2002.

[17] A. M. Stankovic, B. Lesieutre, T. Aydin, "Applications of generalized averaging to synchronous and induction machines," in *in Proc. North American Power Symposium*, B. Lesieutre, 1996.

[18] P. Zhang, J.R. Martí, H.W. Dommel, "Synchronous Machine Modeling Based on Shifted Frequency Analysis," IEEE Trans. Power Systems, Vol. 22. No. 3, pp.1139-1147. 2007.

[19] P. Mattavelli, A. M. Stankovic, and G. C. Verghese, "SSR analysis with dynamic phasor model of thyristor-controlled series capacitor," *IEEE Trans. on Power Systems,* vol. 14, no. 1, pp. 200-208, Feb 1999.

[20] K. M. H. K. Konara, "Interfacing Dynamic Phasor Based System Equivalents to an Electromagnetic Transient Simulation," M.Sc. Thesis, University of Manitoba, 2015.

[21] T. H. Demiray, "Simulation of power system dynamics using dynamic phasor models," Ph.D. dissertation, Swiss Federal Institute of Technology, 2008.

[22] F. Plumier, “Co-simulation of Electromagnetic Transients and Phasor Models of Electric Power Systems," Ph.D. dissertation, University of Liège, 2015.

[23] V. Venkatasubramanian, H. Schattler, and J. Zaborszky, “Fast time-varying phasor analysis in the balanced three-phase large electric power system," IEEE Transactions on Automatic Control, Vol. 40, No. 11, pp. 1975-1982, November 1995.

[24] A. M. Stankovic and T. Aydin, “Analysis of asymmetrical faults in power systems using dynamic phasors,” *IEEE Transactions on Power Systems*, vol. 15, no. 3, pp. 1062-1068, Aug 2000.

[25] L. Hu and R. Yacamini, "Harmonic transfer through converters and HVDC links," in *IEEE Transactions on Power Electronics*, vol. 7, no. 3, pp. 514-525, Jul 1992.

[26] S.R. Sanders, J.M. Noworolski, X.Z. Liu, G.C. Verghese, “Generalized Averaging Method for Power Conversion Circuits,” IEEE Trans. Power Elec., Vol. 6, No. 3, pp. 251-259, April 1991.

[27] P. B. Darji and A. M. Kulkarni, “Vector Definitions for Control of Single-Phase and Unbalanced Three-Phase Systems,” *IEEE Transactions on Power Delivery*, vol. 29, no. 5, pp. 2136-2145, Oct. 2014.

[28] P. Zhang, J.R. Martí, H.W. Dommel, “Shifted-Frequency Analysis for EMTP Simulation of Power-System Dynamics,” IEEE Trans. Circuits and Systems, Vol. 57. No. 9, pp.1139-1147. 2010.

[29] C. Liu, A. Bose and P. Tian, “Modeling and Analysis of HVDC Converter by Three-Phase Dynamic Phasor,” *IEEE Transactions on Power Delivery*, vol. 29, no. 1, pp. 3-12, Feb. 2014.

[30] C. Liu, Y. Zhao, C. Wang, H. Li and G. Li, "Superposition feature of the switching functions for the dynamic phasor model of the converters under commutation failure," *IET Generation, Transmission & Distribution*, vol. 9, no. 12, pp. 1448-1454, 9 4 2015.

[31] W. Gang, L. Zhikeng, L. Haifeng, L. Xiaolin and F. Chuang, "Modeling of the HVDC convertor using dynamic phasor under asymmetric faults in the AC system," *2009 International Conference on Sustainable Power Generation and Supply*, Nanjing, 2009, pp. 1-5.

[32] Q. Qi, L. Jiao, Z. Yan, Y. Ni, S. Chen, and F. Wu, "Modeling and simulation of HVDC with dynamic phasors," *in proc. of the CSEE*, 2003.

[33] C. Osauskas, A. Wood, "Small-signal dynamic modeling of HVDC systems," *IEEE Trans. on Power Delivery,* vol. 18, no. 1, pp. 220-225, Jan 2003.

[34] L. Gyugyi and B. R. Pelly, "Static Power Frequency Changers – Theory, Performance, and Applications," Wiley, 1976.

[35] Lihua Hu and R. E. Morrison, "The use of modulation theory to calculate the harmonic distortion in HVDC systems operating on an unbalanced supply," *IEEE Transactions on Power Systems*, vol. 12, no. 2, pp. 973-980, May 1997.

[36] H. Zhu, Z. Cai, H. Liu *et al*., "Hybrid-model transient stability simulation using dynamic phasors based HVDC system model," *Elec. Power Syst. Res.*, Vol. 76, pp. 582-591, Apr. 2006.

[37] T. Yang, S. Bozhko and G. Asher, “Fast functional modelling of diode-bridge rectifier using dynamic phasors,” *IET Power Electronics*, vol. 8, no. 6, pp. 947-956, 6 2015.

[38] Y. Huang, L. Dong, S. Ebrahimi, N. Amiri and J. Jatskevich, “Dynamic Phasor Modeling of Line-Commutated Rectifiers With Harmonics Using Analytical and Parametric Approaches,” *IEEE Transactions on Energy Conversion*, vol. 32, no. 2, pp. 534-547, June 2017.

[39] M. Szechtman, T. Wess, and C. V. Thio, “First benchmark model for HVDC control studies,” *Electra,* vol. 135, pp. 55-75, Apr 1991.

[40] J. Schwartz, E. Rahimi and H. Zareipour, “A modified CIGRE HVDC benchmark model for 60 Hz applications,” *2014 North American Power Symposium (NAPS)*, Pullman, WA, 2014, pp. 1-6.

[41] M. Faruque, Y. Zhang, and V. Dinavahi, "Detailed modeling of CIGRE HVDC benchmark system using PSCAD/EMTDC and PSB/SIMULINK," *IEEE Trans. on Power Delivery,* vol. 21, no. 1, pp. 378-387, January 2006.

[42] S. Jiang, U.D. Annakkage, A.M. Gole, “A Platform for Validation of FACTS Models,” IEEE Trans. Power Delivery, Vol. 2, No. 1, pp. 484-491, 2006.

[43] E. Tara *et al*., “Dynamic Average-Value Modeling of Hybrid-Electric Vehicular Power Systems,” in *IEEE Transactions on Power Delivery*, vol. 27, no. 1, pp. 430-438, Jan. 2012.

[44] J. Jatskevich, S. D. Pekarek and A. Davoudi, “Parametric average-value model of synchronous machine-rectifier systems,” *IEEE Transactions on Energy Conversion*, vol. 21, no. 1, pp. 9-18, March 2006.

[45] A. Cross, A. Baghramian and A. Forsyth, “Approximate, average, dynamic models of uncontrolled rectifiers for aircraft applications,” *IET Power Electronics*, vol. 2, no. 4, pp. 398-409, July 2009.

[46] B. R. Needham, P. H. Eckerling and K. Siri, “Simulation of large distributed DC power systems using averaged modelling techniques and the Saber simulator,” *Applied Power Electronics Conference and Exposition, 1994. APEC '94. Conference Proceedings 1994., Ninth Annual*, Orlando, FL, 1994, pp. 801-807 vol.2.

[47] F. Blaabjerg and K. Ma, “Future on Power Electronics for Wind Turbine Systems,” *IEEE Journal of Emerging and Selected Topics in Power Electronics*, vol. 1, no. 3, pp. 139-152, Sept. 2013.

[48] S. Chiniforoosh *et al*., “Dynamic Average Modeling of Front-End Diode Rectifier Loads Considering Discontinuous Conduction Mode and Unbalanced Operation,” *IEEE Transactions on Power Delivery*, vol. 27, no. 1, pp. 421-429, Jan. 2012.

[49] L. P. Piyasinghe, “Dynamic Phasor Based Analysis and Control in Renewable Energy Integration," Ph.D. dissertation, University of South Florida, 2015.

[50] T. L. Vandoorn, B. Meersman, L. Degroote, B. Renders and L. Vandevelde, “A Control Strategy for Islanded Microgrids With DC-Link Voltage Control,” *IEEE Transactions on Power Delivery*, vol. 26, no. 2, pp. 703-713, April 2011.

[51] A. Emadi, "Modeling and analysis of multiconverter DC power electronic systems using the generalized state-space averaging method," *IEEE Transactions on Industrial Electronics*, vol. 51, no. 3, pp. 661-668, June 2004.

[52] A. Emadi, A. Khaligh, C. H. Rivetta and G. A. Williamson, "Constant power loads and negative impedance instability in automotive systems: definition, modeling, stability, and control of power electronic converters and motor drives," *IEEE Transactions on Vehicular Technology*, vol. 55, no. 4, pp. 1112-1125, July 2006.

[53] A. Davoudi and J. Jatskevich, "Realization of parasitics in state-space average-value modeling of PWM DC-DC converters," *IEEE Transactions on Power Electronics*, vol. 21, no. 4, pp. 1142-1147, July 2006.

[54] H. Atighechi, S. Amini Akbarabadi, J. Jatskevich and S. Chiniforoosh, "Large-signal average modeling of HVDC system transients using parametric and analytical approaches," *2013 IEEE 14th Workshop on Control and Modeling for Power Electronics (COMPEL)*, Salt Lake City, UT, 2013, pp. 1-6.

[55] H.W. Dommel "Digital computer solution of electromagnetic transients in single and multiphase networks," IEEE Trans. Power App. Syst., Vol 88, No. 2, pp. 388–395, April 1969.

[56] K. R. Padiyar, HVDC power transmission systems: technology and system interactions, John Wiley & Sons, 1990.

[57] PSCAD/EMTDC User's Manual, Manitoba HVDC Research Center, Winnipeg, MB, Canada, 2010.

[58] H. Duchen, M. Lagerkvist, R. Kuffel, and R. Wierckx, "HVDC simulation and control system testing using a real-time digital simulator (RTDS)," in *Proc. first international conference on digital power system simulators*, 1995.

[59] K. Mudunkotuwa, S. Filizadeh and U. Annakkage, "Development of a hybrid simulator by interfacing dynamic phasors with electromagnetic transient simulation," in *IET Generation, Transmission & Distribution*, vol. 11, no. 12, pp. 2991-3001, 8 24 2017.

[60] R. Kuffel, J. Giesbrecht, T. Maguire, R. P. Wierckx and P. McLaren, "RTDS-a fully digital power system simulator operating in real time," *Energy Management and Power Delivery, 1995. Proceedings of EMPD '95., 1995 International Conference on*, 1995, pp. 498-503 vol.2.

[61] J. Arrillaga, High Voltage Direct Current Transmission, *2nd ed. Exeter, U.K.: Short Run Press, 1998, Inst. Elect. Eng*.

[62] R. Foerst, G. Heyner, K. W. Kanngiesser and H. Waldmann, "Multiterminal Operation of HVDC Converter Stations," in *IEEE Transactions on Power Apparatus and Systems*, vol. PAS-88, no. 7, pp. 1042-1052, July 1969.

[63] A. Ekstrom and G. Liss, "A Refined HVDC Control System," in *IEEE Transactions on Power Apparatus and Systems*, vol. PAS-89, no. 5, pp. 723-732, May 1970.

[64] L. A. S. Pilotto, M. Roitman and J. E. R. Alves, "Digital control of HVDC converters," in *IEEE Transactions on Power Systems*, vol. 4, no. 2, pp. 704-711, May 1989.

[65] J. Reeve and M. Sultan, "Gain scheduling adaptive control strategies for HVDC systems to accommodate large disturbances," in *IEEE Transactions on Power Systems*, vol. 9, no. 1, pp. 366-372, Feb. 1994.

[66] J. D. Ainsworth, "The Phase-Locked Oscillator - A New Control System for Controlled Static Convertors," in *IEEE Transactions on Power Apparatus and Systems*, vol. PAS-87, no. 3, pp. 859-865, March 1968.

[67] T. Sakurai, K. Goto, S. Irokawa, K. Imai and T. Sakai, "A New Control Method for Multiterminal HVDC Transmission Without Fast Communications Systems," in *IEEE Transactions on Power Apparatus and Systems*, vol. PAS-102, no. 5, pp. 1140-1150, May 1983.

[68] F. Karlecik-Maier, "A new closed loop control method for HVDC transmission," in *IEEE Transactions on Power Delivery*, vol. 11, no. 4, pp. 1955-1960, Oct 1996.

[69] D. Povh, P. Thepparat and D. Westermann, "Analysis of Innovative HVDC Control," *2009 IEEE Bucharest PowerTech*, Bucharest, 2009, pp. 1-7.

[70] D. Povh, P. Thepparat and D. Westermann, "Further development of HVDC control," *2011 IEEE Trondheim PowerTech*, Trondheim, 2011, pp. 1-8.

[71] T. Nakajima and S. Irokawa, "A control system for HVDC transmission by voltage sourced converters," *1999 IEEE Power Engineering Society Summer Meeting. Conference Proceedings (Cat. No.99CH36364)*, Edmonton, Alta., 1999, pp. 1113-1119 vol.2.

[72] T. Nakajima, "Operating experiences of STATCOMs and a three-terminal HVDC system using voltage sourced converters in Japan," *IEEE/PES Transmission and Distribution Conference and Exhibition*, 2002, pp. 1387-1392 vol.2.

[73] L. Livermore, J. Liang and J. Ekanayake, "MTDC VSC Technology and its applications for wind power," *45th International Universities Power Engineering Conference UPEC2010*, Cardiff, Wales, 2010, pp. 1-6.

[74] J. Liang, T. Jing, O. Gomis-Bellmunt, J. Ekanayake and N. Jenkins, "Operation and Control of Multiterminal HVDC Transmission for Offshore Wind Farms," in *IEEE Transactions on Power Delivery*, vol. 26, no. 4, pp. 2596-2604, Oct. 2011.

[75] O. G. Bellmunt, J. Liang, and N. Jenkins, "Voltage-current characteristics of multiterminal HVDC-VSC for offshore wind farms," *Elsevier Elec. Power Sys. Research* 81, vol. 81, no. 2, pp. 440-450, Feb. 2011.

[76] O. G. Bellmunt, J. Liang, and N. Jenkins, "Topologies of multiterminal HVDC-VSC transmission for large offshore wind farms," *Elsevier Elec. Power Sys. Research* 81, vol. 81, no. 2, pp. 271-281, Feb. 2011.

[77] J. Liang, O. G. Bellmunt, J. Ekanayake, N. Jenkins, and W. An, "A multiterminal HVDC transmission system for offshore wind farms with induction generators," *Elsevier Elec. Power Sys. Research*, vol. 43, no. 1, pp. 54-62, Dec. 2012.

[78] G. K. Carter, C. E. Grund, H. H. Happ and R. V. Pohl, "The dynamics of AC/DC systems with controlled multiterminal HVDC transmission," in *IEEE Transactions on Power Apparatus and Systems*, vol. 96, no. 2, pp. 402-413, Mar 1977.

[79] B. K. Johnson, R. H. Lasseter, F. L. Alvarado and R. Adapa, “Expandable multiterminal DC systems based on voltage droop,” in *IEEE Transactions on Power Delivery*, vol. 8, no. 4, pp. 1926-1932, Oct 1993.

[80] A. Bagheri-Vandaei and S. Filizadeh, "Generalised extended-frequency dynamic phasor model of LCC-HVDC systems for electromagnetic transient simulations," in *IET Generation, Transmission & Distribution*, vol. 12, no. 12, pp. 3061-3069, 10 7 2018.

[81] A. B. Vandaei, S. Filizadeh, K. Mudunkotuwa and E. Tara, "Real-time implementation of an enhanced dynamic phasor-based three-phase phase-locked loop for line-commutated converters," *2018 IEEE International Conference on Industrial Technology (ICIT)*, Lyon, 2018, pp. 812-817.